UNIVERSITÉ D'ORLÉANS

ÉCOLE DOCTORALE
Mathématiques, Informatique, Physique Théorique et Ingénierie des Systèmes (MIPTIS)

Laboratoire Pluridisciplinaire de Recherche en Ingénierie des Systèmes, Mécanique et Energétique (PRISME)

THÈSE présentée par :

Mustafa ELAHRES

Soutenue le : **16 décembre 2024**
Pour obtenir le grade de : **Docteur de l'Université d'Orléans**

Discipline/ Spécialité : Robotique

Motion planning based on the Artificial Potential Field for safe robotized echography: Application to multimodal medical imaging

Planification de mouvement basée sur le champ potentiel artificiel pour une échographie robotisée sûre : application à l'imagerie médicale multimodale

THÈSE dirigée par :

M. Gérard POISSON	Professeur des universités, Université d'Orléans

Co-Encadrant :

Mme Aïcha FONTE	Maître de conférences, Université d'Orléans

RAPPORTEURS :

M. Abderraouf BENALI	Professeur des universités, Université de Versailles Saint-Quentin
M. Med Amine LARIBI	Professeur des universités, Université de Poitiers

JURY :

Président :	**M. Pierre VIEYRES**	Professeur des universités, Université d'Orléans
Rapporteurs :		
	M. Abderraouf BENALI	Professeur des universités, Université de Versailles Saint-Quentin
	M. Med Amine LARIBI	Professeur des universités, Université de Poitiers
Membres :		
	Mme Aïcha FONTE	Maître de conférences, Université d'Orléans
	M. Gérard POISSON	Professeur des universités, Université d'Orléans
	M. Juan SANDOVAL	Maître de conférences, Ecole Centrale de Nantes
	M. Bertrand TAVITIAN	Professeur des universités, Université Paris Descartes

ORLEANS University

DOCTORAL SCOOL

Mathematics, Computer Science, Theoretical Physics, and Systems Engineering (MIPTIS)

Multidisciplinary Research Laboratory in Systems Engineering, Mechanics and Energy (PRISME)

THESIS presented by:

Mustafa ELAHRES

Defended on: December 16, 2024
To obtain the grade of: **Doctor of the University of Orléans**

Discipline/ Specialty: Robotics

Motion planning based on the Artificial Potential Field for safe robotized echography: Application to multimodal medical imaging

THESIS supervised by:

M. Gérard POISSON	Professor, University of Orléans

Co-Supervisor:

Ms. Aïcha FONTE	Associate Professor, University of Orléans

REVIEWERS:

M. Abderraouf BENALI	Professor, University of Versailles Saint-Quentin
M. Med Amine LARIBI	Professor, University of Poitiers

JURY:

M. Abderraouf BENALI	Professor, University of Versailles Saint-Quentin
Ms. Aïcha FONTE	Associate Professor, University of Orléans
M. Med Amine LARIBI	Professor, University of Poitiers
M. Gérard POISSON	Professor, University of Orléans
M. Juan SANDOVAL	Associate Professor, Ecole Centrale of Nantes
M. Bertrand TAVITIAN	Professor, University of Paris Descartes
M. Pierre VIEYRES	Professor, University of Orléans

TABLE OF CONTENTS

ABBREVIATIONS

DoF	Degrees-of-Freedom
CT	Computed Tomography
HU	Hounsfield Unit
FOV	Field of View
PET	Positron Emission Tomography
TOF	Time-of-Flight
MRI	Magnetic Resonance Imaging
US	Ultrasound Scan, Ultrasonography (also called echography)
RF	Radiofrequency
UUS, UUI, UFI	Ultrafast Ultrasound Scan or Imaging
SPECT	Single Photon Emission Computed Tomography
PETRUS	PET-Registered-Ultrasound
c-PETRUS	clinical Hybrid Positron Emission Tomography - Ultrafast Ultrasound
APF	Artificial Potential Field
KCD	KineoTM Collision Detector
SoT	Stack of Task
DLR	German Aerospace Center
UR5	Cobot from Universal Robots
SR	Super-Resolution
OTOROB	Orthopedic Robot
DH	Denavit-Hartenberg
IK	Inverse Kinematics
ROS	Robot Operating System
LORA	Level Of Robot Autonomy
HRI	Human-Robot Interaction
pHRI	physical Human-Robot Interaction
HRC	Human-Robot Collaboration

SYMBOLS

a_{i-1}	Distance between z_{i-1} et z_i along x_{i-1}
α_{i-1}	Angle between z_{i-1} et z_i about x_{i-1}
d_i	Distance between x_{i-1} et x_i along z_i
θ_i	Angle between x_{i-1} et x_i about z_i
α_i, a_i, θ_i, d_i	Denavit-Hartenberg Parameters of transformation
i	Robot link number
${}^{i-1}T_i$	Matrix homogeneous transformation
$c\theta_i$	$\cos(\theta_i)$
$s\theta_i$	$\sin(\theta_i)$
w_n^0	Angular velocity vector of the end effector frame R_n expressed in inertial frame R_0
v_n^0	Linear velocity vector of the end effector frame R_n expressed in inertial frame R_0
J_n^0	The Jacobian matrix between the robot base and end effector (n-th robot link)
$\dot{q}$	Joint angular velocity
$r_{P_j}^0$	Vector pointing to an arbitrary point P on the j-th robot link (j=1,2,…,n), expressed in the inertial frame R_0
$J_{P_j}^0$	The Jacobian matrix between the robot base and an arbitrary point P located on the j-th robot link
j	Robot link number
J_w, J_v	Upper and lower half of the Jacobian
F_{att}	Virtual attractive force
$k_{att,p}$	Proportional coefficient
P_f	Target position of the end effector
P_c	Current position of the end effector
M_{att}	Virtual attractive momentum
$k_{att,o}$	Proportional coefficient
e_O	Orientation error
Q_f	Quaternion target orientation of the robot end effector
η_f	Scalar parts of Q_f
ε_f	Vector parts of Q_f
Q_c	Quaternion current orientation
η_c	Scalar parts of Q_c
ε_c	Vector parts of Q_c

Se_O	Orientation error
$S(\varepsilon_f)$	Skew-symmetric matrix for the ε_f
T_{att}	Attractive torque affecting all the joints
$F_{rep,i}$	Virtual repulsive force affecting critical point i
k_{rep}	Proportional coefficient
$\|\Delta X\|$	Distance between critical point i and nearest point on the obstacle
$P_{ob,i}$	Nearest point on the obstacle to the critical point on the robot
$P_{cr,i}$	Critical point i on the robot
T_{rep}	Virtual repulsive torque generated from the obstacle and affecting
T	Total torque affecting the robot joints
$\alpha_{att}, \alpha_{rep}$	Weights to variate the priorities between target tracking and obstacle avoidance
$J_{cr,i}^{T}$	Jacobian matrix at that critical point
N	All effects on the joints
q	Increment in the robot state vector
C	A constant for torque to angle transformation
dq	Elementary of robot joint angles
$P_{cr,i}^{ob}$	Artificial potential field function
T_0^{ob}	Transformation between obstacle and base frame
R_{ob}	Spherical obstacle radius
$F_{rep,i}^{ob}$	Repulsive forces elements affecting critical points outside the gantry in two cases
U	Virtual fixture techniques
k	Proportional constant
r	Distance between the obstacle and the object
r_0	Distance precising a threshold
F_{max}	Fixed maximum value of the obstacle repulsive forces
F_{rep}	Repulsive force on the robot check point
dF(r)	Elementary repulsive force
dl	Elementary width on the obstacle effective edge
ds	Elementary surface on the obstacle effective surface
dv	Elementary volume in the obstacle
F	Repulsive force
R	Radius of the sphere
r	Distance between the obstacle centre and the robot check point
r1	Distances threshold to apply obstacle avoidance

ds_1	Elementary surface near a point $P_1(x_1, y_1, z_1)\big\vert_{O_1}$
ds_2	Elementary surface near a point $P_2(x_2, y_2, z_2)\big\vert_{O_2}$
dq_s	Joint displacement on slave side
α_F , β_F	Weighting parameter for repulsive forces
α_{APF}	Weight parameter for integrating the APF with teleoperation
d_{act}, $d_{tr,max}$	Actual and a threshold distance between the robot segments and obstacle
$dq_{s,teleop}$	Joint displacement on slave side produced by teleoperation
$dq_{s,obs}$	Joint displacement on slave side due to obstacle avoidance
$[X_{cr,i}^{ob} \quad Y_{cr,i}^{ob} \quad Z_{cr,i}^{ob}]$	Critical point coordinates in obstacle frame

LIST OF FIGURES

LIST OF TABLES

ACKNOWLEDGEMENTS

I want to sincerely thank everyone who has helped and encouraged me during my PhD journey.

Above all, I want to express my sincere gratitude to **Gérard** and **Aïcha**, my supervisors, for their constant support, tolerance, and direction. Their support went well beyond research guidance; they provided priceless help with administrative duties and, when required, individual encouragement.

I am incredibly appreciative of my wife **Nadin** and kids **Hicham, Salah, Leen, and Yusuf** for their patience and emotional support throughout the many long workdays. My motivation has come from your encouragement and understanding.

Sincere gratitude is extended to my friends **Anas**, **Mohammad**, and **Anwar**, whose early support enabled me to apply for this PhD program and whose financial and travel support enabled this journey.

Additionally, I would like to express my sincere thanks to the **PAUSE** program and the **Collège de France** for helping to arrange my travel and for providing the scholarship that enabled me to continue my research career in France.

My friend **Joseph**, who collaborated with me for the first two years of my PhD, deserves special recognition. My research benefited greatly from our stimulating conversations and his help to get started with the robot operating system ROS.

Lastly, I want to express my gratitude to **all the friends** and **coworkers** who have supported me along the way. Their contributions, no matter how minor, have had a significant influence on my PhD experience. I will always appreciate and remember your support.

Mustafa ELAHRES
December 2024, Orléans

Introduction

The integration of robotics with medical imaging technologies marks a significant milestone in advancing diagnostic and interventional procedures in healthcare. In recent years, the combination of multiple imaging modalities, such as CT-PET scans, with simultaneous ultrasound, has become a powerful approach for enhancing diagnosis reliability and guiding precise interventions. CT-PET imaging, which merges anatomical and metabolic data, is widely utilized in disease diagnosis, treatment planning, and monitoring. However, the real-time guidance necessary for many procedures remains a challenge. Ultrasound offers a solution with its dynamic imaging capabilities but integrating it into CT-PET workflows introduces technical complexities, particularly in confined environments like the CT scan, CT-PET or MRI, gantries.

This PhD thesis addresses these challenges by proposing the integration of a collaborative robotic system capable of performing tele-echography, within the CT-PET environment. This system not only enhances imaging quality but also tackles critical issues related to patient safety and equipment protection. The chosen collaborative robot, the *UR3e*, plays an important role in ensuring high precision while adhering to stringent medical safety standards. Through this work, we aim to advance the potential of image-guided interventions in clinical practice, offering new possibilities for improved patient outcomes.

Chapter 1 discusses the integration of ultrasound into CT-PET imaging workflows, focusing on the selection of the *UR3e* collaborative robot to perform tele-echography within the confined space of a CT-PET gantry. The chapter outlines the technical challenges of integrating these imaging modalities and addresses the requirements of safety, accuracy, and maintaining image quality. This chapter also sets the stage for understanding how robotics can enhance diagnosis reliability and safety in clinical settings.

The rapid development of robotics has transformed various sectors, including healthcare, with the emergence of collaborative robots (cobots) designed to work safely alongside humans. Collaborative robotics is reshaping how humans interact with machines, particularly in shared spaces where safety and precision are paramount. In this PhD thesis, we investigate the essential concepts of human-robot interaction (HRI), focusing on the physical interaction between humans and robots in medical settings. With the increasing adoption of teleoperated robotic systems, such as those used in echography, safe motion planning in dynamic, human-populated environments becomes a key concern. The International Standards Organization's ISO/TS 15066 guidelines for safe human-robot collaboration serve as a foundation for the safety protocols discussed in this manuscript.

Chapter 2 explores the foundational theories of physical human-robot interaction (pHRI), emphasizing the need for safe motion planning in shared environments, particularly in medical settings. It introduces key concepts such as levels of autonomy, safety measures, and hybrid approaches to motion planning. This chapter also reviews applications of collaborative robotics in medical procedures like robot-assisted echography, providing the theoretical framework for the more advanced methodologies explored in later chapters.

The ability to avoid collisions with obstacles in their environment is crucial for the safe operation of collaborative robots. This thesis explores artificial potential field (APF) algorithms as a method of obstacle avoidance in robotic systems. APF algorithms, with their intuitive design based on repulsive and attractive forces, are particularly effective for tasks requiring safety and adaptability, such as teleoperated medical procedures. However, APF methods face challenges, such as local minima, that must be overcome for effective motion planning. This research contributes to the field by developing a motion planning system based on the APF method adapted to medical applications, enabling robots to navigate in complex environments.

Chapter 3 focuses on the development and application of the Artificial Potential Field (APF) algorithm for collision avoidance during robotic teleoperation. It details the kinematic modelling of the *UR5* robot and the application of the APF method in guiding the robot through complex environments filled with spherical and cylindrical obstacles. This chapter presents simulations validating the algorithm, emphasizing its effectiveness for safe robot navigation in the described medical environment.

This thesis also expands upon APF's application in human-robot interaction, particularly in environments where robots must operate near human operators, such as in healthcare. Traditional motion planning methods typically address geometric obstacles like spheres and cylinders, but the complexities introduced by human anatomy require more detailed and more human-like modelling. This work extends the APF algorithm to account for human-like obstacles, offering a new framework for collision avoidance that improves the safety and efficiency of robotic systems in environments where human interaction is present.

Chapter 4 extends the APF algorithm to deal with human-like obstacles, modelling human anatomy with more complex shapes like elliptic cylinders. It explores the challenges of human variability and dynamic motion in human-robot collaboration, providing a conceptual framework for improving the safety of robotic navigation in environments shared with humans, such as the medical ones.

In addition, to developing safe motion planning algorithms, this PhD thesis integrates APF with teleoperation control systems to facilitate tele-ultrasound procedures during CT-PET scans by incorporating virtual haptic feedback and automatic collision avoidance into the teleoperation architecture. The use of haptic devices, such as the Phantom OMNI, improves the accuracy of robot-assisted ultrasound by providing tactile feedback to operators, allowing them to focus on the main task rather than focusing on the safety of the patient and the equipment.

Chapter 5 presents the integration of APF with teleoperation control for real-time ultrasound guidance in confined medical spaces, such as the CT-PET environment. It discusses the implementation of a haptic feedback system and shows how this framework enables safe and efficient tele-echography, reducing the cognitive load on medical staff while maintaining patient safety. Experimental results, from using the *UR3e* robot and Phantom OMNI haptic device, validate the system's effectiveness in providing collision-free teleoperation.

In summary, this PhD thesis work makes significant contributions to the fields of robotics, motion planning, and medical technology by integrating collaborative robots into clinical environments. The APF algorithm's application in teleoperated medical procedures, combined with its potential for human-robot interaction, presents a promising solution for enhancing safety, precision, and efficiency in healthcare. This work not only addresses immediate challenges in robotic motion planning but also lays the foundation for future advancements in tele-echography and other robotic-assisted medical procedures.

CHAPTER 1
Robot-assisted echography in CT-PET device

This chapter addresses integrating ultrasound guidance into CT-PET imaging through robotic assistance as a contribution to improving the efficacy and safety of diagnostic and interventional procedures in clinical settings.

Medical image fusion is an important component of modern healthcare, especially when it comes to multimodal medical imaging. It involves merging information from various imaging techniques, such as Magnetic Resonance Imaging (MRI), Computed Tomography (CT), Positron Emission Tomography (PET), and Single-Photon Emission Computerized Tomography (SPECT), to provide comprehensive diagnostic insights. This fusion process is pivotal in achieving high-resolution, high-quality images that aid in precise disease detection and treatment. The field of medical image fusion, especially the integration of CT, PET, and US imaging, has gained prominence due to its potential to significantly enhance clinical practice.

Context

Each medical imaging modality offers distinct advantages, but their combined use can provide a more comprehensive understanding of the patient's condition. For instance, CT offers detailed anatomical information, while PET reveals metabolic activity, and US can offer real-time, high-resolution imaging. Combining these modalities can improve the accuracy of lesion localization, enable precise treatment planning, and enhance disease detection. The current context of this research revolves around facilitating the fusion of CT, PET, and US images through developing a robotic system that guides the US probe inside the CT/PET device’s gantry.

Objectives

The primary objectives of our research are as follows:

Incorporate the ultrasound probe into CT-PET imaging device: develop a methodology for the navigation ultrasound guidance into CT-PET imaging to enhance medical interventions. This involves proposing a new imaging procedure where the robot manipulator holds the US probe while CT and PET images are acquired, followed by the US image.

Optimize Robotic Assistance: design and implement a robotic system that ensures safe motion for the ultrasound probe. The robot should operate through collaborative way, more precisely teleoperated, communicate effectively with medical staff, and prioritize patient safety throughout the procedure. It also should consider, and address challenges related to teleoperation, obstacle avoidance, and robotic motion. Implement safety measures to prevent patient and radiologist discomfort or injury.

This research aims to advance the field of medical image fusion by developing a systematic approach for integrating ultrasound into CT-PET imaging, with a strong focus on safety, accuracy, and improved patient outcomes. The design of the robotic system, as described below, is a critical component of the research.

Here are some key aspects to consider for this design:

- Robotic manipulator selection: choose or design a robotic manipulator that can precisely and safely hold and maneuver the ultrasound probe within the CT-PET imaging gantry. The manipulator should have the necessary *Degrees-of-Freedom (DoF)* to ensure required positioning.
- Integration with imaging device: ensure that the robotic system is seamlessly integrated with the CT-PET imaging device. This may involve adapting the robot's structure to fit within the imaging gantry without compromising patient comfort or safety.
- Ergonomics: consider the ergonomic aspects of the robotic system design to ensure that the ultrasound probe's movements are smooth and comfortable for the patient. This is necessary for minimizing patient discomfort during the interventional procedure.
- Control interfaces: develop user-friendly interfaces for medical staff to control and monitor the robotic system. This should include real-time visualization of the ultrasound images and the ability to adjust the robot's movements as needed.
- Safety features: implement safety mechanisms within the robotic system to prevent collisions with the patient or the imaging device. These safety features should include both hardware and software components to ensure patient well-being.
- Robotic control: the control of the robotic system is pivotal in ensuring the possibility and safety of ultrasound integration into CT-PET imaging.

Here are the control-related considerations:

- ➢ Motion control algorithms: develop appropriate motion control algorithms that enable the robot to manipulate the ultrasound probe with sufficient accuracy. These algorithms should take into account the specific requirements of the imaging procedure, including patient positioning and imaging protocols.
- ➢ Real-time feedback: implement real-time feedback systems that allow the robot to adjust its movements based on the position of the ultrasound probe and the imaging device. This feedback loop is essential to ensure the safety and success of the medical procedure.
- ➢ Teleoperation: because the procedure involves remote control of the robotic system, a teleoperation system that enables medical staff to manipulate the robot effectively need to be developed. Potential time delays in communication need to be addressed.

- Obstacle avoidance: obstacle avoidance algorithms are integrated to ensure that the robot can navigate within the imaging gantry without collisions. This is particularly important when the environment is partially visible or when the robot operates in close proximity to the patient.
- Safety overrides: safety overrides are implemented to allow immediate stopping of robotic movement in the event of unexpected circumstances or emergencies.

This research should aim to strike a balance between precision, safety, and patient comfort when designing and controlling the robotic system for ultrasound integration in CT-PET imaging. The successful execution of these aspects will contribute significantly to the overall success of the whole work and its potential impact on clinical practice.

In order to understand the technical requirements and aspects of the research, we need to introduce the different medical imaging modalities, CT, PET, and US, mentioned in this thesis and explain their principles.

1.1 Computed tomography (CT) scan

After its clinical introduction in 1971, computed tomography (CT) developed from an X ray modality that was limited to axial imaging of the brain in neuroradiology into a versatile 3-D whole body imaging modality for a wide range of applications, including oncology, vascular radiology, cardiology, traumatology and interventional radiology (Dance, D. R., Christofides, S., Maidment, A. D.A., McLean, I. D., & Ng, K. H., 2014).

CT has revolutionized the diagnosis and treatment of a wide range of medical conditions.

1.1.1 Principles of CT

CT scans use X-rays to create detailed images of internal body structures, which are then reconstructed into cross-sectional images using computer algorithms.

The process of CT image acquisition involves the measurement of X ray transmission profiles through a patient for a large number of views. A profile from each view is achieved primarily by using a detector arc generally consisting of 800–900 detector elements (dels), referred to as a detector row. By rotation of the X ray tube and detector row around the patient, this large number of views can be obtained. The use of tens or even hundreds of detector rows aligned along the axis of rotation allows even more rapid acquisition (Fig 1.1). The acquired transmission profiles are used to reconstruct the CT image, composed of a matrix of picture elements (pixels).

The values that are assigned to the pixels in a CT image are associated with the attenuation of the corresponding tissue or more specifically, to their linear attenuation coefficient. This linear attenuation coefficient depends on the composition of the material, the density of the material and the photon energy. Since a CT image is composed of a matrix of pixels, the scanned patient can also be regarded as being made up of a matrix of different linear attenuation coefficient volume elements (voxels). From the above, it can be seen that the basic data needed for CT are the intensities of the attenuated and unattenuated X ray beams, respectively, and that these can be measured. Image reconstruction techniques can then be applied to derive the matrix of linear attenuation coefficients (in Hounsfield units), which is the basis of the CT image (Dance, D. R. et al., 2014).

CT images are typically displayed in eight-bit grayscale, with each pixel's Hounsfield Unit (HU) value mapped to one of 256 gray levels. Windowing, involving adjustments to window width and level, is used to enhance visualization. Choosing the right window settings depends on the clinical purpose, such as viewing soft tissue, lung, or bone. Inaccuracies in HU values can result from factors like reconstruction filters, field of view (FoV) size, and artifacts. Longitudinal studies should account for potential HU value variations over time.

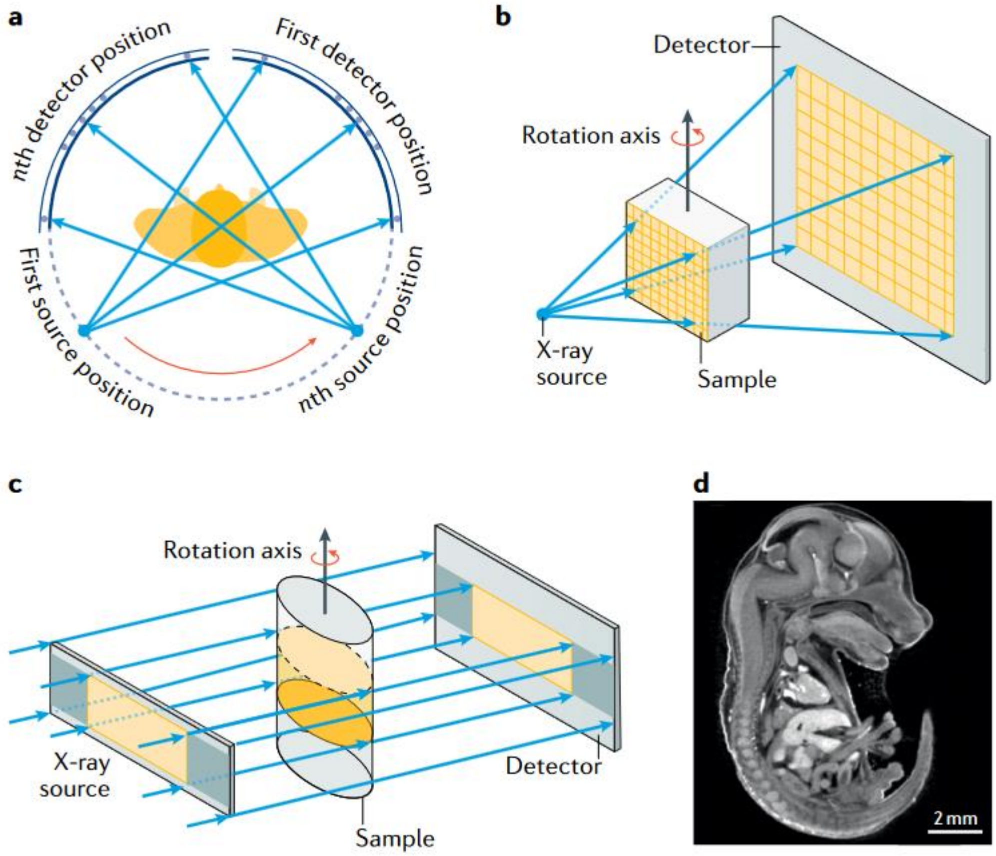

Figure 1.1: Common X-ray computed tomography configurations
a-Gantry system where the source and the detector rotate in tandem around the patient, animal or specimen. b-Cone beam system typical of laboratory systems. c-Parallel beam system geometry typical of synchrotron X-ray systems. d-Virtual slice through an attenuation contrast tomogram of an iodine-stained mouse embryo (Withers et al., 2021)

1.1.2 The CT imaging system description

The CT imaging system consists of a gantry and a table. The CT scanner gantry contains essential components for capturing patient transmission profiles from various angles, including the X-ray tube, collimator, beam shaping filters, detector arc, and data acquisition system. These components must withstand centrifugal forces during fast gantry rotation. Slip ring contacts provide power to the rotating gantry, and wireless technology transmits projection profiles to a computer. The patient table must support varying positions and heavy weights without bending. The X-ray tube uses a tungsten anode and a cooling system to manage the high X-ray flux. Collimation creates a fan beam, while beam shaping filters ensure uniform exposure and image quality, particularly in the axial plane. CT scanner engineering is critical for accurate data acquisition in medical imaging.

Solid state detectors, currently used, are generally scintillators, which means the X rays interacting with the detector generate light. This light is converted to an electrical signal, by photodiodes that are attached to the back of the scintillator, which should have good transparency to ensure optimal detection. Typically, an antiscatter grid is mounted at the front of the detector, which consists of small strips of highly attenuating material (e.g. tungsten) aligned along the longitudinal (z) axis of the CT scanner, forming a 1-D antiscatter grid.

1.1.3 Artefacts and their undesirable effects

Achieving proper image quality in computed tomography (CT) scans requires regular calibrations. These calibrations ensure accurate detector responses, essential for precise image projections. Common artifacts in CT scans are categorized as acquisition-related (e.g., ring artifacts), reconstruction-related, and patient-related. Patient-related artifacts can be minimized by instructing patients to minimize movement and maintain breath-holding during scans. Beam hardening artifacts are a significant concern in computed tomography (CT) imaging. These artifacts arise due to the preferential attenuation of lower-energy X-rays as they pass through an object, causing a beam hardening effect. This effect can distort CT images, particularly when dealing with materials like compact bone, calcifications, or metal objects. It leads to streaks and inaccuracies in the reconstructed images, and therefore in diagnostic reliability.

1.1.4 Advancements in CT technology

With the advancement of CT technology, patient safety has improved dramatically. Newer CT scanners require less radiation exposure than earlier models, which helps reduce the risk of radiation-related health problems. In addition, CT technology allows doctors to detect health problems earlier, which can lead to more effective treatments.

CT technology is used for a wide range of medical applications, including cancer detection, heart disease diagnosis, and neurological disorders. CT scans are also used in emergency medicine to quickly diagnose internal injuries and other life-threatening conditions.

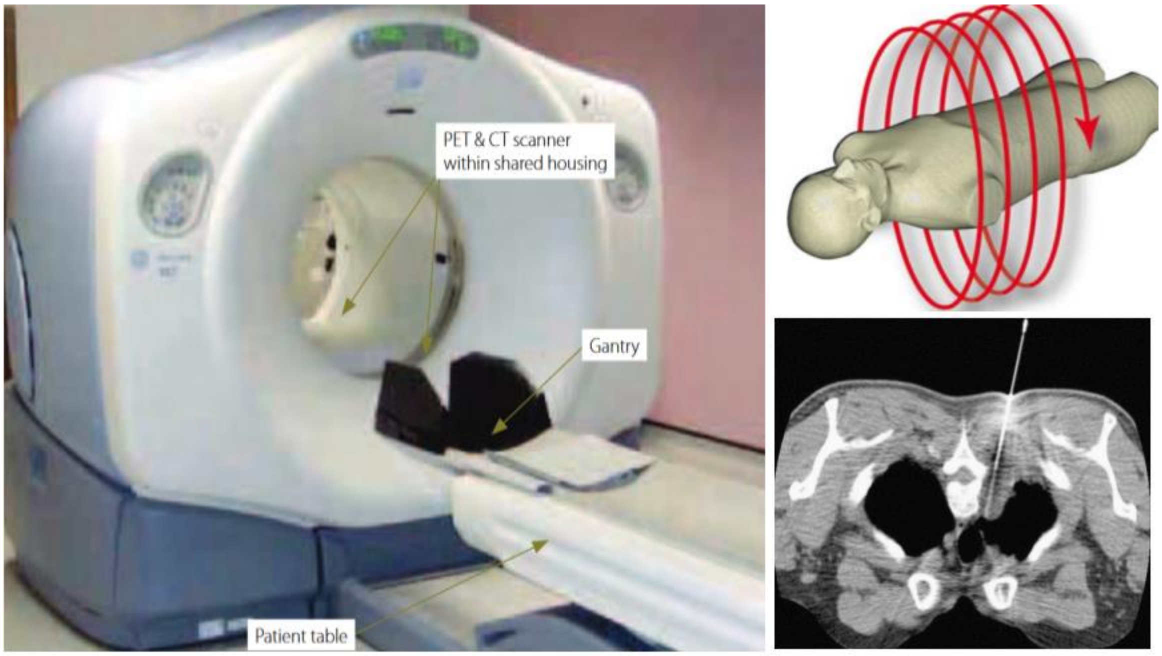

Figure 1.2: A typical PET-CT scanner (left). Geometry of a helical CT (top right). A plan scan for CT fluoroscopy guided puncture showing the needle (bottom right) (Dance, D. R. et al., 2014)

1.2 Positron emission tomography (PET) scan

Positron emission tomography (PET) is the imaging of radiopharmaceuticals labelled with positron-emitting radionuclides. Positrons are the positively charged antimatter version of the electron and are ejected during the radioactive decay of a proton-rich nucleus; during this decay process, a proton in the nucleus is converted into a neutron. The positron is released from the nucleus with a significant amount of kinetic energy and travels a short distance before interacting with the nearby atoms several times. During every interaction, the positron loses some of its kinetic energy and travels in a random direction through the surrounding material. The positron annihilates a nearby electron when it is at rest. The energy associated with their combined mass is transformed into two annihilation photons with a proper amount of energy due to the conservation of energy. Conservation of momentum dictates that the two photons are emitted from the point of annihilation travelling in opposite directions (Fig 1.3). These properties, the instantaneous production of two photons of equal energy travelling 180° to each other, are the basis of the PET imaging technique used to localize where the original annihilation event occurs within the patient. A PET scanner consists of multiple rings of crystal scintillation detectors. Each detector is a few mm in size, and a group of them are formed into a block that is typically connected to a group of four photomultiplier tubes. The scintillator detectors convert incoming photons into light before amplifying the signal using the photomultiplier tubes. The two photons traveling at the speed of light will be detected almost instantly when there is a positron emission within the ring of detectors. Coincidence events are photons that arrive at various detectors during this coincidence timing window.

The "line of response" is the path between the two detectors that picked up each coincidence event. Typically, data are collected over several minutes and all detected coincidence events are grouped into parallel lines of response to form projections through the patient that are used for image reconstruction, typically using iterative reconstruction techniques. The great advantage of this type of localization is that, unlike a gamma camera, it does not require collimators to provide positional information and therefore offers much higher sensitivity than single-photon emission computed tomography (SPECT). The detectors form a special camera that benefits from the radioactive tracer to produce images of the body's metabolic and biochemical processes (Fig 1.3. right bottom). The figure shows how the ring detects photons (red arrows) which result from the annihilation of an electron with a positron emitted by the radiotracer (FDG).

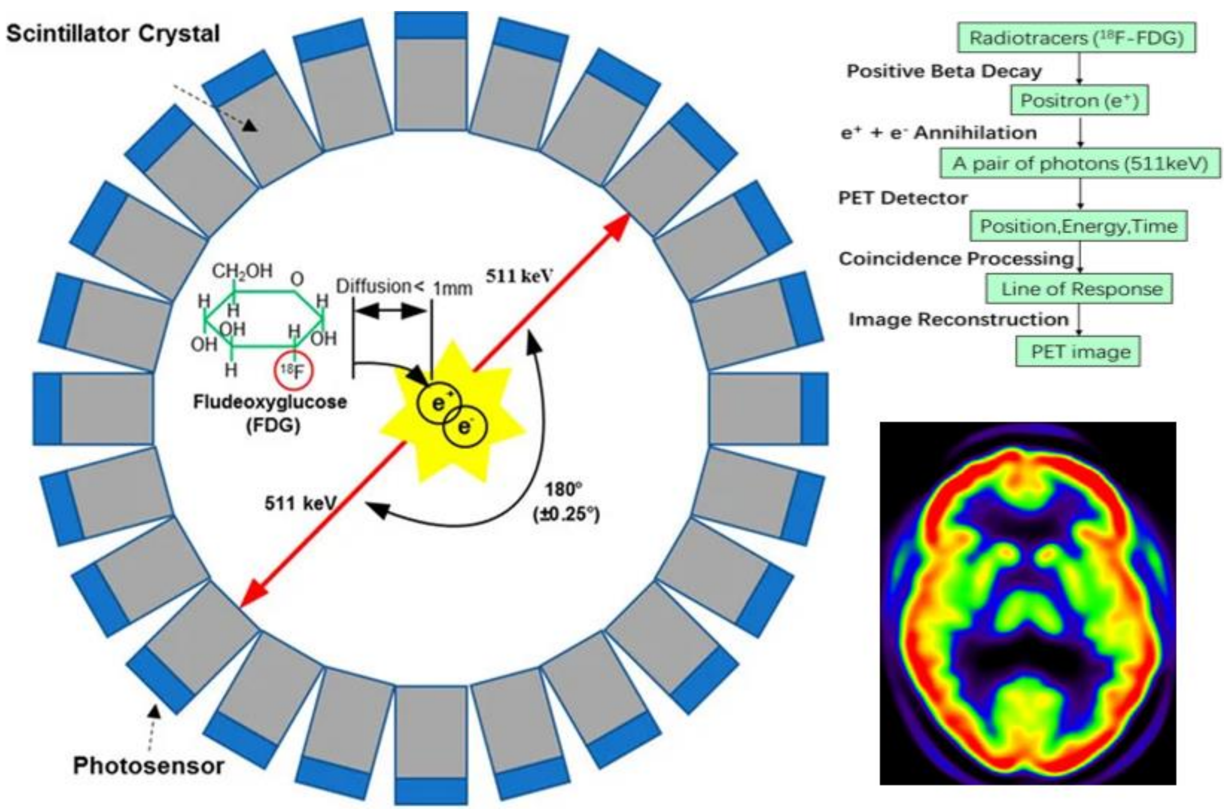

Figure 1.3: The basic principle of a PET system: the PET detector ring (left). Detection flow of the PET system (right up) (Jiang, Chalich, & Deen, 2019). PET images of a normal brain (right bottom) (Lameka, Farwell, & Ichise, 2016)

Various types of technologies are used in PET scan. High-Resolution PET Scanners have high resolution. Thus, they can produce more detailed and accurate images. Time-of-Flight (TOF) PET Scanners can measure the time it takes for a photon to travel from the tracer to the detector, providing more accurate information about the location of the tracer. There are also Hybrid PET-MRI and PET-CT scanners which combine PET imaging with magnetic resonance imaging (MRI) or computed tomography (CT) as we will see later, respectively, providing more comprehensive and detailed images.

These advancements in PET scan technology are leading to more accurate diagnoses and more personalized treatment plans for patients with a wide range of medical conditions. They are mainly used to diagnose and monitor cancer, neurological disorders, and cardiovascular disease. Because PET can detect picomolar concentrations of molecular probes with a resolution typically in the millimetre range, it is considered the gold standard for molecular imaging. Due to PET's remarkable ability to non-invasively show local biochemistry, numerous PET tracers have been developed, and more and more of them have received clinical approval for use in diagnostics (Provost et al., 2018).

1.3 Ultrasound (US) scan principle

Long after underwater sonar imaging was developed, conventional ultrasonography for medical purposes began to be used in the 1970s. This led to a link between the idea of echolocation in underwater acoustics and how we create images in medical ultrasound. Initially, backscattered echoes at depths along a focused beam line were recorded using ultrasound devices equipped with single focused elements (a-mode). Then, for a brief time in the 1970s, ultrasonic images were obtained by mechanically moving the focused transducer.

Consequently, the development of electronic focusing and multiple element arrays has made line-per-line acquisition the fundamental technology utilized in all ultrasound scanners (Tanter & Fink, 2014). The term "ultrasonic" refers exclusively to sound waves with frequencies higher than the nominal 20 kHz maximum frequency at which humans can hear sound. Ultrasound with a frequency range of 2–15 MHz is typically used for diagnostic imaging. Since higher frequency waves can be focused more tightly but are attenuated by tissue more quickly, the choice of frequency is determined by a trade-off between penetration depth and spatial resolution. The physical processes that underlie the propagation, reflection, and attenuation of ultrasound waves in tissue have an impact on the information contained in an ultrasonic image (Dance, D. R. et al., 2014).

Short acoustic pulses are sent through the human body's region-of-interest during a traditional US scanning procedure. After that, the raw channel data, also known as the backscattered echo signals, are processed to produce radiofrequency (RF) beamformed lines. Acoustic waves with frequencies between 20 kHz and 1 GHz make up ultrasound signals. By electrically stimulating a piezoelectric transducer, which is able to produce and detect ultrasonic energy, these waves are created. The ultrasound waves in the medium are transmitted and received using the same transducer. The fundamental concept of ultrasound imaging is shown in Fig 1.4 (Szasz, 2016). Fig 1.5 illustrates the entire scanning process.

Additional information and details on sound propagation laws, transducer properties and design, and how to visualize the signals reflected from the medium can be found in (Szasz, 2016) in order to gain a better understanding of the principle of interaction between the sound and the particles in the propagating medium.

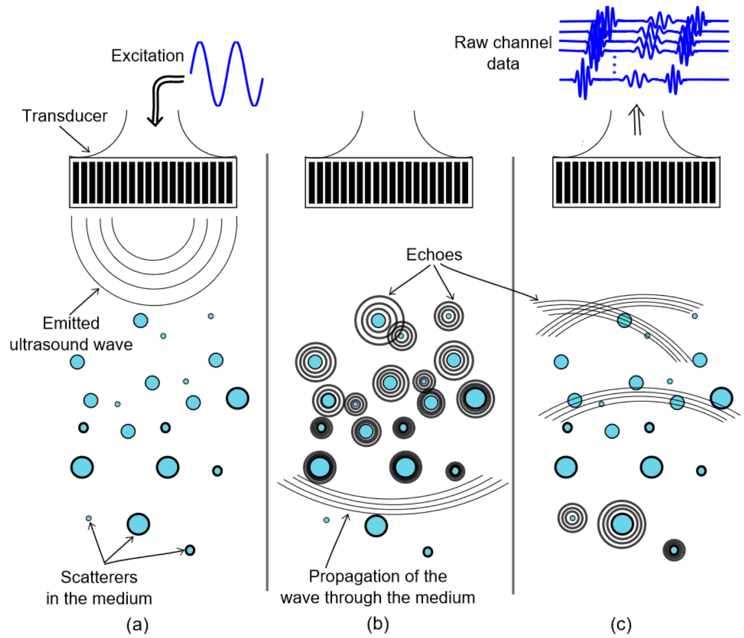

Figure 1.4: The principle of ultrasound imaging
(a) an electrical pulse is transmitted to the transducer to form the ultrasound wave (b) the wave propagates and interacts with the medium (c) the waves are received and transformed to electrical signals (raw channel data) (Szasz, 2016)

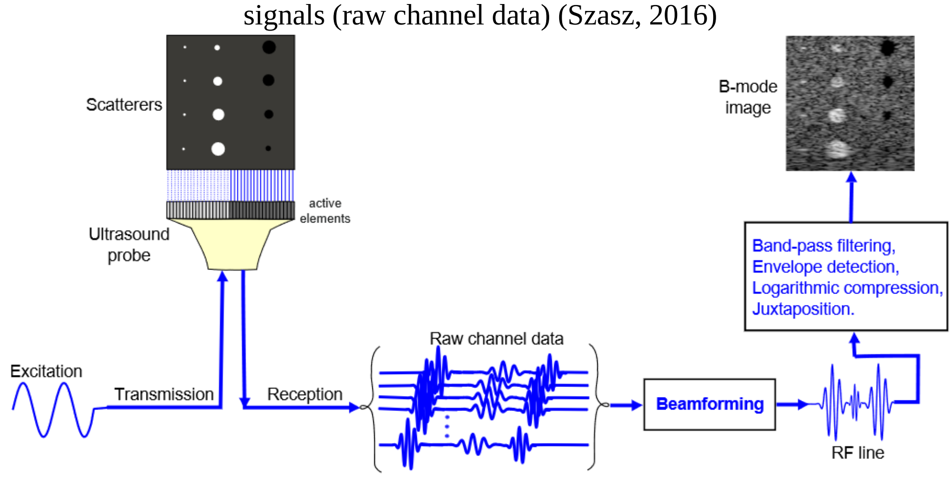

Figure 1.5: General ultrasound scanning process (Szasz, 2016)

1.3.1 Ultrafast Ultrasound imaging (UUI)

Ultrafast ultrasound echography is a more recent method of medical ultrasound imaging that takes inspiration from optical holography and ultrasonic time reversal. This method uses a wide field-of-view plane wave for insonification, capturing the backscattered echoes, in contrast to conventional sonar-based techniques. Ultrafast ultrasonography uses time-reversed echoes to create images, much like optical holography, which uses interference to record light fields on a holographic plate and then reconstructs them. During backpropagation, time-reversal ultrasound efficiently creates a wavefield that optimally refocuses on the original object, producing an image that is spatially accurate in the end. This technology, which allows for the computational reconstruction of high-quality images from a single transmission and is based on the concepts of digital parallel receive beamforming, has the potential to produce ground-breaking improvements in ultrasound (Tanter & Fink, 2014).

Because UUI can capture images in a wide field of view in less than a millisecond, it is an ideal tool for studying fast-moving phenomena and gathering a lot of data to attain high sensitivity. UUI benefits from an active research community where new imaging modes are constantly being developed. Applications include brain activation imaging, tissue stiffness measurement for cancer or fibrosis staging, cardiac activation, and non-invasive in vivo angiography of small vessels. In recent times, UUI has been expanded to three dimensions, enabling the acquisition of thousands of volumes per second (Provost et al., 2018).

1.4 Medical image fusion

Many multimodal medical imaging techniques, such as MRI, CT, PET, and single photon emission computed tomography (SPECT), are used for medical diagnostics. Every modality has a specific purpose and is used in a given application. While the MRI, CT, and ultrasound provide information about the anatomical structures of the organs, the SPECT and PET show the functional and metabolic activity.

Medical image fusion is the ideal solution for additional useful images with higher corresponding data and higher image details. Thus, it may be considered as a merging tool for relevant knowledge from a series of medical images into one comprehensive image. There are so many applications of image fusion that require high spatial and spectral resolutions within a single image besides achieving higher image quality.

Many good features distinguish the fusion process in the medical field such as (Faragallah et al., 2021):

1) Accurately provides the image location of lesions and significantly reduce the surgical risk.
2) Extraction all the advantageous info from source images into a specific image.
3) Fusion of images can improve reliability and capability by complementary information.
4) It is convenient for the detection and classification of numerous diseases.
5) Fusion process reduces the data storage required and time for transmission.

6) It can provide accurate information for a precise localization and size estimation for tumors.

Consequently, the field of medical image fusion multimodalities has recently emerged as a challenging area for research.

In the next parts, we will discuss the fusion of CT, PET, and US as this is the medical application context to be delt with during this work.

1.4.1 PET-CT fusion

Although CT is an excellent tool for evaluation of structural abnormalities of the brain, the addition of PET as a hybrid PET-CT offers the benefit of functional imaging (Fig 1.6). For example, while CT provides anatomic information, it does not usually distinguish between malignant and benign tissue. This is significant when measuring response of tumor to treatment. Anatomic imaging has limits in the delineation of tumor extension when tumor-bearing structures have unchanged anatomy or when tumor and normal tissues have similar density, or similar contrast enhancement. Other value of hybrid PET and CT is that these scans are obtained in the same gantry in a single imaging session with the patient in the same position, allowing for the use of the CT scan component for attenuation correction of the PET scan. Patient motion between CT and PET scanning may cause an inaccuracy in the CT image and misregistration of the two image datasets. However, image misregistration is usually corrected using special software programs (Lameka et al., 2016).

Fig 1.6 presents a typical PET-CT imaging system combining a PET scanner, for molecular imaging, with a multiple-detector-row CT scanner, for anatomic imaging. Each of the software and hardware is designed to measure proper information from a patient bed moving in the two scanners.

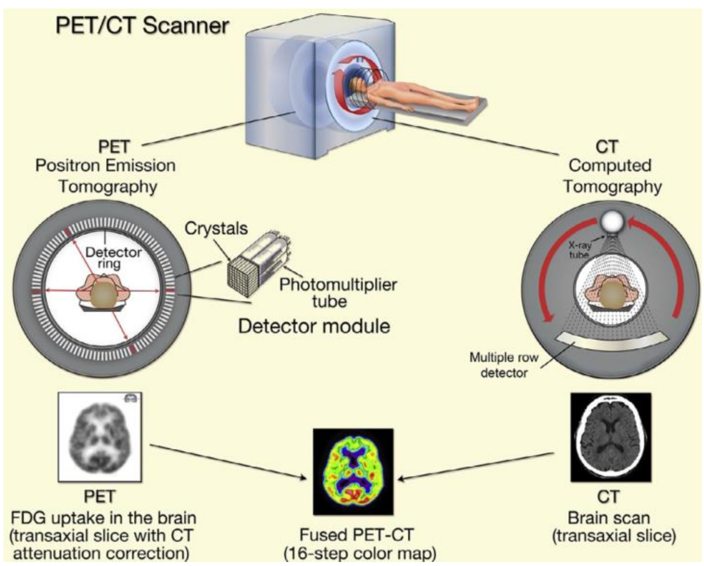

Figure 1.6: Typical PET-CT imaging system (Lameka et al., 2016)

For the CT component of the scan, lasting seconds, the table moves uninterrupted while a continuous volume is acquired in spiral scan mode. For PET images, the bed moves in incremental steps based on the PET detectors' field-of-view (typically 16.2 cm) with each acquisition typically taking 3–6 minutes. The PET detector ring is shown with a multicrystal scintillation detector and photomultiplier tubes (Lameka et al., 2016).

The fusion of CT and PET images has advanced in recent years, thanks to improvements in hardware and software. The main developments include precise image registration techniques for accurate alignment, advanced reconstruction algorithms for better image quality, and the development of new PET tracers targeting specific molecular markers. These advancements have augmented the clinical usage of CT and PET scan fusion, enabling more accurate diagnosis, and treatment planning for various diseases, including cancer, neurological disorders, and cardiovascular conditions. PET-CT is the standard clinical imaging method for staging cancer extension, combining molecular and anatomical imaging modalities (Provost et al., 2018).

1.4.2 PET-CT-US fusion

PET images are currently obtained and co-registered with a computed tomography (CT) scan (PET-CT), which is utilized for anatomic localization and attenuation correction. Even though PET has a high negative predictive value, false-positive results can still happen. which could require a biopsy in order to confirm or rule out cancer. Nonetheless, certain lesions that are positive for PET could show minimal or no correlation in their ultrasound (US) and/or CT results (i.e., low conspicuity on morphological imaging). Due to inherent technical constraints, a biopsy cannot be performed solely with PET guidance; instead, PET data needs to be incorporated into a CT- or US-guided biopsy procedure (multimodal US-PET-CT fusion imaging) (Paparo et al., 2014).

The anatomical localization of actively uptaking lesions can be improved by real-time fusion of US and PET modalities, as shown in (Di Mauro et al., 2013). This is particularly significant when lesions are poorly or not visible in the US alone. A greater degree of confidence was guaranteed during the follow-up phase by this fusion. It made treatments possible that would not have been possible technically if they had only relied on PET-CT and had no real-time capabilities.

A team of researchers (Provost et al., 2018) in INSERM proposed a triple-imaging modality (PET-CT-UUI) that combines the three imaging modalities into a single device for fully co-registered imaging in real time, allowing image fusion without motion artifacts or longer acquisition times. Through integration, the physiological correlates defined by hemodynamic, biomechanical, electrophysiological, and quantitative structural parameters will be linked to metabolic activity. The lightweight, portable UUI instrumentation for which specific, customized sequences were developed was used to assemble the hybrid imaging PET-CT-UUI instrument from already-available, commercially available devices.

The team demonstrated how a 6-DoF motorized micro-positioner was used to precisely control the ultrasound probe in order to achieve full, markerless, rigid-body three-dimensional (3D) registration, and how the ultrasound probe's presence had no effect on the PET volumes' quality. Remarkably, PET-CT-UUI can generate multi-parametric data that is not currently possible with any other non-invasive imaging technique. In this study, they illustrate how this imaging modality can produce hitherto unseen information from fused, concurrently acquired volumes of PET-CT-UUI images in pre-clinical oncology and cardiology applications. Fig 1.7 shows the whole system setup with the fusion process and Fig 1.8 shows the preclinical device for the experiments.

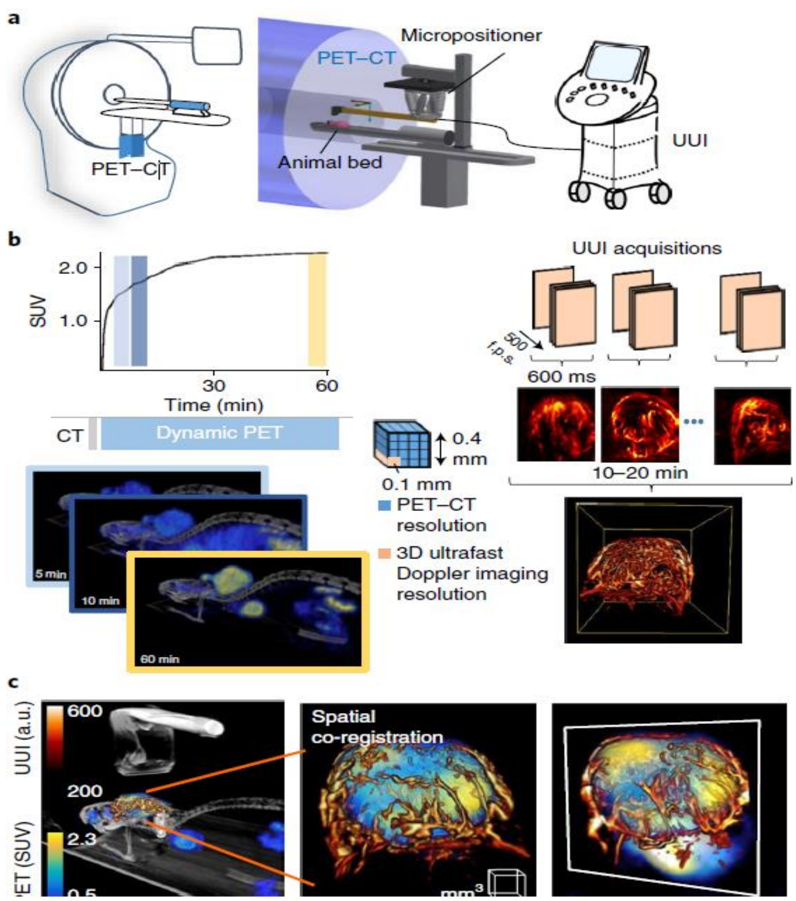

Figure 1.7: PET-CT-UUI set-up and acquisitions

a, The combination of an ultrafast ultrasound scanner and a PET-CT device. b, Left: SUV for FDG PET scans (top, black line). dynamic PET-CT 3D reconstructions of a mouse (bottom). Right: UUI in ultrafast Doppler imaging mode in a mouse tumor. c, PET-CT-UUI images of a mouse tumor xenograft. Left: the ultrasound probe located above the targeted tumor in the CT and the fused PET-UUI volume. Middle: maximal intensity projection view of the spatially co-registered tumor. Right: view of image plane inside the volume (Provost et al., 2018)

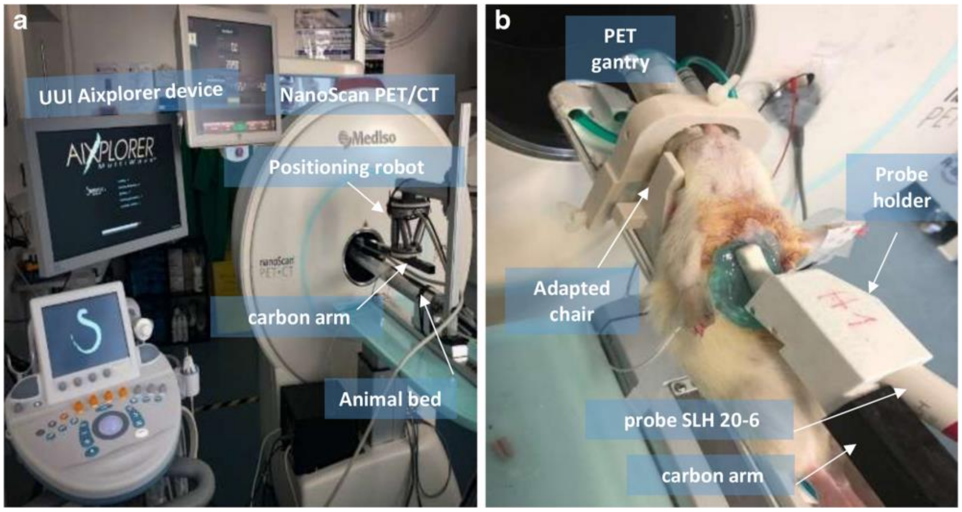

Figure 1.8: PETRUS setup for cardiac exploration in rodents
a) elements of the PETRUS system. b) animal location for PETRUS cardiac studies in rats (Perez-Liva et al., 2020)

1.5 The c-PETRUS project

In the last years, the INSERM team, mentioned earlier, has built a preclinical imaging instrument PETRUS (PET-Registered-Ultrasound) that simultaneously acquires positron emission tomography (PET) and ultrafast ultrasound images (UUI), with which the INSERM team obtained co-registered images of two main cancer biomarkers: glucose metabolism with PET and neo-angiogenesis with high-sensitivity UUI Doppler. The INSERM team proposes the extension of this preclinical prototype (Fig 1.8) to a clinical device (c-PETRUS) in collaboration with our laboratory (PRISME). The project will focus on the technological level for the conception of the clinical device and its optimal exploitation. Based on the development of in vivo, simultaneous, 3D, non-invasive, and non-contact methods of UUI and PET, the goal is to develop a hybrid image system, Clinical Hybrid Positron Emission Tomography - Ultrafast Ultrasound: c-PETRUS, using state-of-the-art collaborative robots (cobots). A device that enables spatial and temporal correlations of parameters characterizing the evolution of a tumour and its response to treatment. The successful implementation of this will contribute to the field by enhancing the accuracy and reliability of image-guided interventions through multimodal imaging fusion. And improving the whole procedure by providing clinicians with comprehensive real-time information.

The general objectives of the c-PETRUS projects are:

1) Implementation of the PETRUS prototype into a clinical PET scanner.
2) Using a proper robot system to manipulate the US probe within the gantry of the PET-CT imaging device with the development of a proper navigation system.

3) Development of a real-time and high-resolution reconstruction and an optimized multimodal image co-registration algorithm to link these tissue properties in space and time.
4) Development of a statistical framework for advanced multiparametric analysis to facilitate the best interpretation of tumorigenesis and therapeutic targeting.

This project is based on some hypotheses like:

1) Acoustic imaging is an unparalleled tool to be combined with metabolic PET imaging for its portability, real-time, high temporal and spatial resolution, and acoustic waves' interaction with tissues gives access to a wide range of tissue parameters.
2) The real-time acquisition with ultrasonic probes doesn't alter the quality of the PET images acquired simultaneously and doesn't affect the imaging process (Perez-Liva et al. 2018).

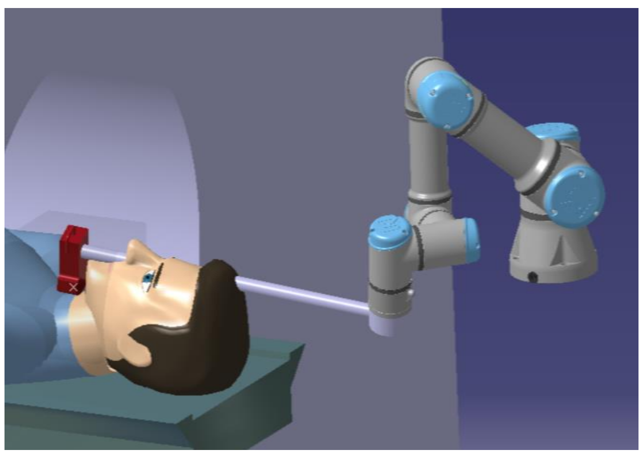

Figure 1.9: Image of echography inside CT-PET device

In PRISME laboratory, we will involve in the fulfilling the objective (2) of this project. Development of a navigation system based on a CT image and optimization of volumes acquisition by adding and evaluating the feasibility of using a 6 (or 7) DoF poly-articulated cobot to manipulate a US probe within the confines of a PET-CT imaging device.

We will select an industrial prototype cobot that meets clinical specifications in terms of reachable workspace, dexterity, speed and accuracy, safety. Using the technical characteristic of this cobot, we will define the optimal location of the cobot in the PET-CT environment. In this complex environment, the robotic control needs to be well designed in order to guarantee intelligent behaviour for greater accurate and safe motions. Finally, we will develop different robotic procedures corresponding to the different experimental tests required by c-PERTUS and we will validate the cobotic approach and define its limits.

1.5.1 Imaging procedures

It is important to describe the proposed medical procedure in order to be able to precise the robot motion's requirements.

I. Basic CT-PET imaging procedure

This involves acquiring CT and PET images of the patient separately, with the patient lying on the imaging table. The images are then registered using software to fuse them into a single image.

II. Proposed CT-PET-US imaging procedure

In this procedure, the robot manipulator would hold the US probe while the patient is lying on the imaging table. The CT and PET images would be acquired first, followed by the US image. The images would then be registered using software to fuse them into a single image.

III. Robot motion

The proposed methodology for CT-PET-US fusion using a robot manipulator can be divided into three main stages:

1. **Comanipulation**: involves the robot manipulator and the surgeon working together to control the US probe and position it accurately.
2. **Teleoperation**: involves the radiologist remotely controlling the robot manipulator using a computer interface.
3. **Robot Homing**: involves the robot manipulator returning to a pre-defined position after completing a task.

Desired accuracy and stability should be achieved through the use of precise robotic control algorithms and sensors. The robot should be designed to move smoothly and ergonomically, taking into consideration the patient's skin shape. Multi-risk zones velocity should be considered to ensure patient safety.

IV. Safety considerations

The robot manipulator should:

- Be designed to apply maximum force to the patient, as specified by medical references,
- Be programmed to avoid contact with the patient except for the US probe in the examination region,
- Move smoothly and ergonomically to avoid discomfort or injury to the patient,
- Be designed to communicate effectively with the patient and staff using multiple modalities, such as visual and auditory feedback.

V. Failure considerations

In case of failure, the robot manipulator should have limits on accelerations and velocities to prevent injury to the patient. The robot should also be designed to avoid self-collision and avoid the gantry.

In conclusion, the proposed methodology for CT-PET-US fusion using a robot manipulator involves careful consideration of imaging procedures, robot motion, and safety considerations. The robot manipulator should be designed to move smoothly and accurately, communicate effectively with the patient and staff, and ensure patient safety at all times.

1.5.2 The proposed methodology for CT-PET-US fusion

In this context and given the experience of our PRISME laboratory in robot-assisted tele-ultrasound (Bassit, Poisson, & Vieyres, 2003; Gourdon, Poignet, Poisson, Parmantier, & Marche, 1999), we will provide a solution to these limitations by combining ultrasound images with PET-CT images using a poly-articulated collaborative robot to manipulate the US probe within the gantry of the PET-CT imaging device with the development of a proper navigation system.

In PRISME laboratory, as a partner with INSERM in this project, we will present a new robotic solution that allows the insertion of an ultrasound probe inside the gantry of a PET-CT imaging device, offering clinicians a new approach to Tele-echography under PET-CT test. This solution, developed in the frame of c-PETRUS project (Clinical Hybrid Positron Emission Tomography - Ultrafast Ultrasound) promises to facilitate the clinical procedure of diagnostic imaging, to ensure patient comfort and safety, ensure equipment safety, and optimize workflow efficiency.

In such applications, a robot is utilized to guide an ultrasound probe hold by a specific tool within hollow cylinders (gantries) where a patient is located. The robot manipulates the probe to perform echography, under expert control. Sometimes the echography needs to be performed through teleoperation or comanipulation (separated or combined). Additionally, once the task is completed, the robot must navigate and exit the confined environment.

Throughout these sub-tasks, the complex poly-articulated robot mechanism must avoid collisions with the boundaries of the environment and of course with the present humans (patient and medical team).

Due to the physical principles governing medical devices (e.g., CT scans, PET scans) in which the robots operate, teleoperation is generally employed for these manipulations. However, there are several challenges associated with this approach:

1- The environment may not be entirely visible or only partially visible to the operator.
2- While teleoperating the robot, the operator can ensure obstacle avoidance by employing telemanipulation. However, success always guaranteed. Errors can occur during telemanipulation, especially because the operator may not have a complete view of the articulated mechanism while controlling the robot's terminal organ. Furthermore, delays or failures in transmitting information between the master and slave devices can result in obstacles not being avoided in time.

3- Focusing on obstacle avoidance during the telemanipulation can distract the operator from the main task. Thus, it is more effective to assign the obstacle avoidance sub-task to an automatic and safe controller.

In conventional teleoperation scenarios, the human operator handles the obstacle avoidance task by visually observing the environment and using a haptic device to avoid obstacles as they appear. However, in our case, this approach presents two main issues:

a- A complete and clear view of the work environment is not always available, making manual obstacle avoidance challenging.

b- Adding obstacle avoidance to the operator's responsibilities increases the cognitive load, particularly in tasks that demand complete concentration, such as medical diagnosis, where the operator must analyse the environment, operate the robot, and interpret medical images for diagnosis.

Assigning obstacle avoidance to the human operator may compromise the performance of the primary task, and they may struggle to succeed in either task. Hence, a more effective approach is to implement an automatic algorithm directly on the slave robot, which can independently handle the obstacle avoidance task while the main teleoperation task remains the focus.

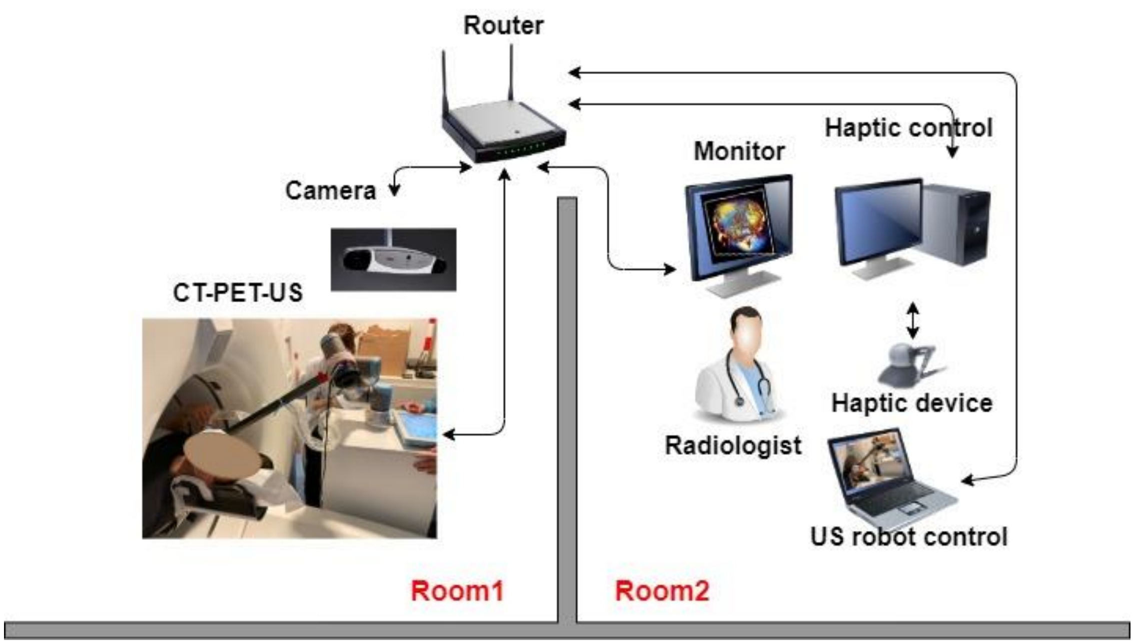

Figure 1.10: The CT-PET-US diagnostic system

1.5.3 The research objectives

This thesis aims to address the following objectives:

1. Integration of ultrasound into CT-PET imaging: Develop a methodology for incorporating ultrasound guidance into CT-PET imaging procedures to enhance intraoperative guidance and interventions.
2. Optimization of robotic assistance: Design and implement a robotic system capable of safely manoeuvring an ultrasound probe within the CT-PET gantry. This involves addressing challenges such as teleoperation, obstacle avoidance, and ensuring patient and operator safety.

Robotic system selection for tele-echography in CT-PET gantry

The integration of robotics in medical diagnostics, particularly in remote and precision-based procedures, has expanded the range of potential applications. But this integration requires some considerations to take to ensure successful tasks with no undesired effects. In this part, we highlight the process of selecting an appropriate robotic system to conduct tele-echography within the gantry of a CT-PET device. Our choice is dependent upon fulfilling some requirements and restrictions while maintaining enough level of accuracy, safety, and practicality.

Robot capability requirements: the robotic system must fulfil the following requirements to ensure the task execution:

Tele-echography: a robotic ultrasound arm system must reproduce the gross and fine motor control of a human upper extremity. The system must have a range of motion (ROM) that would at minimum allow examination of all four quadrants of the abdomen. Force and torque must be sufficient to provide an image of diagnostic quality without injuring the patient. The system must rotate the ultrasound probe in excess of 90° to allow longitudinal and transverse imaging (roll). It must also angle the transducer to optimize the image (pitch and yaw) and perform linear translations (x, y, z) with roughly 1 mm of tolerance. These fine adjustments are routinely made during handheld sonography. The arm should hold still without drift. Ideally, the system would allow probe changes without human intervention (Swerdlow, Cleary, Wilson, Azizi-Koutenaei, & Monfaredi, 2017). To perform the key component of our goal, which is to telemanipulate an ultrasonic probe, the robot needs to have enough dexterity. For our application, a versatile robotic arm that has 6 DoF (3 positions + 3 rotations) is an appropriate option because it offers the manoeuvrability needed for probe manipulation.

Co-manipulation with a human: in the complex landscape of medical procedures, human expertise is irreplaceable. In this application, the ultrasound probe needs to be inserted into the gantry at the beginning of the clinical procedure and before starting the tele-echography. Due to the patient's bodies various topologies and sizes, this insertion can’t be repeatable. So, the human will manually insert the ultrasound probe into the gantry through robot hand-guiding to prepare it for the tele-echography process. Therefore, our robotic system must allow for co-manipulation, where a human operator can hand-guide the robot. Collaborative robots, known for their safety features and human-robot interaction capabilities, seamlessly facilitate this essential collaboration. We can't do it through teleoperation because it requires relatively big displacements which might be insecure through teleoperation, and it needs to change the scaling factor to be able to perform big displacement for the insertion and small displacements for the tele-echography. So, it would be more efficient to consider hand-guiding to globally navigate the robot around the patient and teleoperation to locally navigate the ultrasound probe at the region of diagnostic.

Special requirements and constraints: to perform the main goal while ensuring patient safety and the task feasibility, the robotic system has to fulfil some other requirements:

Patient safety, working beside a patient: safety and patient well-being should be given priority. Thus, the robotic system must be designed/chosen to operate safely near patients. Collaborative robots, engineered to work in harmony alongside humans, provide the required assurance of patient safety in the medical context.

Equipment safety, collision avoidance: navigating the gantry of a CT-PET device presents a unique challenge. inserting the ultrasound probe and performing the manipulations without collisions with the gantry borders and with some patient's parts. This requirement necessitates a robot with six degrees of freedom (6-DoF) at least to provide full operational space, allowing for precise movements and obstacle avoidance.

Preserve the CT image quality: computed tomography (CT) is a commonly used imaging method in disease diagnosis and treatment planning. In particular, dose distributions in radiation therapy are calculated as the solution of a forward problem; CT images determine the electron density of the irradiated tissues and patient-specific anatomy (Pimkin et al., 2020)**.** High-density objects like metal that exists in the area of interest, strongly affect the attenuation of X-Rays that may lead to distortion of the final image reconstructed from an inconsistent sinogram (Boas & Fleischmann, 2012). These image artifacts could have a significant impact on the dose calculation accuracy and reduce the visibility of organs and structures close to the metal objects. We need to prevent the insertion of metal pieces inside the gantry in order to protect the validity of CT scan images as a requirement to avoid extra image processing to reduce the distortion that may occur due to the existence of metal inside the CT gantry. This restriction leads us to make the ultrasound probe holder out of a non-metal material, ensuring that it has no impact on the CT images.

Robot selection synthesis: starting from the requirements above, we make the analysis of robot choice as follows:

Kinematic choice: the selection of the robot kinematics is essential in our quest for the robotic system choice. Although parallel platforms provide stability, efficient use of space in the crowded gantry environment is our main concern. As a result, we decide to use a collaborative robotic serial arm that balances end-effector stability with space utilization.

Precision requirement: in tele-echography, the human hand has a precision of about 1 mm. This precision will be reduced (e.g., 10 mm with a gain of 10) at the slave side because of the teleoperation gain that magnifies the master robot displacements in this application. Therefore, the typical precision of robotic manipulators, approximately 1 mm at the end effector (typically they are better than this), aligns seamlessly with the precision demanded by human teleoperation. Excessive precision would be redundant and costly.

Robot workspace and redundancy considerations: robotic systems with redundancy can perform secondary tasks like obstacle avoidance while also carrying out the primary task of tele-echography, which improves capabilities. However, it is not important for our particular application. A 6-DoF manipulator is a practical choice because there aren't any long-distance manipulations that call for switching between workspace regions which change the robot's pose.

Tool design and control strategies: we are aware that the elongated, potentially elastic tool for the ultrasound probe holder may present difficulties, like magnifying the error and vibrations at the ultrasound probe, but we also understand that the solution to these problems lies not only in the robot accuracy choice, but also in the careful tool design and proficient robot control strategies. These components will be important in reducing this type of errors, vibrations, and disturbances throughout the procedure.

As a result, the choice of a robotic system for tele-echography in the CT-PET gantry is a multidimensional that is influenced by a wide range of factors and limitations. By choosing a collaborative robotic arm with six degrees of freedom (UR3e from Universal Robot), we can customize our choice to the special needs of the medical application, ensuring safety, accuracy, and usability in the quest for better patient care and diagnostics. This decision establishes the framework for the completion of our research project in this difficult but exciting field.

This chapter addresses integrating ultrasound guidance into CT-PET imaging through robotic assistance aiming to improving the efficacy and safety of diagnostic and interventional procedures in clinical settings. It also provides a clear overview of the research goals, objectives, and the significance of addressing the integration of ultrasound with CT-PET imaging using robotic systems. In the second chapter we well present some theoretical and state-of-the-art background regarding the various modalities of this research.

CHAPTER 2
Theory and state-of-the-art
of safe motion planning and collaborative robotics

This chapter provides an overview of the theoretical basis and the current state of research relevant to collaborative robotics, and robot-assisted echography. The first section contains the key theories for human-robot interaction and its main aspects like collaboration. Then, we will present motion planning with obstacle avoidance for robot manipulators in order to set the stage for the detailed methodological approaches discussed in the next chapters. The second section will elaborate on robot-assisted echography.

2.1 Human-robot interaction (HRI) and Collaborative Robotics

Robotic technologies have rapidly evolved since the first industrial robot, Unimate 001, introduced in the mid-twentieth century (Pie, 2021). In 1942 Isaac Asimov published the science fiction novel "I, Robot", where the three laws of robotics were introduced. First rule stated that "A robot may not injure a human being". Until now, industrial robots have been efficient devices dedicated for specific tasks. However, they work behind cages with protective equipment to secure humans to respect Isaac's rule. Collaborative robots, designed to work with humans, helped in omitting these cages. They are built with various safety features to either prevent collisions, or reverse the mechanism direction through compliance to avoid causing injury to the human (Mihelj et al., 2019).

2.1.1 Physical Human-robot interaction (pHRI)

The design and evaluation of robotic systems to be used by or with humans has led to the emerge of *Human-Robot Interaction (HRI)* field of study witch addresses problems related to the ways of interacting with robots. Those interactions can be physical or social ones. In this thesis we are more interested in applications that contain physical human-robot interaction (pHRI). Based on these ways of interaction, a classification for the levels of interaction has been introduced in literature. In (Trafton et al., 2005), authors have introduced a scale of HRI as a continuum from teleoperation, where the human directly controls the robot's motions, to dynamic autonomy, where the robot can exercise its own initiative and set its own goals while collaborating with the human. Fig 2.1 shows the human interaction scale with the robot.

Although this classification considers some of the more popular ways of interaction at the time, the emerging advancements in this kind of robots led to more comprehensive classifications in literature as we will see later in this chapter.

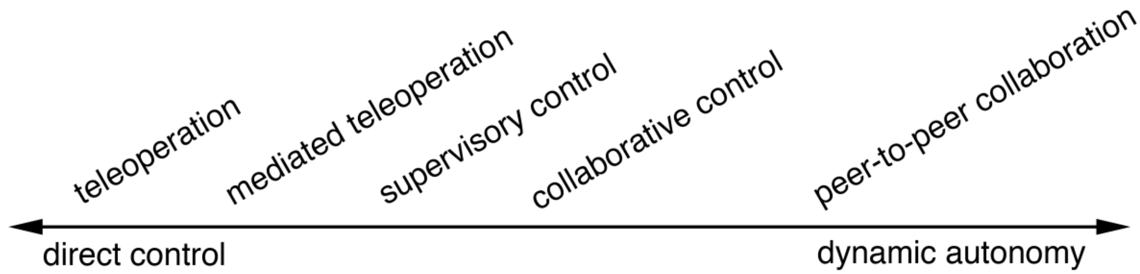

Figure 2.1 : Levels of human interaction with autonomous system (Trafton et al., 2005)

As it can be seen in the figure above, *Human-Robot Collaboration (HRC)* is a form of interaction between humans and robots and can be considered as a sub-field of HRI. Its objective is to perform a task by combining both human's and robot's skills in what is called *collaborative robotics*. Humans have natural flexibility, intelligence, and problem-solving abilities, while robots provide precision, power, and repeatability. Collaborative robots are particular robots designed specifically to work safely alongside people or to assist them during certain tasks (Gervasi, Mastrogiacomo, & Franceschini, 2020).

Although the terms *Cooperation* and *Collaboration* sometimes are used as synonyms in the literature, they can have different meanings. *Cooperation* can be defined as "working together to accomplish shared goals", while *Collaboration* is "working in a group of two or more to achieve a common goal, while respecting each individual's contribution to the whole". *A cooperative work* is defined as a task that is accomplished by dividing it among participants, where "each person is responsible for a portion of the problem", and C*ollaborative work* as "the mutual engagement of participants in a coordinated effort to solve the problem together". It can be noticed from these definitions that cooperation is more focused on working together to create a final product and can be achieved even if all participants do their assigned parts separately. However, collaboration also requires sharing knowledge, implying direct interaction among participants. Thus, compared to cooperation, collaboration is a more complex form of interaction and requires the fulfilment of additional conditions in order to be achieved(Gervasi et al., 2020).

2.1.2 Collaborative robots

Collaborative robots are particular robots designed to work in the same space or on the same tasks with people. They allow a safe co-existence and a natural interaction with humans and have some form of autonomy.

The concept of *collaborative robot* was introduced for the first time in 1996 by Colgate et al. A collaborative robot, *cobot*, was introduced as a robotic device which manipulates objects in collaboration with a human (Colgate, Wannasuphoprasit, & Peshkin, 1996). The collaboration was seen as a form of assistance in which, the robot enables guiding and constraining some of the human's movements. According to ISO/TS 15066 standard, a collaborative robot is "a robot intended to physically interact with humans in a shared workspace". Cobots have some differences from industrial robots (as presented in Table 2.1) (Matúšová, Bučányová, & Hrušková, 2019).

Table 2.1: Comparison of industrial and collaborative robots (Matúšová et al., 2019)

Collaborative robots		Conventional industry robots
Simply programming		Programming is time- consuming
Lower weigh of robot < 29kg		High weigh of robot > 50kg
Embedded security features		Missing of safety sensors
Operation in the limited space		Large operation space
Lower weigh of machined workpiece		Greater load capacity
Mobile		Immobile
External force sensors		Sensors of external forces are missing
Faster and simpler setting		High operation speed in operation
Flexibility of deployment		Universal usage in the limited space

A collaborative robot aims to support and relieve humans through collaborative work, where a purposely designed robot system and a human operator work in direct cooperation within a defined workspace. The term robot defines robot arm and robot control and does not include the robot end-effector or part. While the term robot system we describe robot, end-effector, and workpiece (Mihelj et al., 2019).

Collaborative workspace

Different workspaces can be defined for the collaborative robot system, as shown in Fig 2.2. **Maximum workspace**: all the area that can be reached by the moving segments of the robot, the end-effector, and the workpiece**. Restricted workspace**: part of the maximum workspace restricted by surrounding objects that impose limits are not exceeded. **Operating workspace**: part of the restricted workspace that is used while performing all motions commanded by the task planner. **Collaborative workspace**: part of the operating workspace where the robot system and a human can perform tasks concurrently during task execution.

Some aspects need to be considered when designing the collaborative workspace to enable the human to perform his task safely. In the collaborative workspace strict limitations about the speed, space limits, and torque sensing are applied to guarantee operator safety.

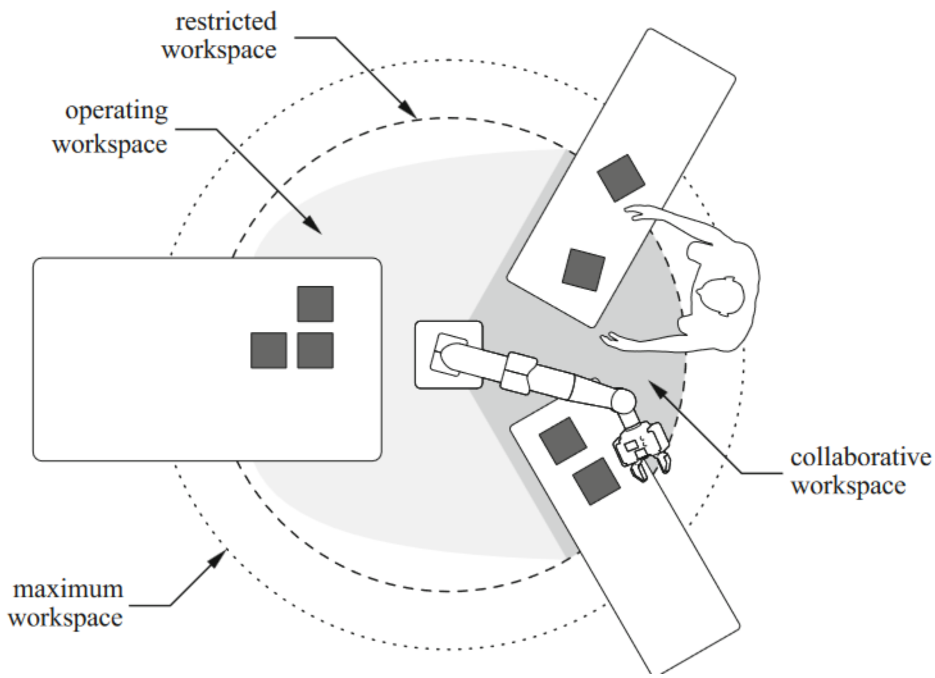

Figure 2.2: Maximum, restricted, operating, and collaborative (dark grey area) workspaces (Mihelj et al., 2019)

Depending on the use of the robot, task, the robot system role, and the environment, collaborative operation can be classified into four main techniques (Mihelj et al., 2019) as presented in Table 2.2. These techniques are: 1-safety-rated monitored stop; 2-hand guiding; 3-speed and separation monitoring; 4-power and force limiting.

Applications of Collaborative Robotic System

The ISO 10218-2:2011 standard explains some collaborative application modes which are:

1-Hand-over window application (Fig 2.3a). The robot is located behind guards where the task is performed in automatic mode without limitations. Human-robot interaction is done through a window. The robot reduces its speed when approaching the window (Mihelj et al., 2019).

2-The interface window (Fig 2.3b) acts as a barrier for the robot system. On the robot side the robot can perform autonomous automatic operations. The robot system is also guarded by fixed or sensitive guards around the workspace. The robot stops at the interface window and can be then manually moved outside the interface. For guided movement the robot must be equipped with hand guiding device.

3-Applications including simple assembling and handling can take advantages of the collaborative workspace (Fig 2.3c). Inside the common workspace the robot can perform automatic operations. When the operator enters the collaborative workspace, the robot reduces speed and/or stops. In this type of application, additional person detection systems using one or more sensors are needed.

4- Applications including inspection and parameters tuning (e.g., welding application) (Fig 2.3d) require guarded workspace and person-detection systems. When the operator enters the shared workspace, the robot continues operation with reduced speed. The application needs to have additional measures to prevent misuse.

5- Hand-guided robots (Fig 2.3e) are used for hand-guided applications (e.g., assembling or painting). The robot is equipped with hand-guiding device. The operator guides the robot by hand along a path in a task-specific workspace with reduced speed. The area of collaborative workspace is mainly dependent on the hazards of the required application.

Table 2.2: Types of collaborative operations (Mihelj et al., 2019)

	Speed	**Torques**	**Operator controls**	**Technique**
Safety-rated monitored stop	Zero while operator is in collaborative workspace	Gravity and load compensation only	None while operator is in collaborative workspace	No motion in the presence of the operator
Hand guiding	Safety-rated monitored speed	As by direct operator input	Emergency stop, enabling device, motion input	Motion only by direct operator input
Speed and separation monitoring	Safety-rated monitored speed	As required to maintain min. separation distance and to execute the application	None while operator is in collaborative workspace	Prevented contact between the robot system and the operator
Power and force limiting	Max. determined speed to limit impact forces	Max. determined torque to limit static forces	As required by application	Robot cannot impart excessive force (by design or control)

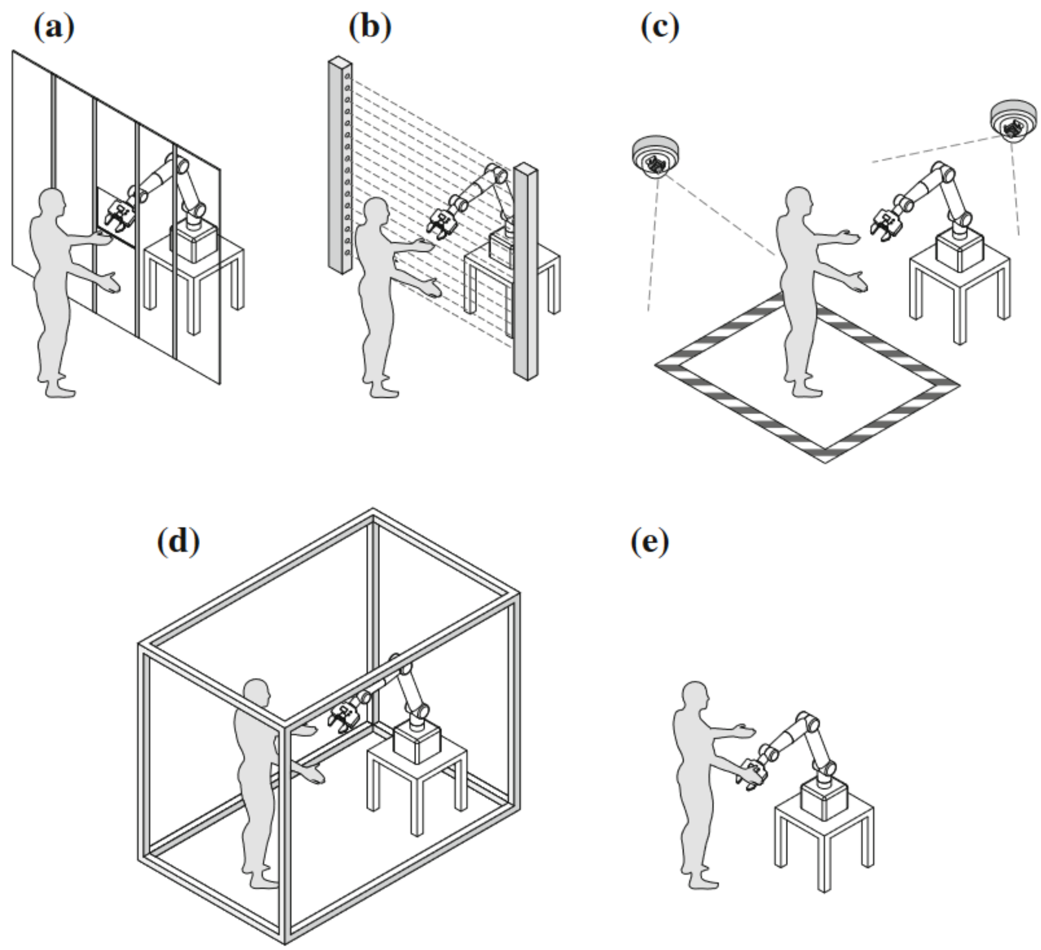

Figure 2.3: Conceptual applications of collaborative robots
a) hand-over window, b) interface window, c) collaborative workspace, d) inspection, and e) hand-guided robot (based on ISO 10218-2:2011) (Mihelj et al., 2019)

Although ISO 10218-2:2011 presented these applications from industrial point of view, some of them can be used to describe some applications in other domains. In our case the hand-guided applications can describe robot-assisted echography when it is performed through Comanipulation (hand-guiding).

2.1.3 Safety in pHRI systems

ISO 10218-1:2011 and ISO 102182:2011 (ANSI/RIA R15.06:2012) provided some requirements and guidance for industrial robots. However, The technical specification ISO/TS 15066:2016 (Chemweno, Pintelon, & Decre, 2020) supplements those requirements and guidance on collaborative industrial robot operation. It specifies safety requirements for collaborative industrial robot systems and the work environment and provides comprehensive guidance for risk assessment in their applications.

Safety assurance strategies for collaborative robot systems can be classified into 6 different ones based on (Chemweno et al., 2020):

1. Passive safeguards (embedded on the robotic system): includes laser scanners, lightweight robotic structure, foam padding, fluid-based actuators with force and torque limiting functions, torque and force compliant mechanical actuators.
2. Active safeguards (control-related): includes intelligent assist devices, impedance control for collision avoidance, agile control-oriented strategies with human cognition, active force controllers, force/torque sensing.
3. Task-oriented design safeguards: learning-from-demonstration task design approach, cognitive automation strategies, task-based constraints for motion planning.
4. Biomechanical models and metrics for quantifying collision risks: probability and collision impact metrics, force and torque limiting thresholds.
5. Design of interactive virtual environments: laser zoning approaches for interactive collaboration, human supervisory control strategies, kinetostatic danger field.
6. Risk-oriented approaches: proactive risk profiling, dependability risk assessment models.

2.1.4 Teleoperation

The rise of robotics began with the need to manipulate highly radioactive objects without exposing the human operator. In the late 1940s, Raymond Goertz built master–slave remote handling devices to grasp and move objects in 6 D*egrees-of-Freedom*. Mechanical tapes were used first to ensure the coupling between the human operator's master and the slave, but later this coupling employed electromechanical servos with force feedback. Since then, there has been much progress in telerobots in variety of domains. In medicine, surgical telerobots, such as the DaVinci system, first approved in 2000, are now permitting better precision by scaling down and dejittering of the surgeon's hand motions for minimally invasive surgery. This is not restricted to surgeries, but also physically handicapped persons are now experiencing improved arm manipulation and walking prostheses and orthoses (Sheridan, 2016).

2.1.5 Robot in medical applications

Medical robotics has the potential to change medical care in the same way that robots have transformed industrial tasks. Unlike the repetitive nature of industrial tasks, medical procedures are complex and non-repetitive or minimally repetitive requiring an interactive approach. In this context, collaboration or any other form of interaction between robots and healthcare professionals is essential. One example of medical robots are the surgical ones, whose goal is not to replace the surgeon with a robot, but to provide him with an additional set of very adaptable tools that increase the surgeon's capacity to treat patients (Taylor, 2006). However, this goal is extended to all medical robot types using a collaborative approach that aims to make the most of both human and robot strengths. Therefore, these systems are frequently referred to as medical assistants that collaborate with specialists. Robots are superior at fine motor control and geometric accuracy, whereas people are better at adapting to new situations and making important decisions. According to (Taylor, 2006), the core functions of medical robots are to supplement physician talents, improve process safety, and enable thorough procedure data capture.

The literature contains a wealth of works documenting the evolution, challenges, and prospects of medical robotics, with a significant focus on robotic-assisted surgery. One of the most detailed sources is (Hoeckelmann, Rudas, Fiorini, Kirchner, & Haidegger, 2015) and (Taylor, 2006) which contribute to our understanding of the role that medical robotics plays in shaping the healthcare.

There has been a successful introduction of robotics in medical domains like neurosurgery, skull and ENT surgeries, and orthopedics surgery thanks to the rigid nature of bones which makes preplanning robot trajectories possible. However, this is not the case in some other domains like minimally invasive interventions involving soft tissue manipulation for several reasons, including the difficulty of tracking deformable anatomy and a lack of force feedback, 3D vision, and surgical dexterity. In order to deal with these limitations, the next generation of surgical robots are based on synergic collaboration or teleoperation between the robot and the surgeon (Troccaz, Dagnino, & Yang, 2019).

The evolution of surgical robots encompasses not only size and architecture but also cooperative interaction with the surgical team and safety measures. The implementation of a suitable human–robot interface and specific control strategies is paramount for the safety and optimal outcome of the surgery. Initially, medical robots were used as passive tool holders and eventually, they became able to adapt in real time preprogrammed plans to the intraoperative position of a target. Future surgical robotic systems are aimed to be better able to cooperate with surgeons, providing them not only with superhuman dexterity but also with integrated real-time intraoperative image guidance, sensing, and decision making. Sight and sense information will allow the surgeon to close the control loop of the system and synergistically operate with the robot. As a result, the standard master/slave configuration (wherein the slave manipulator inside the patient replicates the movements of the surgeon's hands as the master) could be further improved through the use of real-time imaging and sensing in the control architecture. This implementation of the perception–decision–action loop architecture along with surgical robotic assistance will guarantee the best possible treatment in terms of surgical success and safety. Physicians will cooperate with robotic systems such that they will complement each other, with a minimal footprint in the operating or radiology room and maximum integration with the clinical workflow (Troccaz et al., 2019).

In (Troccaz, Berkelman, Cinquin, & Vilchis-Gonzales, 2002) is presented a classical taxonomy in medical robotics that distinguishes three categories of guiding systems for computer-aided surgery: active, passive and semi-active systems (see Table 2.3). Passive systems can inform the surgeon about the position of the surgical tool and the surgeon is totally responsible for the execution of the surgical task. Active systems realize a part of the intervention autonomously. A robot may perform without interaction with a human operator who generally supervises the action. A semi-active system involves a combined action with the human operator in a way that allows an ergonomic, direct and accurate intervention.

There are also two other types of systems that have been introduced more recently: Synergistic and Tete-robotic systems. Synergistic, also called Comanipulated or Cooperated, systems, are intended for direct physical guidance of a surgical tool that is also held and controlled directly by a surgeon. Such systems are general-purpose mechanical devices held by the surgeon's hand which allow him to feel the virtual world of patient data (including safety regions around anatomical obstacles to be avoided) and of surgical strategies, while moving in the real world. This is a generalization of semi-active systems which allows to make various mechanical constraints. In Tete-robotic systems the surgeon remotely controls a surgical tool held by a robot. Robotic systems which enable tight cooperation between man and machine belong basically to semi-active, synergistic (comanipulated), and tele-operated robots which are called *Interactive Robots* (Troccaz et al., 2002).

Six levels of autonomy for medical robotics were more recently proposed by (Yang et al., 2017) as shown in Table 2.3:

1- No autonomy: Like tele-operated robots, prosthetic devices that respond to and follow the user's command, and surgical robot with motion scaling.
2- Robot assistance: The robot provides some mechanical guidance or assistance during a task while the human has continuous control of the system. Like surgical robots with virtual fixtures (or active constraints).
3- Task autonomy: The robot is autonomous for specific tasks initiated by a human. The operator has discrete, rather than continuous, control of the system. Like in surgical suturing where the robot performs the suturing autonomously after the surgeon indicates the place. The surgeon monitors and intervenes only when needed.
4- Conditional autonomy: A system generates task strategies, but the human selects which one or approves a strategy selected by the system. *E.g.* an active lower-limb prosthetic device detects the user's will to move and adjusts without direct attention from him.
5- High autonomy: The robot makes medical decisions with the supervision of a doctor.
6- Full autonomy: A "*robotic surgeon*" that can perform an entire surgery.

Full autonomy requires technology that replicates the sensorimotor skills of an expert surgeon. With decreasing human oversight and increasing robotic perception, decision-making, and action.

Table 2.3: Different levels of human–robot interaction and autonomy mapped to medical robots (adapted from (Troccaz et al., 2002, 2019; Yang et al., 2017))

Decision (autonomy) levels / **HRI levels**	**No autonomy**	**Robot assistance**	**Task autonomy**	**Conditional autonomy**	**High autonomy**	**Full autonomy**
	Operator performs all tasks. This level includes passive and teleoperated systems	Operator maintains continuous control of the system. The robot provides some guidance. Examples include robots with virtual fixtures. This level includes semi-active and comanipulated systems	Operator maintains discrete control, and the robot performs certain tasks autonomously but initiated by a human	Operator selects and approves the surgical plan, and the robot performs the procedure autonomously with human oversight	Robot is able to make medical decisions, under human supervision	The robot can perform the entire surgery with no human in the loop. Currently science fiction
Passive	Neuronavigator					
Teleoperated	Da Vinci					
Semi-active		Renaissance			**Not yet Existing**	
Comanipulated		Mako				
Active			ROBODOC	CyberKnife		

Teleoperation had an important influence on the medical field. One notable step was the "*Spartacus*" project initiated by INRIA in 1975 (Kwee et al., 1983). In this project, a telemanipulator “*telethesis*” for high level tetraplegic and similarly disabled persons has been developed. The system had a modular control structure assuring the ergonomic link with the individual user and a special training procedure has been developed and tested both in the laboratory and in the hospital. Another contribution to medical telerobotics was the development of the *Stereo-Taxical* micro-manipulator for ocular surgery by Guerrouad and Vidal in 1989 at the Automatical Center of Lille in France. This was the first published report of robotic-assisted eye surgery. The system consisted of a “carrier” with x, y and z DoF and a “wrist” with 4 DoF, enabling the device to work in spherical coordinates (Roizenblatt, Edwards, & Gehlbach, 2018).

The separation distance between master and slave stations in teleoperation varies significantly depending on the application. In medical scenarios, master and slave robots may operate in close proximity, such as in the case of the Da Vinci minimally invasive surgery robot. Alternatively, some medical procedures span considerable distances, even occurring between cities or continents. An instance of long-distance tele-echography presented in (Gourdon, Poignet, Poisson, Vieyres, & Marche, 1999) where the Syrtech robot facilitated remote examinations between France and Nepal.

Table 2.4: Taxonomy of Robot Autonomy levels for HRI, H=human, R=robot (Beer, Fisk, & Rogers, 2014)

LORA	Sense Plan Act	Description
Manual	H H H	The human performs all aspects of the task including sensing the environment, generating plans/options/goals, and implementing processes.
Tele-operation	H/R H H/R	The robot assists the human with action implementation. However, sensing and planning is allocated to the human. For example, a human may teleoperate a robot, but the human may choose to prompt the robot to assist with some aspects of a task (e.g., gripping objects).
Assisted Teleoperation	H/R H H/R	The human assists with all aspects of the task. However, the robot senses the environment and chooses to intervene with task. For example, if the user navigates the robot too close to an obstacle, the robot will automatically steer to avoid collision.
Batch Processing	H/R H R	Both the human and robot monitor and sense the environment. The human, however, determines the goals and plans of the task. The robot then implements the task.
Decision Support	H/R H/R R	Both the human and robot sense the environment and generate a task plan. However, the human chooses the task plan and commands the robot to implement actions.
Shared Control with Human Initiative	H/R H/R R	The robot autonomously senses the environment, develops plans and goals, and implements actions. However, the human monitors the robot's progress and may intervene and influence the robot with new goals and plans if the robot is having difficulty.
Shared Control Robot Initiative	H/R H/R R	The robot performs all aspects of the task (sense, plan, act). If the robot encounters difficulty, it can prompt the human for assistance in setting new goals and plans.
Executive Control	R H/R R	The human may give an abstract high -level goal (e.g., navigate in environment to a specified location). The robot autonomously senses environment, sets the plan, and implements action.
Supervisory Control	H/R R R	The robot performs all aspects of task, but the human continuously monitors the robot, environment, and task. The human has override capability and may set a new goal and plan. In this case, the autonomy would shift to executive control, shared control, or decision support.
Full Autonomy	R R R	The robot performs all aspects of a task autonomously without human intervention with sensing, planning, or implementing action.

The main focus of medical robotics research has centred on surgical applications, with the da Vinci surgical robotic system standing as an example of successful implementation of teleoperated surgical robots. It performs the instructions of a surgeon and allows unconstrained automated motion which reduces the surgeon's cognitive load (Hoeckelmann et al., 2015). However, the space of medical robotics extends beyond surgery and impacts other medical domains. One such domain is telemedicine, which facilitates access to healthcare services for individuals residing in remote or underserved areas.

2.1.6 Telemedicine begins in science fiction

In the February 1925 issue of Science and Invention, Gernsback wrote an article that would combine his fascination with the future of radio communications and predict a device for the year 1975 that we still don't see in any practical household form today. Gernsback's device was called the "Teledactyl" and would allow doctors to not only see their patients through a viewscreen, but also touch them from miles away with spindly robot arms. He effectively predicted telemedicine, though with a weirder twist than we see implemented in 2012.

From the February 1925 issue of Science and Invention:

"The Teledactyl (Tele, far; Dactyl, finger — from the Greek) is a future instrument by which it will be possible for us to "feel at a distance." This idea is not at all impossible, for the instrument can be built today with means available right now. It is simply the well-known telautograph, translated into radio terms, with additional refinements. The doctor of the future, by means of this instrument, will be able to feel his patient, as it were, at a distance…. The doctor manipulates his controls, which are then manipulated at the patient's room in exactly the same manner. The doctor sees what is going on in the patient's room by means of a television screen".

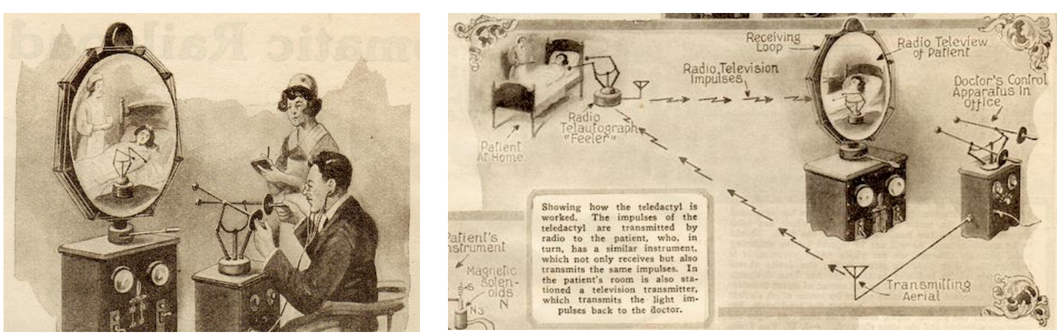

(a) *(b)*

Figure 2.4: (a) A future doctor examines a patient (predicted in 1925) (b) The *Teledactyl* diagram (Magazine & Novak, 2012)

The Teledactyl's impulses are transmitted by radio to the patient, who in turn, has a similar instrument, which not only receives but also transmits the same impulses. In the patient's room is also stationed a television transmitter, which transmits the light impulses back to the doctor.

Remarkably, the Teledactyl was envisioned as a sensory feedback tool that let the doctor to feel resistance in addition to manipulate his instruments remotely.

"Here we see the doctor of the future at work, feeling the distant patient's arm. Every move that the doctor makes with the controls is duplicated by radio at a distance. Whenever the patient's Teledactyl meets with resistance, the doctor's distant controls meet with the same resistance. The distant controls are sensitive to sound and heat, all important to future diagnosis".

Tele-echography stands out among the many telemedicine applications as a particularly promising path that can be integrated with robotics.

2.1.7 Robotized tele-echography concept

Ultrasound examinations necessitate the expertise of skilled physicians (experts), which may not always be readily available, particularly in remote geographic regions or urgent scenarios. In traditional tele-echography procedures, an expert positioned in a medical centre manipulates the ultrasound probe by a remote medical assistant to conduct examinations, with real-time ultrasound images relayed back to the supervising expert. Nevertheless, the precise and proficient manipulation of the ultrasound probe presents a challenge. To address this challenge, the concept of robotized tele-echography emerges. Within this paradigm, a robotic system (slave robot) equipped with an ultrasound probe is stationed remotely with the help of a medical staff, and it is operated by an expert situated in a master station. The expert exercises control over the motion of the ultrasound probe via a haptic (master) device, providing them with a tactile sense of the examination environment. Simultaneously, real-time ultrasound data and visual and vocal communication between the two sites are made available as illustrated in Fig 2.5.

This approach, known as robotized tele-echography, holds the potential to substantially augment the accessibility and quality of ultrasound examinations. It represents a convergence of robotics and telemedicine.

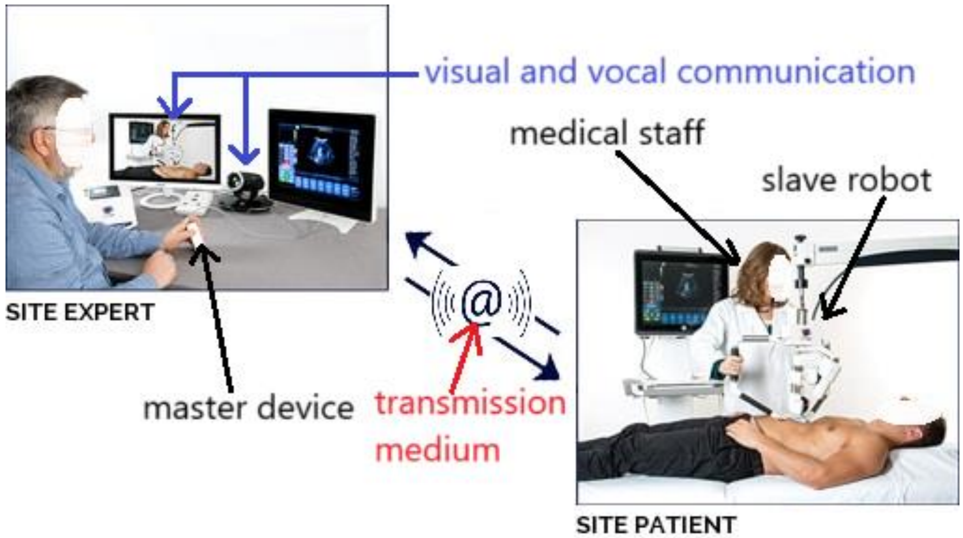

Figure 2.5: Robotized tele-echography concept. Adapted from (TIMM SANTE, 2017)

Subsequent years witnessed the development of complementary tele-echography devices through targeted projects. These included the TER robot (Vilchis, Masuda, Troccaz, & Cinquin, 2003) that replaced the assistant with a parallel robotic structure, combining cable-driven serial and parallel robotic systems for probe orientation and translation motions along the patient's body. And also, the TERESA robot (Vilchis González, 2003) for space tele-echography, and the OTELO system (Pierre Vieyres et al., 2006) which employs a slave robot structure with inverse kinematics position control. However, it requires an assistant to position the robot near the examination area. Industrial partners also contributed to this field with robots like ESTELE (Courrèges, Novales, Poisson, & Vieyres, 2009). Other example of a robotic system for tele-echography is the MELODY robot. After three years of testing, the MELODY system has been developed by AdEchoTech compatibly with the medical sector's actors. It has been commercially available since 2013 (P Vieyres et al., 2013). The PROSIT robot (Fonte et al., 2010), ReMeDi system (Giuliani et al., 2020), and others further expanded the horizons of tele-echography in healthcare. The following figures illustrate the above-mentioned robotic systems.

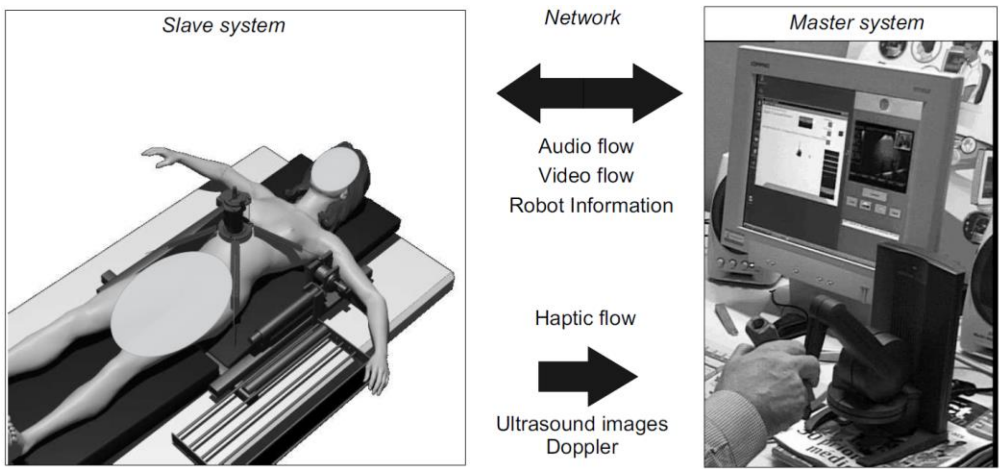

Figure 2.6: TER system overview. Adapted from (Guiochet & Vilchis, 2002)

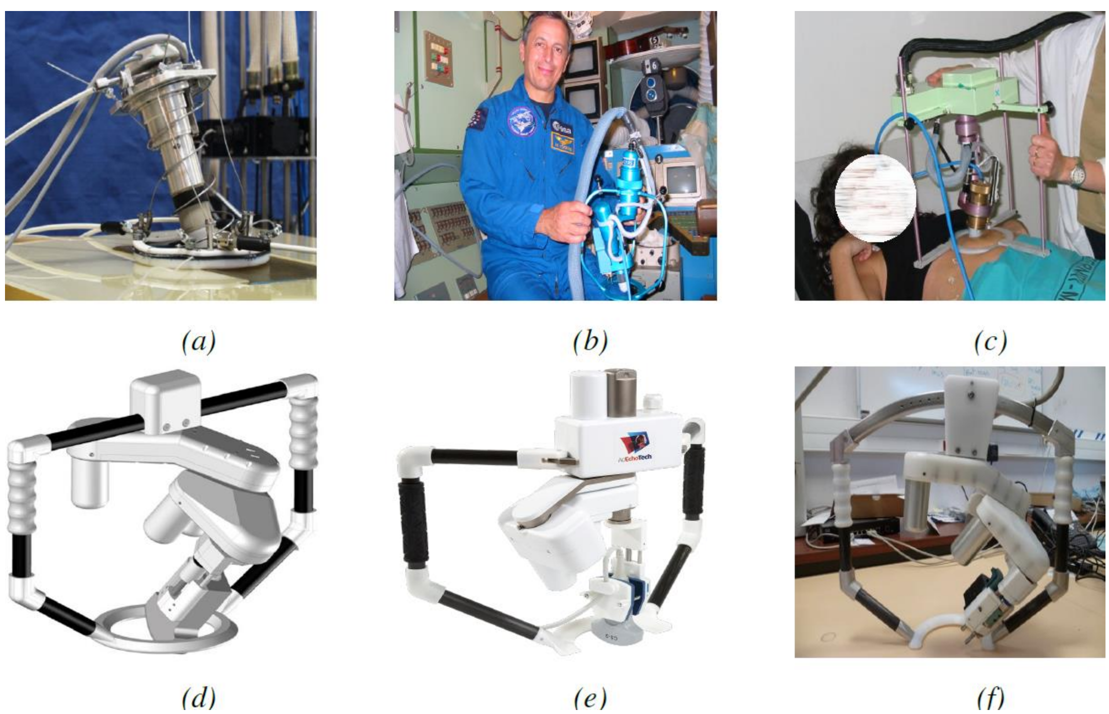

Figure 2.7: Some examples of robots for tele-echography
(a) A probe holder for TER system. (b) Teresa robot for space echography with the French astronaut Michel Tognini. (c) Otelo1 system. (d) Estele.
(e) Melody. (f) Prosit. (Joseph Diab, 2021)

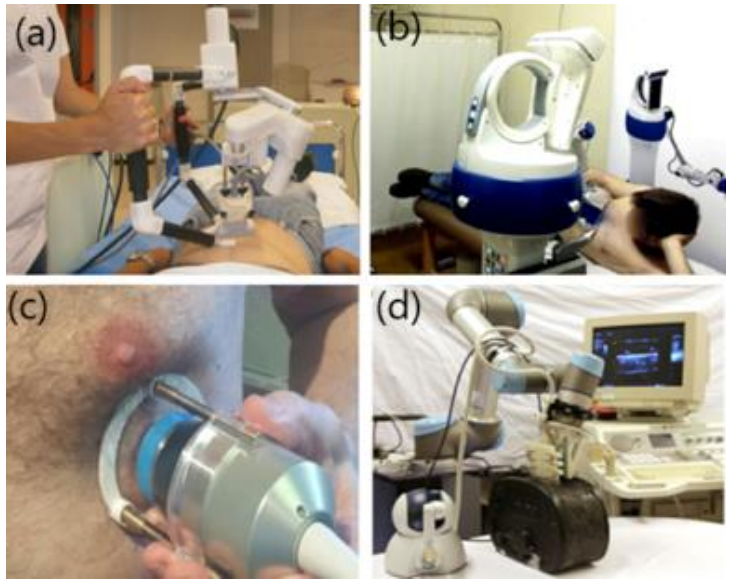

Figure 2.8: Other examples of robots for tele-echography
(a) MELODY. (b) ReMeDi. (c) TOURS. (d) Teleoperated ultrasound platform with haptic device while acquiring an imaging phantom. Adapted from (Von Haxthausen et al., 2021)

In this part, we covered the basic concepts and state-of-the-art developments in physical human-robot interaction (pHRI), with a focus on collaborative robotics, teleoperation, and medical robotics applications, particularly in robotized tele-echography. We saw how pHRI enables intuitive and safe cooperation between humans and robots in shared workspaces, referring to key challenges related to safety, precision, and efficiency. Collaborative robots (cobots) demonstrate significant potential in enhancing human performance while maintaining safety. In the domain of teleoperation, we discussed how remote manipulation through robotic systems has opened new possibilities, especially in medical robotics. Robotized tele-echography, a rapidly emerging field, represents a example of how robotics can overcome physical barriers, enabling expert medical diagnosis in real-time despite physical distance.

2.2 Robot safe motion planning

Safe robot navigation is a very important aspect of robotics. It involves so many strategies and techniques which are designed to ensure that robots can move through their environments without causing damage to themselves and others (robots or humans). This involves the development of real-time sensing systems, planning with collision avoidance algorithms, and control mechanisms.

Motion planning is finding a robot motion between a start and a goal states that avoids nearby obstacles and respects other constraints, such as joint limits (Lynch & Park, 2017).

Although most literature contributions discuss the problem for the robot and the obstacle modelled as points, the problem becomes more difficult for robot manipulators. This is because manipulators have multiple links and therefore, the planner algorithm must ensure that none of those links collides with any obstacle in the environment. When the obstacle has a complex shape that we can’t model as a point, the problem also becomes more difficult.

2.2.1 Motion planning problem types and aspects

The **path planning** is a particular case of the **motion planning** problem (Fig 2.9). It is only the geometric problem of finding a collision-free path from a start configuration to a goal one, without concern for other aspects like, robot dynamics, duration of motion, various constraints, or control inputs. The path returned by the path planner can be scaled in time to create a practical trajectory.

A motion planning problem requires an immediate result to ensure task implementation, which calls for a fast **online planner** in **dynamic environments** where obstacles can appear, disappear, or move unpredictably. **In static environments** or in the **absence of obstacles**, a slower **offline planner** can satisfy.

The robot might have fewer **control inputs** than **degrees-of-freedom**. In this case, there are some paths thar the robot can’t follow although they are collision-free.

Whether the robot reaching the **exact** goal state or an **approximate** one, this might be **satisfying**. But in some cases, we might want the planner to minimize some cost function which creates **optimal motion** (minimizes time or efforts or path’s length…).

A motion planner is **complete** if it ensures to find a solution in a finite time when it exists, and to notify when there is no possible path. In practical problems we might accept a **resolution or probabilistic completeness**.

The **computational complexity** refers to the amount of time or memory needed. It may be expressed in terms of the average case or the worst case (Lynch & Park, 2017).

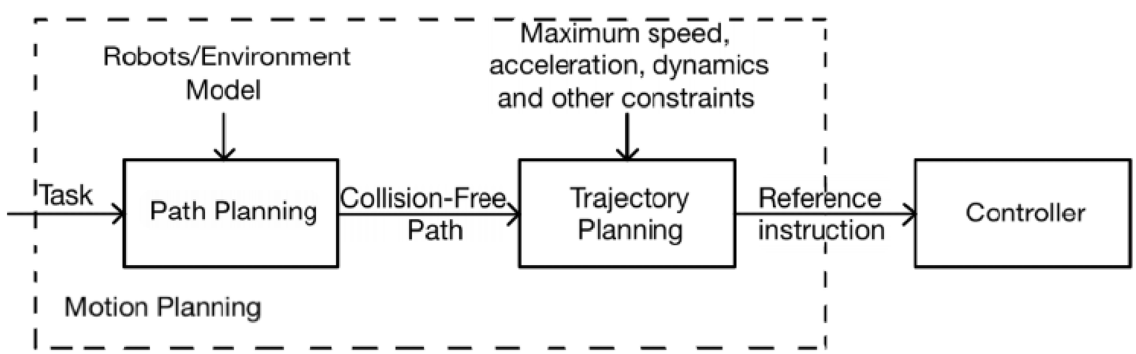

Figure 2.9: Robot motion planning problem (Liu & Liu, 2020)

2.2.2 Motion planning methods

Motion planners are classified into two categories:

- **Local** motion planners: generating a path based on local information about the environment. They operate in the immediate robot's neighbourhood. They are **reactive** methods that make decisions based on the current sensor data and local environment parameters. The path can avoid obstacles locally without consideration of optimising other parameters. They threat obstacle avoidance as a control problem (low level control).
- **Global** motion planners: they take into consideration the entire environment to find a complete path from start to end (goal) state. They are deliberative and find a high-level path. The path can avoid obstacles, optimize efficiency, and consider the various constraints.

Table 2.5: A comparison between global and local motion planners
(Gasparetto, Boscariol, Lanzutti, & Vidoni, 2015a; Lajpah & Petri, 2012; Petrič, Gams, Likar, & Žlajpah, 2015a; Kavraki & LaValle, 2008)

	Global planning methods	**Local planning method**
Advantages	Can give optimal behaviour, based on some criteria, when applied to well-defined environments. There is a guarantee of completeness if a path exists. Is done one time at the beginning of the task.	Quickly adapts to dynamic changes. Suitable when the obstacle position is not known in advance. Fast, highly responsive to changes in dynamic environments. Computationally less demanding.
Disadvantages	They are relatively slow and computationally extensive (too much data to handle) Expensive computation Less adaptive to real-time changes	May cause suboptimal behaviour. May be incomplete, no guarantee to find a valid path. May become stuck when a collision-free path cannot be found from the current configuration.
Common methods	Probabilistic Roadmap (PRM), Rapidly exploring Random Tree (RRT), A*	Artificial Potential Field (APF), Velocity Obstacle (VO)

Often, local planners are not meant to replace the global ones, but used in parallel to enable global planners improve behaviour in what we call "hybrid approaches" (L. Wang, Lim, & Jr, 2002). These latest combine the strengths of both local and global planners. A common strategy is to use a global planner to compute a rough high-level path and then employ a local planner to navigate the robot along that path while avoiding obstacles in real-time.

We need to introduce some basic definitions to understand the path planning problem and methods. The configuration space (C-space) is the space of all possible robot configurations, where a configuration, denoted q, is the specification of position and orientation of the robot. The obstacles' representation (C-obs) is the image of the obstacles in the C-space, and the space of free configurations (C-free) is defined as {C-space-C-obs} (Gasparetto et al., 2015a).

Fig 2.10. illustrates the C-space, C-free and C-obs for an articulated robot with two joints. The C-space is given by its joint space (in this case, R^2).

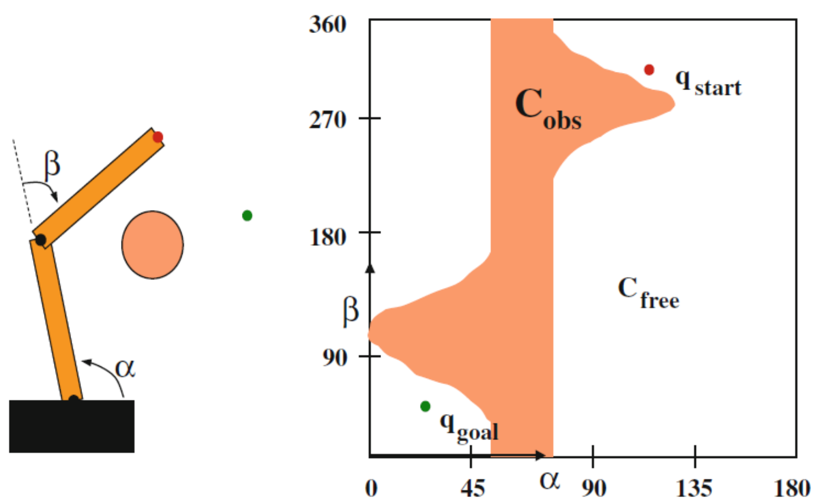

Figure 2.10: The C-space (Right), the C-free and C-obs spaces for the articulated robot with two joints represented (Left) (Gasparetto et al., 2015a)

Path planning algorithms are usually divided in three categories, according to the methodologies used to generate the geometric path, namely: roadmap techniques, cell decomposition algorithms, and artificial potential methods.

I. The roadmap techniques

These techniques depend on the reduction of the C-space to a set of one-dimension paths to search. So, this approach maps the C-free connectivity into a system of one-dimensional curves called the roadmap. The roadmap obtained contains a set of paths. In this way, the path planning consists in linking the initial and final configurations to the roadmap. Usually, a graph is associated to the roadmap and some optimality index is defined (e.g. the Euclidean length). Then, we can search the optimal solution in the graph (often represented by the shortest path). One kind of roadmap is called *visibility graph*, i.e. the graph whose nodes are the vertices of all the obstacles in the configuration space. Searching the graph would usually lead to get the shortest Euclidean path in the C-space. The nodes of the graphs indicate point locations, while edges represent visible connections between the nodes. Another kind of roadmap algorithms is based on what it is called the *Voronoï diagrams*. In which, the space is divided into regions. A region Ri contains all points closer to a point Pi than to any other point Pj(j≠i) in a given set of points, also called germs, {P1,…Pn}. The Voronoï diagrams allow to obtain a path at the maximum distance from the obstacles, whereas the visibility graph produces a path as close as possible to the obstacle vertices (Gasparetto et al., 2015a).

Fig 2.11 shows some path generated by using Voronoï diagrams. Obstacles are represented by three squares, while the blue lines are the set of points equidistant from at least two obstacles. The paths resulted using this technique are as far away as possible from nearby obstacles.

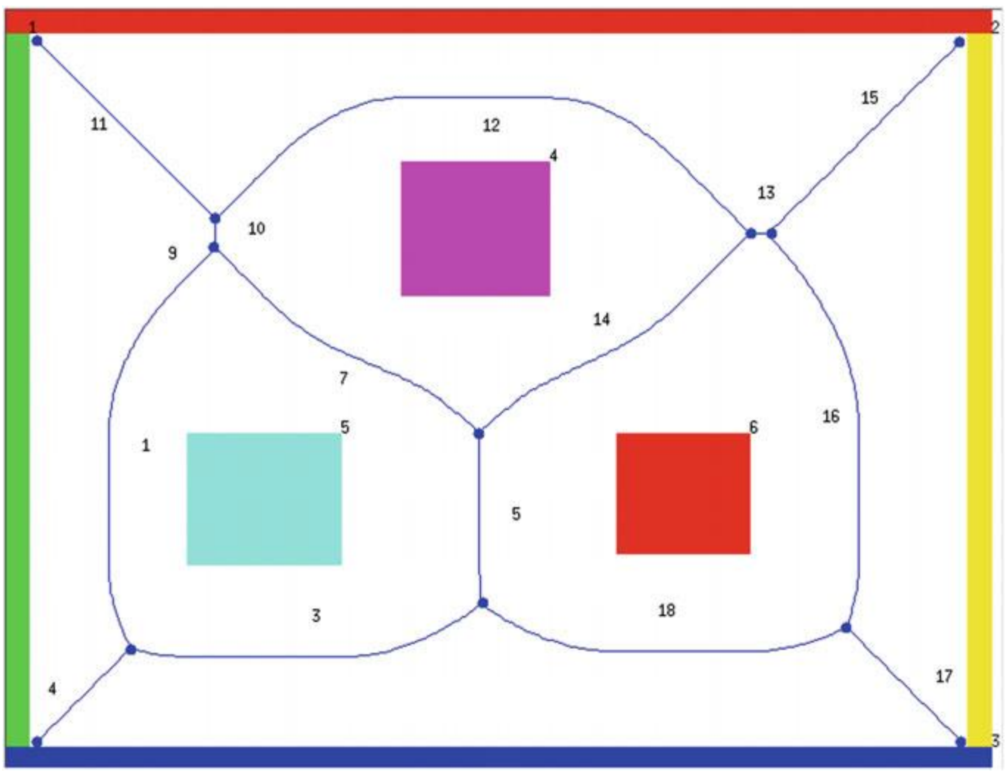

Figure 2.11: Paths resulting from Voronoï diagrams (Gasparetto et al., 2015a)

II. The cell decomposition (grid) methods

These methods discretize the C-free into a grid (several regions called cells) and search the grid for a motion from initial configuration q_{start} to a grid point that exists in the goal region (Lynch & Park, 2017). The adjacency relations between cells are represented in what we call *connectivity graph*. Namely, the nodes of the graph represent the cells extracted from the free space, and there is an arch between two nodes are connected if and only if the corresponding cells are adjacent. Hence, path planning becomes a graph-searching problem (Gasparetto et al., 2015a). These methods can return optimal solutions but, they have a fixed resolution, they need extra memory to store the grid data and need time to search it. Their complexity increases highly with the number of space dimensions.

Fig 2.12: show an example of exact cell decomposition technique, the union of the cell represents exactly the free space. In some cases, an exact computation of the free space is not possible or convenient. Approximate cell decomposition methods must therefore be employed.

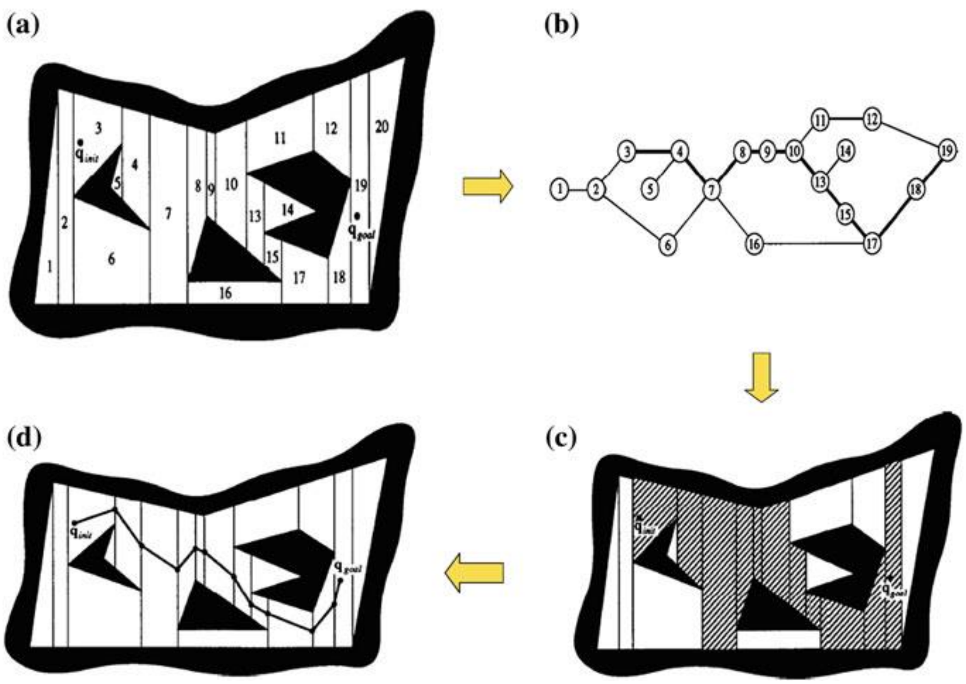

Figure 2.12: Exact cell decomposition
(a) subdivision of space into numbered polygons, (b) connectivity graph, (c) regions to be crossed, (d) computed path (Gasparetto et al., 2015a)

III. Sampling methods

From the cell decomposition principles, we can notice that they require an explicit construction of the Configuration space obstacles C-obs, which is not intuitive (sometimes impossible) in practice especially for complex environments. The key idea behind sampling-based algorithms is to avoid this issue by performing a search test in a sample from the C-space. A generic sampling method relies on:

- A random (or deterministic) function to choose a sample from the C-space
- A function to evaluate whether the sample is in the C-free

- A function to determine the “closest” previous C-free sample
- A local planner to try to connect to, or move toward, the new sample

In these methods, we need to construct a graph or a tree to represent possible robot motions. Sampling methods tend to be probabilistically complete and can even solve high DoF motion planning problems. However their solutions are not optimal but satisfying and have significant computational complexity (Lynch & Park, 2017). Comparing to the human way of motion planning, humans do not follow entirely multiple paths for the same situation, we can argue that these methods are so different due to the randomness they have. This randomness is a good tool for exploration but in real-time, where planners have short time to find a right sequence of actions, a significant bias away from the goal is possible to exist, especially if the goal is dynamic. So many techniques to perform this sampling exist in literature. The most common ones are based on random trees, probabilistic roadmaps, and A* search algorithm.

A) The rapidly exploring random trees (RRTs)

The RRT is a common incremental sampling-based algorithm that searches for a collision-free motion from an initial to a goal state. It is applied to kinematic problems, where the state x is simply the configuration q, as well as to dynamic problems, where the state includes the velocity (Lynch & Park, 2017). In these situations, path planners take into account kinematic and dynamic constraints of the robot. This problem is referred to as kinodynamic motion planning. It allows to search nonconvex high-dimensional spaces by randomly building a space-filling tree (Gasparetto et al., 2015a).

Some other versions of the classical RRT have been proposed in literature to inhance some aspects. One of them, “Bidirectional RRT” which grows two trees: one “forward” from the start point and one “backward” from the goal point. Another one “RRT*” is a variation on the single-tree RRT that continually rewires the search tree to ensure storing only the shortest path. The method is computationally demanding especially when high resolution is needed. Fig 2.13 shows a comparison done between the classical RRT and the RRT* version to find the shortest path.

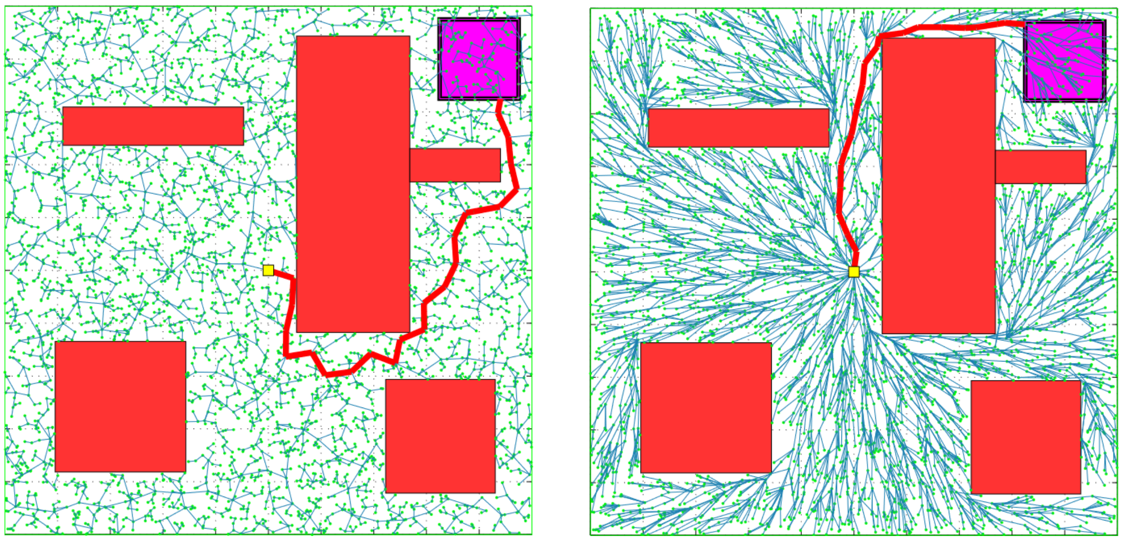

(a) (b)

Figure 2.13: (a) The tree generated by a RRT (b) The tree generated by RRT*
The goal is the square at the top right corner, the shortest path is indicated (Lynch & Park, 2017)

B) The probabilistic roadmaps (PRMs)

The basic idea is using probabilistic algorithms, such as random sampling, to construct the roadmap. They consider a graph whose nodes are consistof a set of random configurations in the C-free. A local planner can then try to connect these configurations using a path. Whenever a path is found, a new node is added to the graph. Hence, the graph reflects the C-free connectivity. In order to find a path between two configurations, they are added to the graph to perform a search in order to find a path (Gasparetto et al., 2015a).

In order to tackle moving obstacles, dynamic roadmap methods are used. They depend on the standard PRM which creates a roadmap that represents the C-free connectivity in a preprocessing phase to plan the robot motion. A local planner is used to modify the robot path to avoid dynamic obstacles in real time.

C) The A* search algorithm

The A∗ algorithm proposed in 1968 is a global optimal planner which depends on designing a heuristic function to estimate the path's cost. The direction of the path search is determined by the cost function. In each search iteration, the cost function value of each child node (the nodes near the parent node) is calculated, and the child node with the smallest cost function value is assignded to the parent node in the next iteration. Then, the final path result is searched. A* is so much utilized in path planning due to its low complexity, high efficiency, and global optimality. Fig 2.14 presents the results of collision-free path planning for a robot manipulator using two versions of the A* method. The one in the left shows the shortest path A* proposed in (Tang, Zhou, & Xu, 2024).

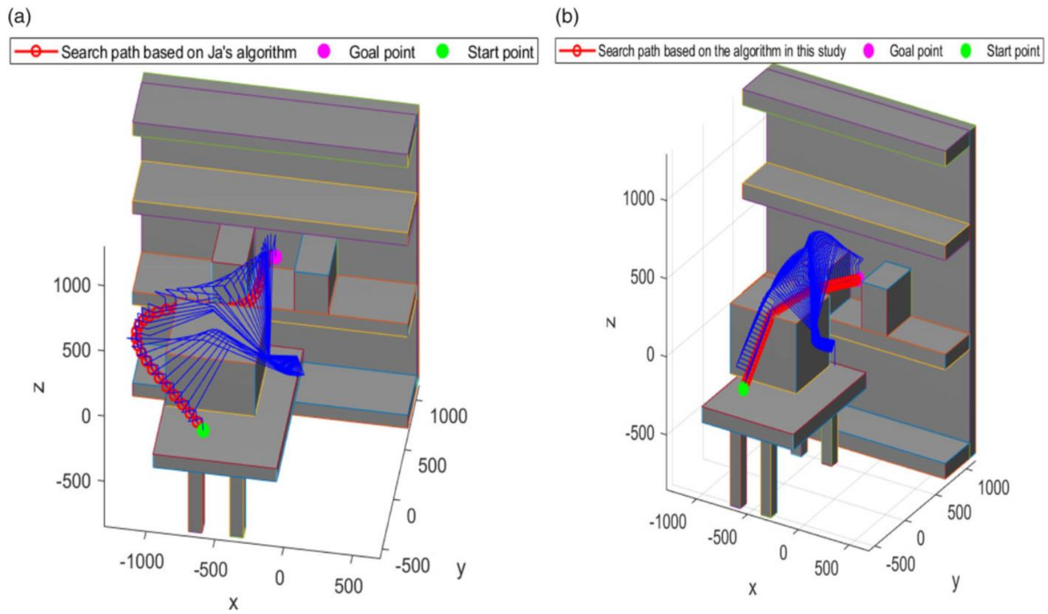

Figure 2.14: Motion planning with obstacle avoidance for robot manipulator
Path trajectory (a) with an old A* method (b) with A* proposed by (Tang et al., 2024)

Although graph-based search or tree-based search algorithms are complete and optimal, on close observation, we find the following shortcomings with them:

- They have a blind behaviour. The algorithm cannot foresee the possibility of an obstacle in the very first step to avoid expanding nodes in the obstacle's direction.
- The tree-based algorithm may expand in the neighbourhood of a tree branch that has already been closed from earlier steps which results in a computation waste.

There are some other issues related to using traditional A* planner for robot manipulators in 3D environments:

- Due to the 3D aspect and the existing obsracles, the calculation speed will be drastically reduced.
- A* suggests the robot to be a point and only considers whether this point collides with obstacles. But in practice, the relationship between the manipulator's segments, the end position of the robot, and the obstacles need to be considered when planning a path for a robot manipulator.

Due to the above-mentioned shortcomes of the traditional graph-based and tree-based algorithms in practical applications, there have been some propositions to modify the algorithm to consider these issues. However, these modifications contains usually hybrid approaches that uses multiple techniques. Some of them use the Artificial Ptential Field (APF) local planner in parallel to reply to plan for in dynamic obstacles situations to inhance realtime behaviour.

IV. The Artificial Potential Field (APF) methods

The concept of artificial potential fields was introduced into motion planning by (O. Khatib, 1985). In the potential field method, an artificial potential field is assigned to the robot workspace space. The obstacle is assigned a repulsive potential while the goal state is assigned an attractive potential. Then, the path is calculated using the gradient of the total artificial potential. Virtual potential field produces virtual forces that pull the robot toward the goal while pushing it away from obstacles. The approach is relatively easy to implement, even for high-Dof systems, and fast to evaluate, often allowing online implementation (Lynch & Park, 2017). An example of the application of the artificial potential method is shown in Fig 2.15. This technique has applications in various fields, because it can be easily implemented online. Which means that the obstacle avoidance problem is no longer performed in the high and slow level of path planners but in the low and fast level of online motion controllers. This leads to the reactivity to environment changes detected by the robot sensors. Thus, the robot controller can fast manage unexpected workspace changes (Gasparetto et al., 2015a).

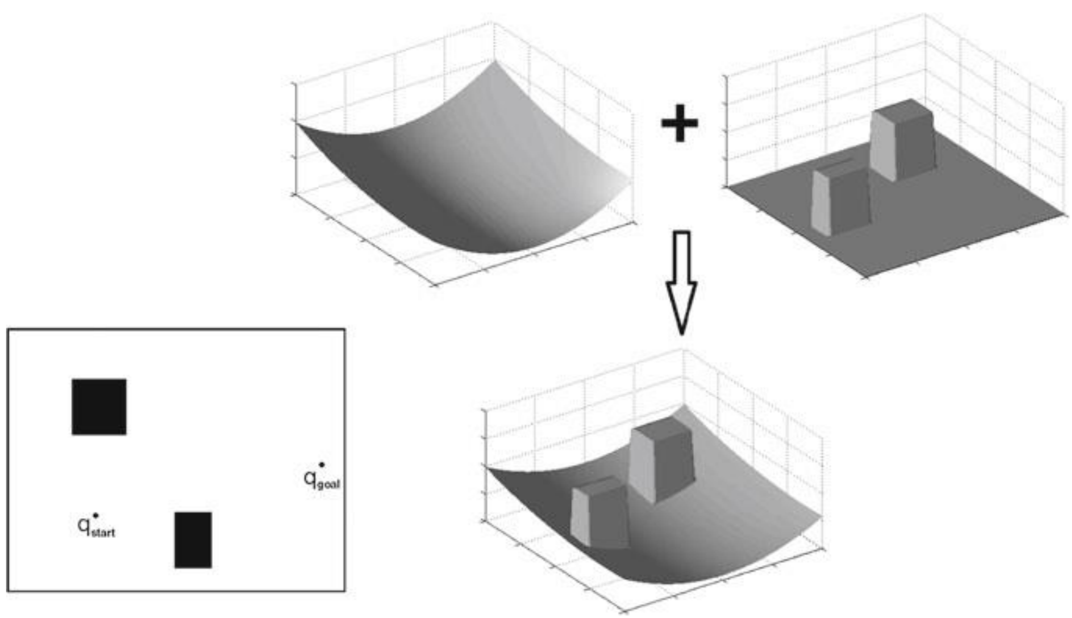

Figure 2.15: The artificial potential method (Gasparetto et al., 2015a)

However, the artificial potential methods intrinsically suffer from a major problem, which is the presence of local minima, where the robot may get stuck in configurations where the attractive and repulsive forces cancel each other but the robot has not reached the goal state yet. A local minimum acts like an attraction area and traps the robot, preventing it to reach the global minimum which is supposed to be at the final state.

In order to overcome this problem, several solutions have been proposed in literature: for instance, search algorithms have been used to address this problem but at the cost of expensive computation. Another approach depends on avoiding of local minima generation by adding some auxiliary potentials. Some other approaches use potential functions which do not have local minima (also called navigation functions). Another approach to solve the path planning problem using Random Path Planners (RPPs). In this planner, local minima are avoided by combining the artificial potential field concept with random search techniques.

In robot manipulators, multiple control points are placed along the robot to make sure the entire robot avoids collisions and not just the end-effector. The forces on the control points are translated to joint torques which are applied to the robot. That makes the robot manipulator move around the obstacle.

The potential-field method is also suitable for self-collision avoidance, if this problem may not be solved by the joint bounds already.

Various mathematical formulations have been used in literature to define the artificial potential fields and various strategies have been devised to find a path using the gradient of the total artificial potential. This will be more investigated in the next two chapters.

V. Other obstacle-free path planning methods

In addition to the APF method, there are some other local methods used in literature that depends on reactive control and can plan collision-free paths in real-time.

Nonlinear optimization: The motion planning problem is converted in these methods to a nonlinear optimization (QR) problem by representing the path or controls with a finite number of parameters. The problem turns to solve for the parameters that minimize some cost function while respecting some constraints on the goal, obstacles, and controls (Lynch & Park, 2017). These methods can produce near optimal solutions. When the objective function or the solution space are not convex, the optimization process can get stuck far away from a feasible solution (Lynch & Park, 2017). In (Faverjon & Tournassoud, 1987; Vaillant et al., 2016) a *velocity damper* is added as an extra constraint to the QP problem. When the distance between the robot and obstacle is lower than some threshold, the constraint is activated. The distance derivatives are needed to calculate the QR solution. However, calculating the distance and its derivatives for dynamic obstacles is not an easy task and can produce jerk due to derivative noise as we expect.

Danger fields: It is similar to the APF method but also takes into account the relative movement between the robot and the obstacle (Ceriani, Zanchettin, Rocco, Stolt, & Robertsson, 2015). A special form called *kinetostatic* danger field (Lacevic, Rocco, & Zanchettin, 2013), takes into consideration the velocity vector’s norm and the relative angle between the velocity and position vector. Danger field increases with the velocity norm and with relative angle also (when the motion is more oriented to a given point). This method suffers from local minima problem like the APF one.

Escape velocity: Like danger field method, escape velocity is similar to the artificial potential field method. It depends on identifying the closest robot points to the obstacle (critical points) then to give them some velocity the move the link away (Xiao & Zhang, 2016; Zhang & Wang, 2004). Computer vision is used in (Flacco, Kroger, De Luca, & Khatib, 2012) to calculate the so-called *depth space* which is then used to calculate the distance between the robot and the obstacle. Similarly to the latest method, a repulsive vector is used to drive the robot away. In this method, all obstacle points are considered instead of using only the closest point as in (Xiao & Zhang, 2016). This can be improved by estimating the obstacle velocity and the robot is controlled in a direction different from the obstacle velocity vector. In (Lajpah & Petri, 2012; Petrič et al., 2015a), authors used the robot redundancy to perform the obstacle avoidance as a secondary or primary task in the robot's null space at the kinematic level (Fig3.12a) and at dynamic level (Fig3.12b). they assigned a virtual velocity or force to drive the critical points away from the obstacle.

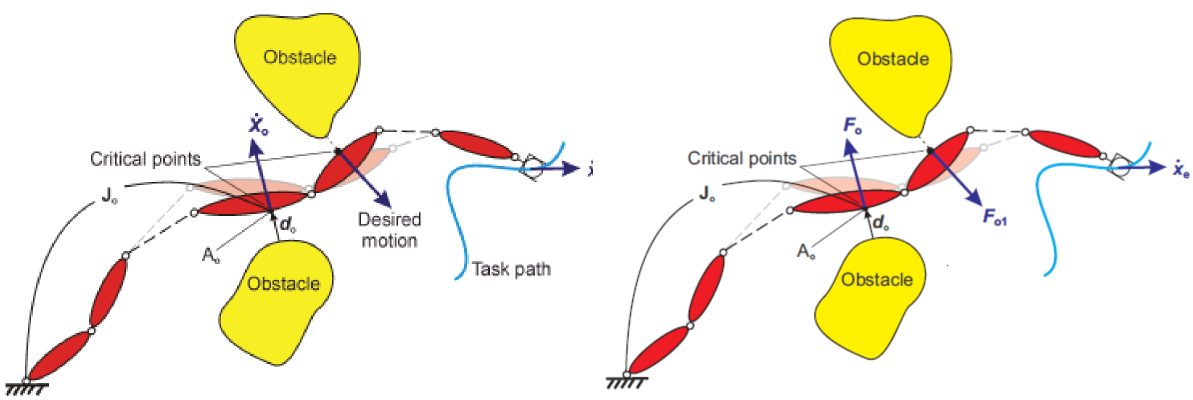

(a) (b)

Figure 2.16: Manipulator motion in presence of some obstacles
(a) using kinematic control (b) using virtual forces (Lajpah & Petri, 2012)

Although authors used this reactive control-based method for redundant robot manipulator (*Kuka LWR*), it can be used for 6-DoF robots like *Universal Robot URx* when only end-effector position is considered.

As we can notice, these reactive methods have a similar principle the Artificial Potential Field one with some variations which allow us to classify them as other versions of the traditional APF planner.

2.2.3 Collision-free path planning for robot manipulator in cPETRUS project

In robot systems design, in addition to technological choices, the questions of robot enrolment, workspace adaptation, aspects choices, path planning generation, etc. have always been major obstacles to robot development. In particular, the obstacle avoidance issue has been a major challenge for roboticists.

We have seen in the previous chapter that the robot-assisted medical application imposes some challenges (described earlier in chapter 1) which requires an automatic algorithm to ensure collision-free path planning during teleoperation to increase safety.

At present, there are many methods for obstacle avoidance in path planning of manipulators, including C-space methods, Artificial Potential Field, force field, visibility graph, pre-processing-planning algorithm, topology method, or fuzzy logic algorithm (Chotiprayanakul, Liu, Wang, & Dissanayake, 2007; Gasparetto, Boscariol, Lanzutti, & Vidoni, 2015b; Jiang, Fang, He, & Yan, 2018; lajpah & Petri, 2012; Petrič, Gams, Likar, & Žlajpah, 2015b). Other methods like minimum seeking algorithms, genetic algorithms, and spline-based algorithms can be found with a discussion on trajectory planning in (Iqbal, Islam, Abbas, Khan, & Ajwad, 2016). These methods can be classified into two main categories: global and local ones. Global methods are devoted to finding a collision-free path from the start pose to the goal pose if such a path exists. However, they are computationally heavy and therefore not applicable for real-time control (Kivelä, Mattila, Puura, & Launis, 2017).

Since our focus is on local planning to avoid collision in structured environments, we chose to use reactive control methods like APF which is faster than other numerical Jacobian-based inverse kinematics methods (S. O. Park, Lee, & Kim, 2020a). And also APF was noted by Hoy in (Hoy, Matveev, & Savkin, 2015) to be faster than other local planning methods. Artificial potential field-based approaches in addition to being very fast, they have a strong mathematical basis, can be performed online, don't waste too much computation, and seem intuitive.

One of the most important procedures to perform before collision avoidance, is measuring distance between the robot manipulator and the obstacle to determine the possibility of collisions. Since computing this distance using accurate topology is very time consuming, many researchers have been trying to find efficient approaches to speed up the calculation. For example, covering the links of a robot manipulator with polytope, polyhedron, sphere, ellipsoid, etc. which can significantly reduce computing time (Chotiprayanakul et al., 2007).

As far as we know, no previous research has investigated path planning inside hollow shaft cylindrical obstacles. However, only a few studies proposed algorithms to detect cylinders (Chittawadigi & Saha, 2013; J. Ketchel & Larochelle, 2006; J. S. Ketchel & Larochelle, 2005; Michael, 2010). In all these works, the obstacles were occluded, the planned paths had to be outside them, and the repulsive field has unique distribution in contrast to our situation.

There have been numerous studies that have investigated this issue. An artificial vision system was used in semi-automatic obstacle avoidance with a human operator who remotely operated a robotic arm for live power lines maintenance (Aracil et al., 1998). The technique used a supervisory control architecture. Advantages of this, in contrast to a manual operation, are a higher level of protection, safety for the worker and quickness. However, it had some disadvantages related to the higher complexity and cost. Another method that depends on using the distance between the robot and the obstacle allows to filter the velocity received from the operator so that the robot stops smoothly when reaching to a specified threshold from the obstacle (Feddema & Novak, 1994). As a result, the control system restricts motion in the direction of obstacles while permitting unconstrained motion in other directions. The method was applied to a teleoperated PUMA 560. In (Garcia-Hernandez & Parra-Vega, 2009), potential field method is used to generate a virtual force, transformed into a torque on the haptic device to restrict the human operator motion through force feedback which improved the task execution time, system safety and increased the information for the operator about the robot and the environment. However, it still assigns a part of the effort to avoid the obstacle to the human. A similar work in (Zhong & Hauser, 2022) is used to detect obstacles using attentiveness map estimation (AME) and uses haptic feedback to inform the human operator to avoid obstacle himself. Another technique that depends on integrating the whole arm obstacle avoidance goal in an online optimization problem that considers also the enhancements of the tracking error and joint limits at the same time for a unilateral teleoperated system (Portillo-Velez, Rodriguez-Angeles, & Cruz-Villar, 2009). Li et al. in (Li, Song, Li, Lu, & Mao, 2012), proposed a method for redundant manipulator obstacle avoidance in teleoperated task. It is based on equipotential surface inspired from the artificial potential field concept. After projecting the robot links and the obstacle on the equipotential surface, authors computed distances and equivalent virtual velocity to guide the robot away from the obstacle. Then, they profited from the redundancy to change the robot configuration without affecting on the main task. Another technique is used in (Torres et al., 2015) to integrate automatic obstacle avoidance in teleoperated concentric tube robot. It depends on precomputing a roadmap of collision-free robot configurations based on a description of the anatomical obstacles, which are obtained via volumetric medical imaging.

Integration of Artificial Potential Field (APF) approach into a multi-level robot control structure will improve the real-time performance of the overall robot control system (Oussama Khatib, 1986). Thus, it can be used for obstacle avoidance in robot arm teleoperation tasks. However, it is mainly used for obstacles that have simple or regular geometric shapes to facilitate modelling of their potential fields and their mathematical expression.

In APF, a virtual attractive force is applied to the robot arm's target position, while repulsive forces are applied to any obstacles in the robot arm's environment (Oussama Khatib, 1986). The resulting force vector determines the direction and magnitude of the robot arm's movement and is used to guide the robot away from obstacles and towards the target position. However, this technique can also have some limitations, such as the possibility of getting stuck in local minima or the need for careful tuning of the potential field parameters to achieve effective obstacle avoidance (Elahres, Fonte, & Poisson, 2021).

2.2.4 Obstacle Avoidance in Teleoperation based on Artificial Potential Field

Although a major trend in recent years has been toward sampling methods, which are easy to implement and can handle high-dimensional problems (Lynch & Park, 2017), we will focus on APF method due to their properties mentioned earlier. Which can suit well to be integrated in teleoperation tasks. Teleoperation often requires real-time responsiveness.

Artificial Potential Fields (APF) are suitable in such applications due to several advantages. Based on simple mathematical formulations of attractive and repulsive forces, APF can compute the forces quickly. This leads to immediate reaction, necessary for teleoperation. The straightforward and computationally light calculations in APF which allows the system to run the algorithm in real-time.

The human-like concept of repulsive and attractive fields is easy to understand, making the robot’s behaviour more predictable and easier for teleoperators to anticipate and interact. With a good choice for the potential field expression, APF can generate smooth paths, which are preferable for teleoperation as discontinuity in direction can be difficult for human operators to deal with and can lead to unsafe movements.

APF method requires few parameters to tune which makes it easy to implement and integrate with teleoperation. Finally, with appropriate modifications, APF can be designed to plan in dynamic environments by updating the virtual forces based on sensor feedback.

However, APF can get trapped in local minima where the robot gets stuck in a position different from the goal. However, in addition to local minima traditional solutions that exist in literature, and in a teleoperation scenario, the human operator can intervene to guid the robot to escape these local minima.

The following chapter will present a dedicated method to collision-free path planning algorithm and its validation. This method is developed based on the APF concept to avoid collision with a whole robot manipulator. And it proposes a repulsive field model for hollow cylindrical obstacles. The robot is modelled with poly-articulated cylinders in the obstacle detection.

CHAPTER 3
Motion planning with obstacle avoidance using the Artificial Potential Field (APF)

In this chapter, we describe the development and evaluation of an Artificial Potential Field (APF) method for collision-free path planning for a robot manipulator. The proposed algorithm uses APF to guide the robot from an initial to a desired position and orientation, avoiding spherical and hollow cylindrical obstacles. The robot (in fact a cobot), an *UR5* (Fig 3.1) from *Universal Robots*, is modeled using a poly-articulated cylinder model to measure the distance to the obstacle. more informations about *UR5* exist in APPENDIX A.

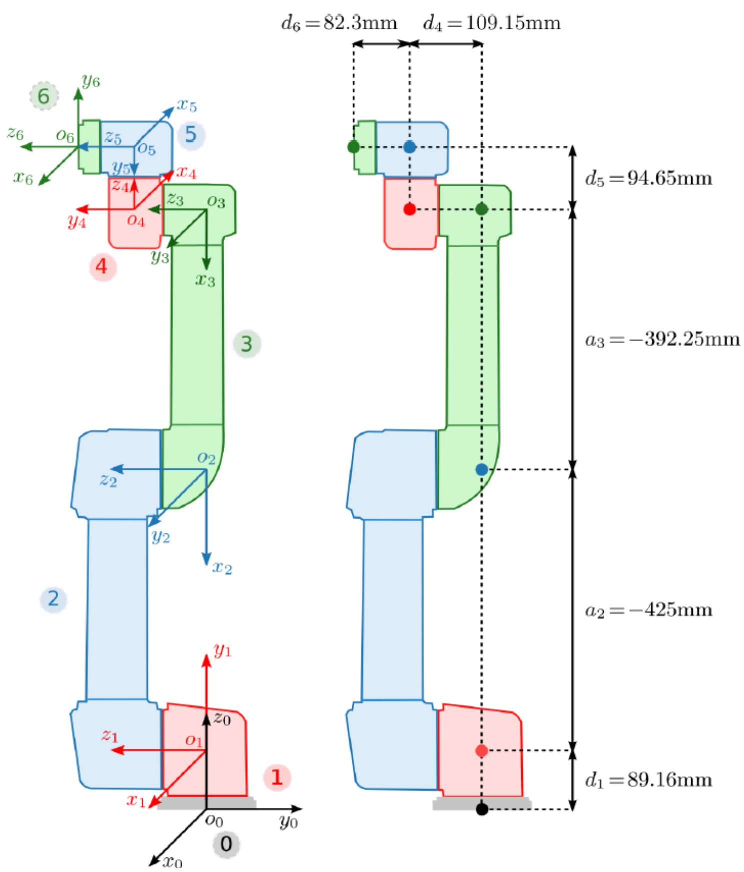

Figure 3.1: (Left) the coordinate frames assigned to each link of the *UR5* manipulator according to the DH convention (Right) the DH parameters (Kufieta, 2014)

3.1 Robot manipulator model

This study is based on the integration of the *UR5* cobot from *Universal Robots* company which is a lightweight 6 *DoF* robot designed for safe direct interaction.

From the *Universal Robots* datasheet, we defined the modified *Denavit-Hartenberg DHm* (Denavit & Hartenberg, 1955; Khalil & Kleinfinger, 1986; Reddy, 2014; H. Wang et al., 2014) parameters (*Universal Robots*, 2020) given in Table 3.1. More information about both *DHm* table and *UR5* kinematics is found in APPENDIX A.

The reference frame R_0 (O_0, x_0, y_0, z_0) of the environment is located at the robot's base were z_0 axis is vertical and the origin O_0 is placed on the bottom plane of the robot.

Table 3.1: Modified Denavit-Hartenberg table (DHm) for the 6-DoF *UR5* robot
Parameters are given in (mm) and (rad), adapted from (Guoxian & Liang, 2020; Kufieta, 2014)

Link i	a_{i-1}	α_{i-1}	d_i	θ_i
1	0	0	89.159	θ_1
2	0	π/2	0	θ_2
3	- 425	0	0	θ_3
4	-392.25	0	109.15	θ_4
5	0	π/2	94.65	θ_5
6	0	-π/2	82.3	θ_6

With respect to the *DHm* approach, the homogeneous transformation ${}^{i-1}T_i$ between the nearby frames R_i and R_{i-1} is given in the next 4x4 matrix (Reddy, 2014).

$$ {}^{i-1}T_i = \begin{bmatrix} c\theta_i & -s\theta_i & 0 & a_{i-1} \\ s\theta_i c\alpha_{i-1} & c\theta_i c\alpha_{i-1} & -s\alpha_{i-1} & -d_i\alpha_{i-1} \\ s\theta_i s\alpha_{i-1} & c\theta_i s\alpha_{i-1} & c\alpha_{i-1} & d_i\alpha_{i-1} \\ 0 & 0 & 0 & 1 \end{bmatrix} \quad \text{(Eq 3.1)} $$

With, c and s denote repectively cosinus and sinus.

The global transformation ${}^0T_6$ relation is then:

$$ {}^0T_6 = {}^0T_1\,{}^1T_2\,{}^2T_3\,{}^3T_4\,{}^4T_5\,{}^5T_6 \quad \text{(Eq 3.2)} $$

The above transformations were used in order to compute the 6x6 Jacobian matrix of the transformation and robot links extremities positions. These particular points afterwards are used in the APF algorithm. In addition, the algorithm evaluates and uses the Jacobian matrices at certain critical points precomputed during the execution, which obliges to express the general form of Jacobian inspired by (Kufieta, 2014; Spong, Hutchinson, & Vidyasagar, 2006) as follows:

$$\begin{bmatrix} w_n^0 \\ v_n^0 \end{bmatrix} = J_n^0 \dot{q} \tag{Eq 3.3}$$

Where v_n^0 and w_n^0 are the linear and the angular velocity vectors of the end effector frame R_n expressed in inertial frame R_0, respectively. In this case, the Jacobian J_n^0 is given by:

$$J_n^0 = \begin{bmatrix} J_w \\ \hline J_v \end{bmatrix} \tag{Eq 3.4}$$

In case of fully revolute manipulator, the upper and lower half of the Jacobian are given as:

$$J_w = \begin{bmatrix} z_0 & \cdots & z_i & z_{n-1} \end{bmatrix} \tag{Eq 3.5}$$

$$J_v = \begin{bmatrix} z_0 \times (O_n - O_0) & \cdots & z_i \times (O_n - O_i) & z_{n-1} \times (O_n - O_{n-1}) \end{bmatrix} \tag{Eq 3.6}$$

(Eq 3.7)

With z_n and O_n: the z axis and the origine of frame R_n. We can get the Jacobian at an arbitrary robot point located on link j by replacing O_n with the position of the arbitrary point and setting the last $n - j$ columns to $[0 \quad \ldots \quad 0]^T$ as described below. Let $r_{P_j}^0$ a vector pointing to an arbitrary point P on link j, expressed in the inertial frame R_0, the Jacobian $J_{P_j}^0$ is then (Kufieta, 2014):

$$J_{P_j}^0 = \begin{bmatrix} z_0 & \cdots & z_{j-1} & 0 & \cdots & 0 \\ z_0 \times (O_n - O_0) & \cdots & z_{j-1} \times (O_n - O_{j-1}) & 0 & \cdots & 0 \end{bmatrix} \tag{Eq 3.8}$$

3.2 Robot manipulator collision model

The *DHm* model explained earlier allows us to determine the position of each point on the robot multiple links with considering the latest as a cylinder with a certain diameter. This led us to model the robot as poly-articulated cylinders while measuring the distance to the obstacle. For each link, we precise a resolution and divide the link axis to a number of points. Then we measure the distance between each of those points and the obstacle. From each link, the nearest point to the obstacle is considered a “critical point” (a collision point $P_{cr,i}$ demonstrated in Fig 3.5) if the distance is less than some predefined threshold. After precising those critical points, we can assign a virtual repulsive force for each of them using the APF formula proposed later.

3.3 The Artificial Potential Field method

As mentioned in chapter 2, the Artificial Potential Field (APF) is a traditional path planning method proposed by Khatib (1985) to ensure real time obstacle avoidance for a mobile robot and has made a great achievement as a path planning method for robotic arms. The basic idea of APF is to make the robot move toward the target while being influenced by the attractive and repulsive forces which are generated from the target and the obstacle, respectively.

3.3.1 Attractive forces

During the procedure, the robot starts from the initial position and moves along the potential field's descent path to reach the target point. The potential functions are designed as follows:
The force generated from attractive potential:

$$F_{att} = k_{att,p}(P_f - P_c) \qquad \text{(Eq 3.9)}$$

Where F_{att}, $k_{att,p}$, P_f, P_c are the virtual attractive force, proportional coefficient, target position and current position of the end effector, respectively. In order to plan the orientation of the end effector, we define a virtual momentum to affect the orientation of this end effector as follows:

$$M_{att} = k_{att,o} e_o \qquad \text{(Eq 3.10)}$$

Where M_{att}, $k_{att,o}$, e_o are the virtual attractive momentum, proportional coefficient and orientation error, respectively. Direct computation of the orientation error requires the use of the Euler angles which suffers from representation singularities. To overcome this drawback, this error is calculated based on unit quaternion representation. Let $Q_f = (\eta_f, \varepsilon_f)$ be the quaternion defined by the target orientation of the robot end effector. Where η_f, ε_f are the scalar and the vector parts of Q_f, respectively. And $Q_c = (\eta_c, \varepsilon_c)$ the quaternion defined by the current orientation. Also, η_c, ε_c are the scalar and the vector parts of Q_c, respectively. Then the orientation error is given by this equation (Aguilar & Sidobre, 2006; Campa & Camarillo, 2008; Kivelä et al., 2017):

$$\text{s}e_o = \eta_f \varepsilon_c - \eta_c \varepsilon_f + S(\varepsilon_f)\varepsilon_c \qquad \text{(Eq 3.11)}$$

Where $S(\varepsilon_f)$ is the skew-symmetric matrix for the ε_f.

Then, the attractive torque affecting all the joints can be calculated using the Jacobian J:

$$T_{att} = J^T \begin{bmatrix} M_{att} \\ F_{att} \end{bmatrix} \quad \text{(Eq 3.12)}$$

3.3.2 Repulsive forces

To detect the distance to the obstacle, each robot link is considered a cylinder as described earlier. Then each cylinder axis is divided into a certain number of points. After that, the distance between each point of those and the obstacle is measured to determine the nearest point from each link to the obstacle. If the latest point is in the range of the repulsive field, then it is considered as a critical point $P_{cr,i}$ and a repulsive force is assigned to it. We propose the expression of the force generated from repulsive potential at one critical point as:

$$F_{rep,i} = k_{rep} \frac{1}{\|\Delta X\|} \frac{P_{ob,i} - P_{cr,i}}{\|P_{ob,i} - P_{cr,i}\|} \quad \text{(Eq 3.13)}$$

Where $F_{rep,i}, k_{rep}, P_{cr,i}, P_{ob,i}, \|\Delta X\|$ are the virtual repulsive force affecting the critical point $P_{cr,i}$, a proportional coefficient, the critical point $P_{cr,i}$ on the robot and nearest point on the obstacle $P_{ob,i}$ to the critical point $P_{cr,i}$ on the robot, and the distance between critical point i and nearest point on the obstacle respectively.

The poly-articulated robot is a highly coupled structure, and the repulsive force generated from the obstacle on a single critical point affects other joints through the Jacobian matrix. This leads us to calculate the Force-torque transformation in order to extraxt repulsive torques the joint level.

3.3.3 Force-torque transformation

We pass the repulsion force of a single critical point to other joints through the Jacobian matrix at that critical point. Then adding all effects on the joints (Eq 3.13), we get what we call virtual repulsive torque generated from the obstacle and affecting the robot joints using the formula of Park et al. (2020b) after modifying it to suite our study. This transformation is inspired from the *Jacobian-transpose Control (JT)* (Leeper, Hsiao, Ciocarlie, Sucan, & Salisbury, 2013).

$$T_{rep} = \sum_{i=1}^{N} J_{cr,i}^T F_{rep,i} \quad \text{(Eq 3.14)}$$

After computing the virtual attractive and repulsive torques, we add them to get the total torque affecting the robot joints (Eq 3.14).

$$T = \alpha_{att} T_{att} + \alpha_{rep} T_{rep} \quad \text{(Eq 3.15)}$$

We propose weights $\alpha_{att}, \alpha_{rep}$ to variate the priorities between target tracking and obstacle avoidance. In case the end effector is too far from the target and there is no existence of obstacle (or the obstacle is far), the algorithm gives high values for α_{att}. At the opposite if the obstacle is too close to some points of the robot then the priority is given to avoiding the obstacle and the α_{rep} takes high values.

In order to have natural behavior for the robot when avoiding the obstacle, we need to give great priority to joints which affect directly the critical points near the obstacle so we propose to choose α_{rep} inversely proportional to the distance between critical points and obstacle. Then we use the Jacobian at those critical points to pass from this distance vector to robot joints as proposed in (Eq 3.16).

$$\alpha_{rep} = \sum_{i=1}^{N} J_{cr,i}^{T} \begin{bmatrix} \frac{1}{dx_i} & \frac{1}{dy_i} & \frac{1}{dz_i} \end{bmatrix}^{T} \qquad \text{(Eq 3.16)}$$

Here we need to prevent the distances dx_i, dy_i, dz_i from having zero values which is ensured by avoiding collision. And also, it’s ensured while performing the calculations by fixing a lower threshold for each of these values, in case of collision or computation errors.

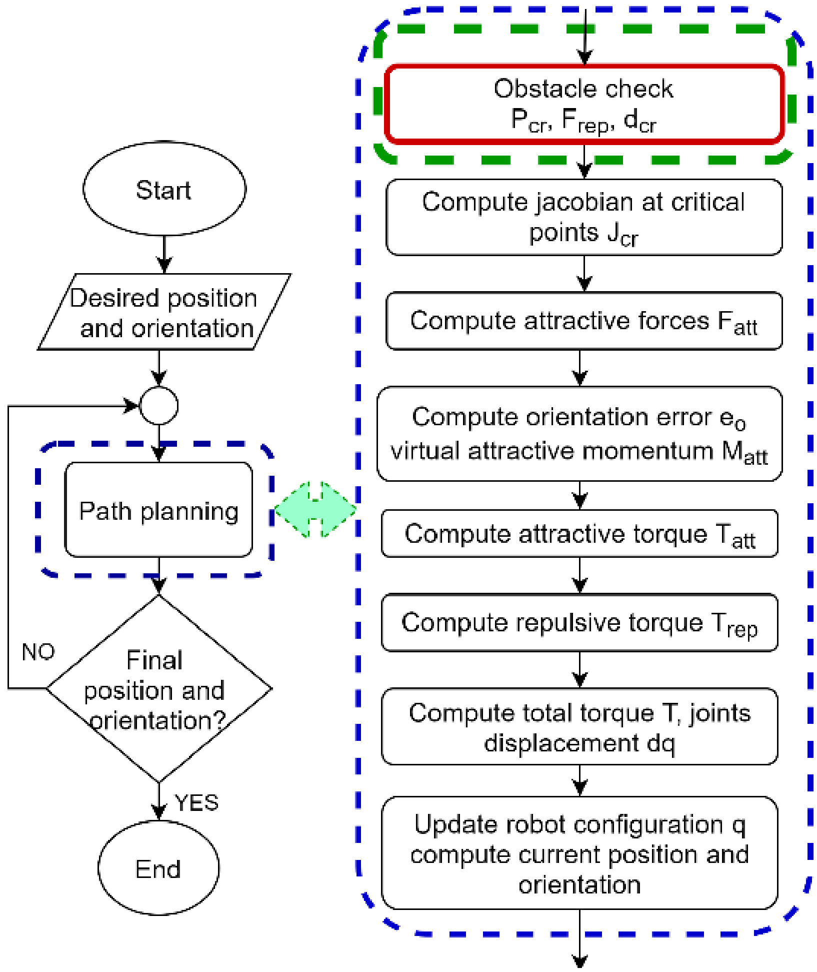

Figure 3.2: Obstacle avoidance path planning flow chart

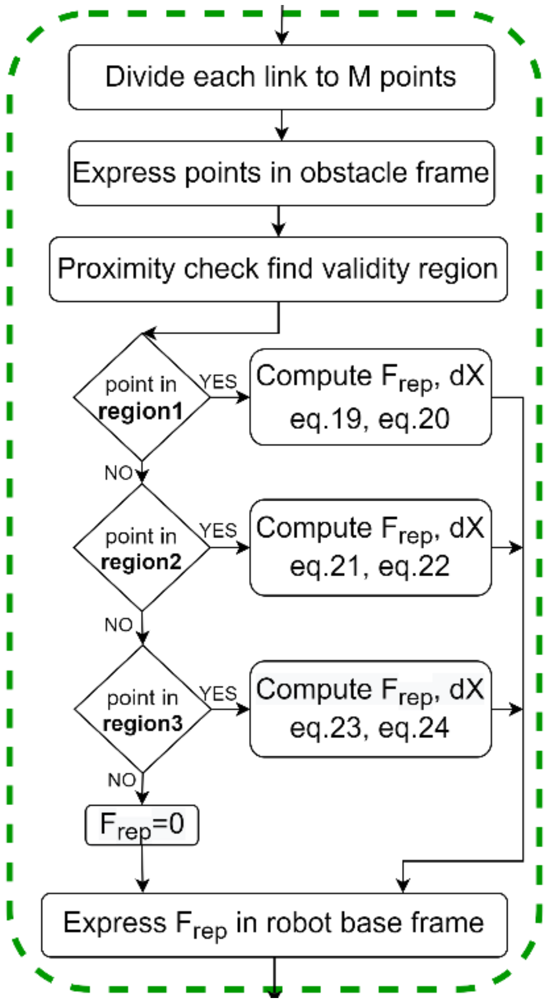

Figure 3.3: Cylindrical obstacle check flow chart

After getting the total torque value T, we compute an increment in the robot state vector q as follows (S. O. Park et al., 2020b):

$$dq = C\frac{T}{\|T\|} \qquad \text{(Eq 3.17)}$$

Where C is constant. Then we update the robot state:

$$q_{n+1} = q_n + dq \qquad \text{(Eq 3.18)}$$

Fig 3.2 describes the algorithm. In the left column, a general overview of the algorithm is presented. The right one describes in more detail the path planning algorithm. Fig 3.3 describes, also in more detail the algorithm of obstacle avoidance in case of a cylindrical obstacle.

3.3.4 General obstacle

The following figures (Fig 3.4-3.7) visualize how the robot moves from an initial pose (position and orientation) to a final one without colliding with the obstacle by the effect of attractive and repulsive forces.

Fig 3.4 shows the robot in three different states.

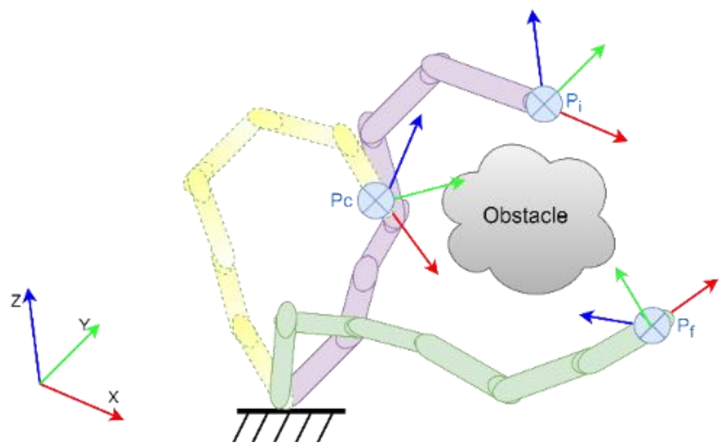

Figure 3.4: Robot manipulator motion in the presence of an obstacle
The robot is represented in the initial (purple), intermediate (yellow) and final state (green)

Fig 3.5 visualizes the different forces affecting the robot in a given state. We can notice that in this pose, the link2, link3, link4, link5, and link6 are affected by repulsive forces because they are close to the obsacle.

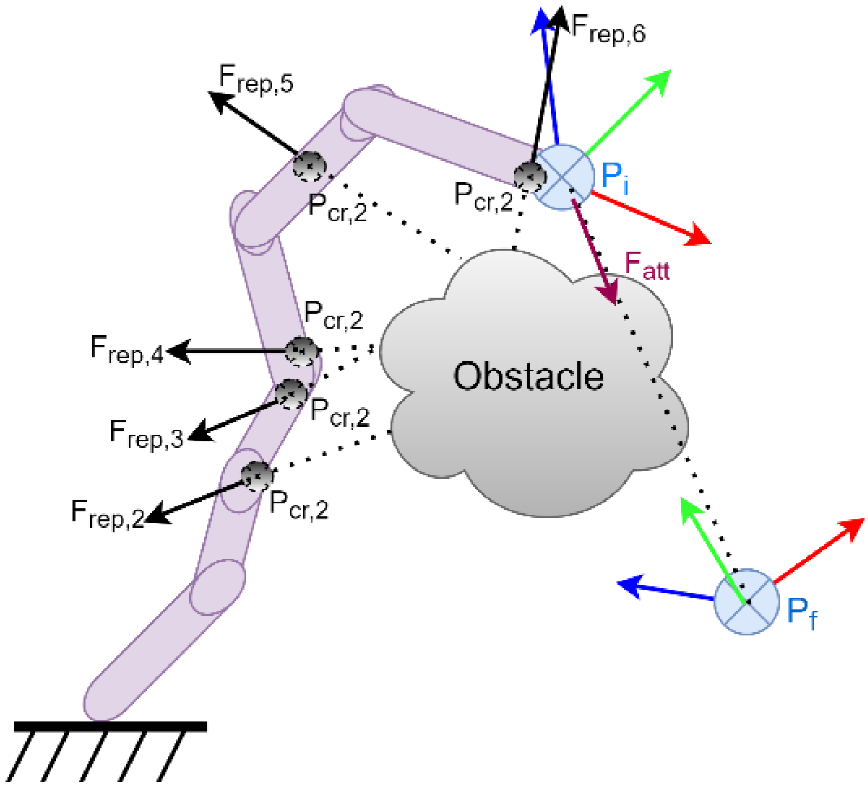

Figure 3.5: Repulsive and attractive forces affecting the robot in the initial position (link2 to link6 are in the effective field of the obstacle)

The total virtual torque led the robot to an intermediate state that makes it approaches the final target without colliding with the obstacle (Fig 3.6a).

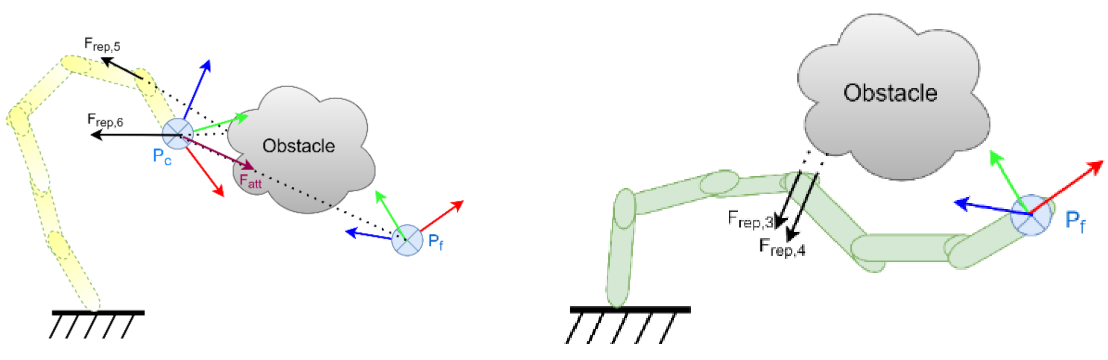

(a) (b)

Figure 3.6: (a) The robot in an intermediate position during its motion (only link5 and link6 are in the effective field of the obstacle) (b) The robot at the final position (there is no attractive force but the repulsive forces move link3 and link4 away from the obstacle)

Finally, the robot reaches the target position and orientation (Fig 3.6b). If there is still some links in the range of the obstacle, the robot still tries to change its configuration in order to cancel the repulsive forces.

3.3.5 Cylindrical obstacle model

To avoid collision with the hollow cylindrical obstacle, we need to define a potential field expression around it. We propose to benefit from the cylindrical symmetry to define the potential equation. This inspires us to divide the space near the hollow cylinder into 3 regions based on this symmetry. As we can see in Fig 3.7, which shows the robot near a cylindrical obstacle, the inside region (region 1, see Fig 3.7) has a cylindrical symetry in a way that all points that have the same distance to the z-axis should have the same potential value to mimick the physical phenomena (*E.g*. gravity or magnetisme). The repulsive force direction has to be towards the cylinder's z-axis to ensure pushing the robot critical point away from the cylinder surface.

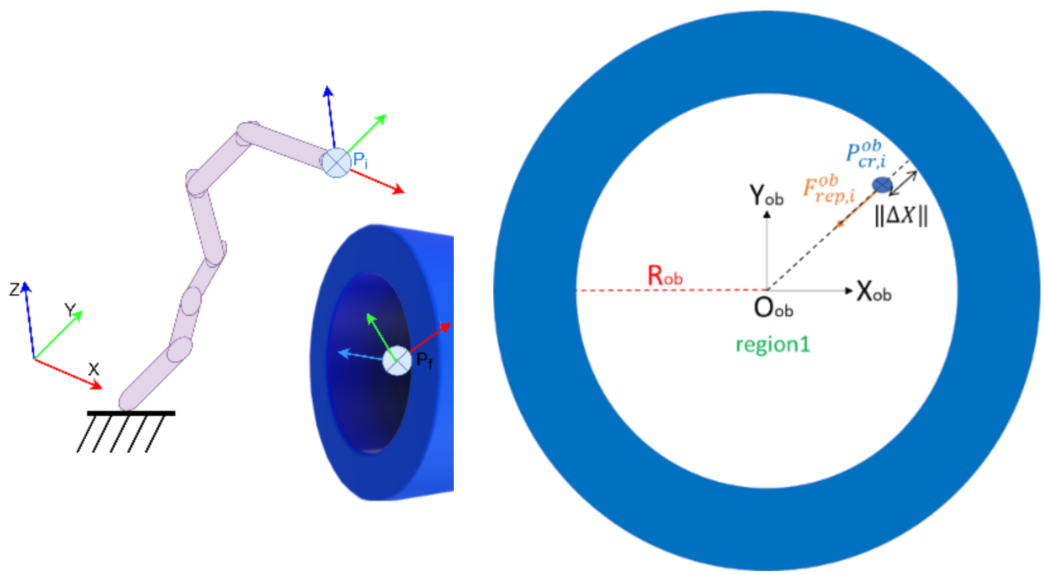

(a) (b)

Figure 3.7: (a) Manipulator motion in the presence of a hollow cylindrical obstacle (gantry) (b) Cross section for the gantry shows repulsive force elements affecting a critical point inside

Outside the gantry (the hollow cylindrical obstacle) we will not consider the side region which doesn't exist in the robot workspace. So, the rest is divided into two region (region 2 and 3, see Fig 3.8). As we can notice in Fig 3.8, the region 2 should have only plane symmetry because all the points are faced to the cylinder plane side wall. While the region 3, which exists on the extension of the interior space, should have a composed symmetry of both plane and cylindrical symmetry.

1-Region1: inside gantry (Fig 3.7 b):

$$P_{cr,i}^{ob} = T_0^{ob} P_{cr,i} = \left[X_{cr,i}^{ob} \quad Y_{cr,i}^{ob} \quad Z_{cr,i}^{ob} \right]^T \qquad \text{(Eq 3.19)}$$

$$\|\Delta X\| = R_{ob} - \sqrt{\left(X_{cr,i}^{ob}\right)^2 + \left(Y_{cr,i}^{ob}\right)^2} \qquad \text{(Eq 3.20)}$$

$$F_{rep,i}^{ob} = -k_{rep} \left[\frac{1}{R_{ob} - X_{cr,i}^{ob}} \quad \frac{1}{R_{ob} - Y_{cr,i}^{ob}} \quad 0 \right]^T \qquad \text{(Eq 3.21)}$$

2-Region2: outside the gantry, outside the extension (Fig 3.8)

$$F_{rep,i}^{ob} = -k_{rep} \left[0 \quad 0 \quad \frac{1}{-Z_{cr,i}^{ob}} \right]^T \qquad \text{(Eq 3.22)}$$

$$\|\Delta X\| = Z_{cr,i}^{ob} \qquad \text{(Eq 3.23)}$$

3-Region3: outside the gantry, inside the extension (Fig 3.8)

$$\|\Delta X\| = \sqrt{\left(R_{ob} - \sqrt{\left(X_{cr,i}^{ob}\right)^2 + \left(Y_{cr,i}^{ob}\right)^2} \right)^2 + \left(Z_{cr,i}^{ob}\right)^2} \qquad \text{(Eq 3.24)}$$

$$F_{rep,i}^{ob} = -k_{rep} \left[\frac{1}{R_{ob} - X_{cr,i}^{ob}} \quad \frac{1}{R_{ob} - Y_{cr,i}^{ob}} \quad \frac{1}{-Z_{cr,i}^{ob}} \right]^T \qquad \text{(Eq 3.25)}$$

$$F_{rep,i} = \left(T_0^{ob}\right)^{-1} F_{rep,i}^{ob} \qquad \text{(Eq 3.26)}$$

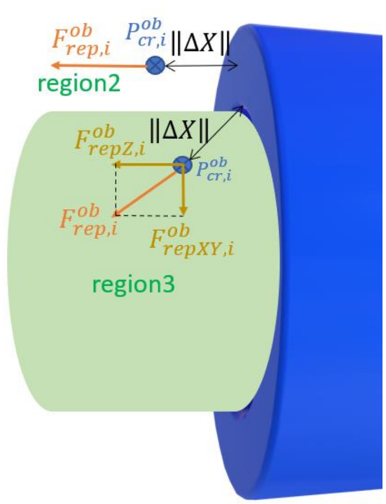

Figure 3.8: Repulsive forces elements affecting critical points outside the gantry in two cases (inside and outside the green extension)

3.4 Simulation results

Measuring the viability of a real-time collision-free path planning is very complicated, due to the difficult algorithm effectiveness validation in reason of the large number of tests that needed to be done. In addition, when avoiding obstacles in real-time, the manipulator could endure some damages if a collision is unavoidable. Therefore, a simulation platform for the purpose of the whole-arm obstacle avoidance path planning of the arm in the obstacle space was established in respond for the above problematics. The simulation platform uses MATLAB R2020b in conjunction with Robotics Toolbox.

We created the robot model starting from the parameters given in Table 3.1. Then, we performed all necessary functions to compute the direct kinematic, jacobian matrices, collision detection and path planning as mentioned in the previous sections. Inverse kinematic is not needed in the algorithm. But, it was used in the initialization in some tests. For this reason, it was computed using the inverse kinematic solver which is included in MATLAB Robotics Toolbox when it was needed.

To do the visualizations, we used the interactive rigid body tree which provides both: an easy way to change the robot configuration on the figure, and an easy way to add obstacles to the environment. *UR5* robot 3D model contained in MATLAB libraries was used. In order to enable the robot to overcome the obstacle while moving towords the desired position and orientation, our proposed algorithm adds the effects of all the attractive/repulsive forces affecting the robot links as a total torque.

The simulation experiments were separated into two parts: firstly, the avoidance of a spherical obstacle, and secondly, the avoidance of a hollow cylindrical obstacle.

3.4.1 Spherical obstacle avoidance

Table 3.2 contains the details of this first experiment.

Fig 3.9 shows the simulation results of a spherical shaped obstacle avoidance. The blue point Pi, the red point P_f and the black points denote the robot initial, final and planned positions, respectivley. The orientaion of the robot was represented using frames (shown in RGB color base). We can see from these results how the robot successfully avoided the collision with the obstacle and reached the final position and orientation.

Fig 3.10 shows the robot joint angles. As this figure shows, the algorithm generated a smooth path in the configuration space.

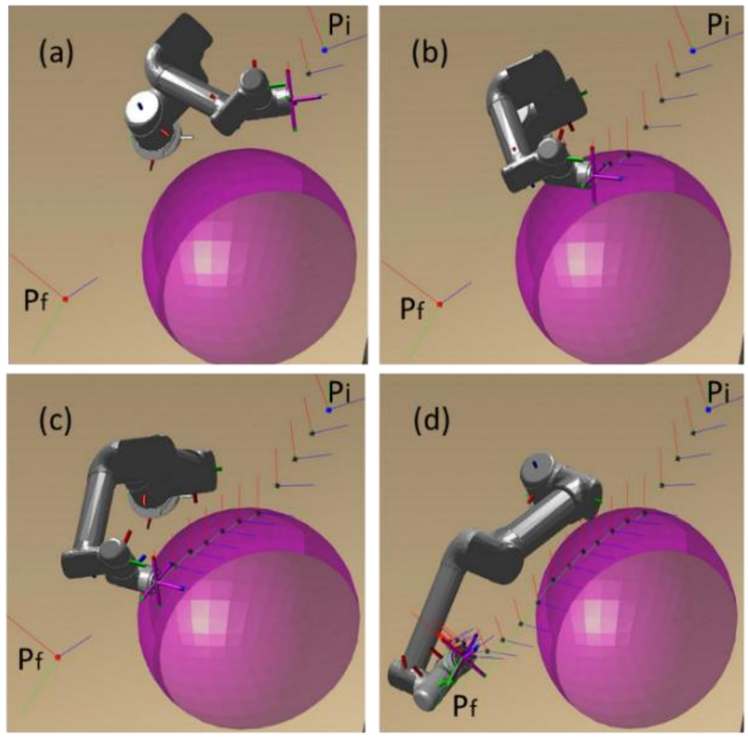

Figure 3.9: The robot avoids colliding with a spherical obstacle
(a) the robot follows the path toward the final target before reaching the obstacle repulsive field (b) the robot reaches the obstacle repulsive field and modifies its path (c) the robot begins to get out of the repulsive filed of the obstacle (d) the robot reaches the desired position and orientation

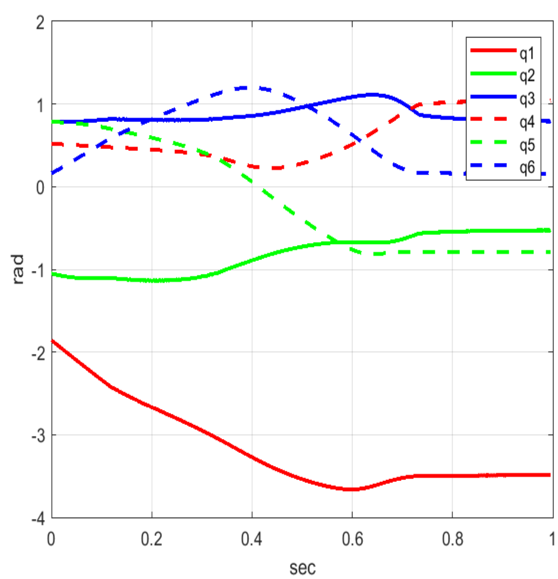

Figure 3.10: Joint trajectories in spherical obstacle avoidance

Table 3.2: Details of spherical obstacle avoidance experiment

Shape of obstacle	sphere
Coordinates of obstacle (m)	(0.45, 0.4, 0.1)
Radius of obstacle (m)	0.3
Starting position (m)	(0.01, 0.65, 0.45)
Starting orientation (rad)	(-2.68, -0.34, 1.77)
Starting joint angles (rad)	(-π/1.7, -π/3, π/4, π/6, π/4, π/20)
Desired position (m)	(0.66, -0.06, 0.23)
Desired orientation (rad)	(-1.96,-0.8,0.21)
Desired joint angles (rad)	(-π/0.9, -π/6, π/4, π/3, -π/4, π/20)
Calculation time (sec)	0.001

3.4.2 Hollow cylindrical obstacle (Gantry) avoidance

Table 3.3 contains the details of this second experiment. Simulation results of the avoidance of a cylindrical shaped obstacle, a gantry-like, are shown in Fig 3.11. The blue point, the red point and the black points denote the robot initial, final and planned positions, respectivley. The orientaion of the robot was represented using frames (shown in RGB color base). We can see from these results how the robot successfully avoided the collision with the borders of the the gantry and reached the final position and orientation inside the gantry. In Fig 3.12, it is shown the front view of the environment (Y axis). We can notice from both Fig 3.11 and Fig 3.12 that the path planned in the robot's operational space, besides safely avoiding the collision with the gantry borders, it was smooth.

Fig 3.13 shows the robot joint angles. As we can see from this figure, the algorithm generated a smooth path in the configuration space.

Table 3.3: Details of cylindrical obstacle avoidance experiment

Shape of obstacle	Hollow cylinder
Coordinates of obstacle (m)	(0.65, 0.6, 0.2)
Internal radius of obstacle (m)	0.5
Starting position (m)	(0.024, 0.095, 0.9)
Starting orientation (rad)	(0 , -π/2, 2.62)
Starting joint angles (rad)	(4π/3,-π/2,0,0,π, 0)
Desired position (m)	(0.65, 0.44, 0.09)
Desired orientation (rad)	(1.09, -0.37, 1.96)
Desired joint angles (rad)	(7π/6, -π/8, π/6, π/8, 3π /4, π/4)
Calculation time (sec)	0.0013

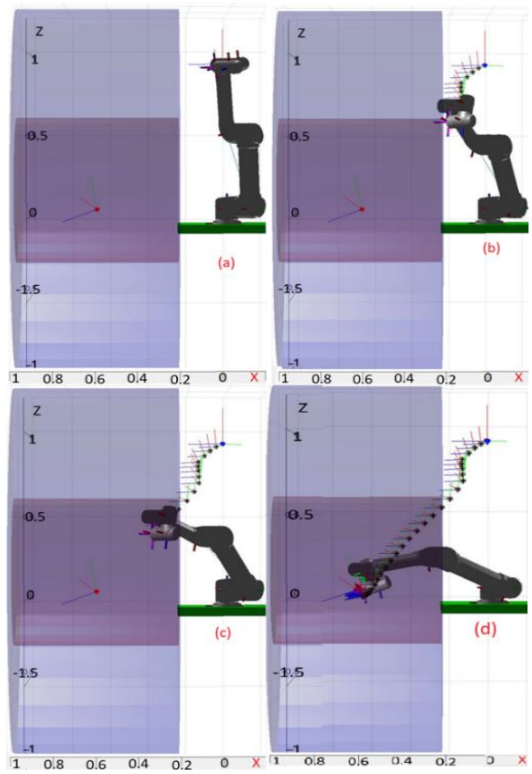

Figure 3.11: The robot moves inside the gantry and avoids colliding with it
(a) the robot at the initial pos before reaching the obstacle repulsive field; (b) the robot reaches the obstacle repulsive field and modifies its path; (c) the robot begins to get out of the obstacle's repulsive filed; (d) the robot reaches the desired position and orientation

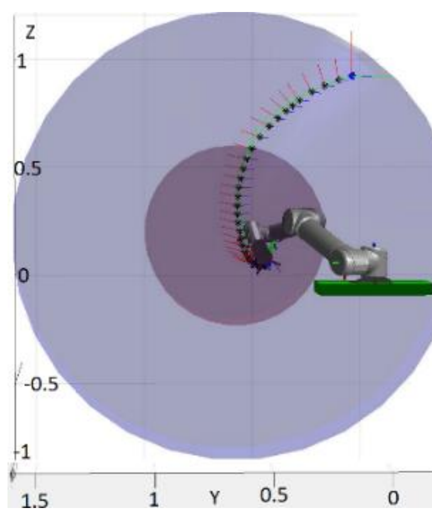

Figure 3.12: Front view for the robot moving inside the gantry without collision with its borders

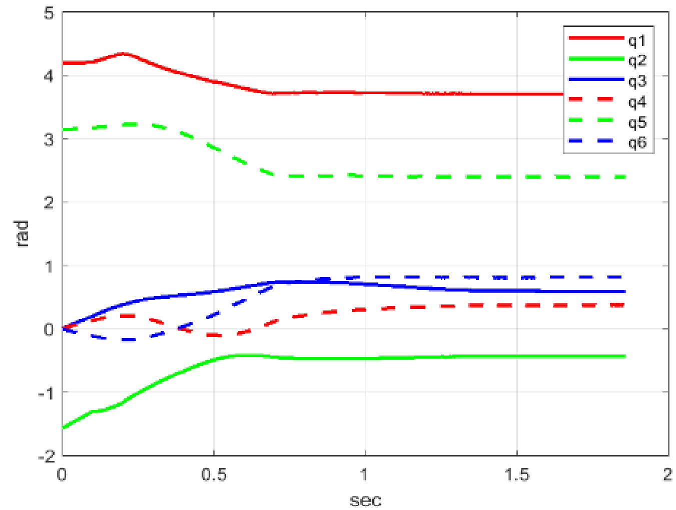

Figure 3.13: The joint trajectories (cylindrical obstacle)

Fig 3.11 shows that the distance between the end effector point and the obstacle border is about 0.1 m which is the same as the marginal distance used in the algorithm. However, it is not always the case, because the robot links have different values for radius when they are modeled as poly-articulated cylinders. In order to ensure the safety, the maximum value for the radius of these links has to be used as a marginal distance in the algorithm, although it loses manipulability in regions close to the obstacle. It is worth discussing that by properly tuning the constant C in (Eq 3.17), a good compromise can be made between vibration and speed. We noticed that high values for C lead to high displacement in configuration space, hence a big vibration. While at the opposite, when minimizing its value, we can get a more continuous and smooth path.

Experiments on different initial robot's configuration

The proposed algorithm will be used in general as part of a higher level control system that supplies initial and final poses to plan a free-collision path between them. In order to perform the APF algorithm, we need to find the initial configuration q_i for the robot's initial pose P_i. A general 6R serial robot manipulator has 16 solutions for the inverse kinematic (IK). However, robots with the *UR5* geometry only have 8 solutions, at most, (Villalobos, Sanchez, & Martell, 2022). Hence, the robot can have 8 different initial configurations even for the same pose. Because there are no constraints that limit this number of soltions, we need to evaluate the effect of changing those initial configurations on the algorithm behaviour.

So we performed some experiments to test the algorithm behaviour when another solutions for the inverse kinematic are supplied. To do this, we generated all the possible solutions of the inverse kinematic at the initial pose (using the Inverse Kinematic Solver in Robotics Toolbox). Then, we executed the algorithm for each one of these solutions.

Experiment 1: for the pose given in Table 3.3, we got multiple solutions for the inverse kinematic because it is a singular pose, some of them were repeated. We performed the experiment on the 7 solutions shown in Table 3.4 (it shows that 2 solutions are repeated).

It appeared that the algorithm was able to succeed in generating a collision-free path for 3 different of those solutions, and failed in the rest 2 cases. The failure of the algorithm was due to the appearance of local minima on the robot's path. However, it was still successful to avoid the collision despite slower motion in some places near the obstacle. We assume this is due to the proximity of local minima, which approximately cancels the total torque affecting robot joints. Paragraph 3.4.3 below deals with this recurring issue of local minima.

Fig 3.14 shows the robot successfully reachs the desired target with no collision (Test1 to Test5). Fig 3.15 shows joint angle q4 in successful tests (Test1 to Test5). We can see that the maximum change in angle value among these tests is 0.25 rad.

After some processing on the configurations, by wrapping all articular angles to the inerval [-π, π] and then deleting the repeated solutions, we found that we have only 5 different configurations. It is noticed that configurations $q_{0,2}$, $q_{0,3}$ express the same solution. The same case for the configurations $q_{0,4}$, $q_{0,5}$ as shown in Table 3.4.

Table 3.4: Obstacle avoidance results for different initial robot configurations $q_{0,i}$ (rd)

Test1	$q_{0,1}$	(-2.π/3, - π/2, 0, 0, -π, 0)	successful
Test2	$q_{0,2}$	(-2.π/3, -1.34, -0.47, 0, -π, -0.24)	successful
Test3	$q_{0,3}$	(-2.π/3, -1.34, -0.47, 0, π, -0.24)	successful
Test4	$q_{0,4}$	(-2.π/3, -1.47, -0.21, 0.06, π, -0.05)	successful
Test5	$q_{0,5}$	(-2.π/3, -1.46, -0.22, 0.06, -π, -0.05)	successful
Test6	$q_{0,6}$	(-2.π/3, -1.66, 0.63, -π, π, -2.46)	unsuccessful
Test7	$q_{0,7}$	(2.76, -1.25, -0.94, -0.95, -1.71, -π/2)	unsuccessful

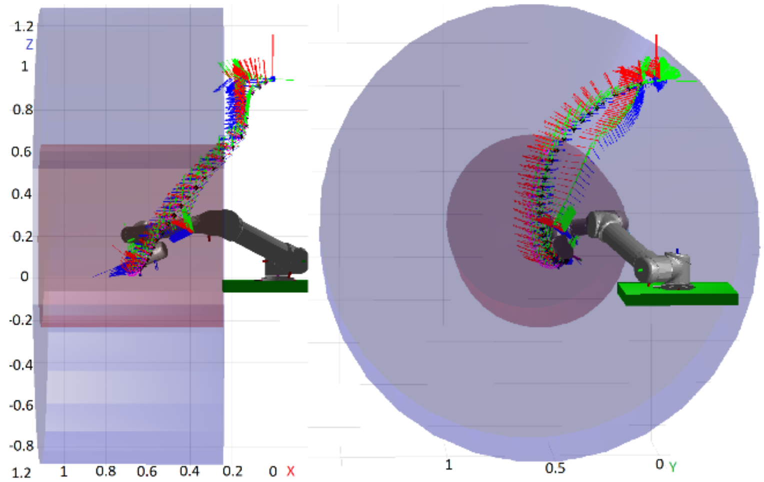

Figure 3.14: The path generated in all successful configurations

Experiment 2: we tried a very small modification in position to do the test beginning from a nonsingular configuration, we had three different solutions for the IK. The algorithm succeeded in one of them and failed in the two other ones due to a local minima phenomenous but still was successful to avoid collision wth gantry borders.

Experiment 3: we tried another position outside the gantry so that we find the reason for failure. The IK for the new initial position and orientation gave 8 different solutions (so, the max of the UR IK). The algorithm faild in 4 configurations (fell in local minima).

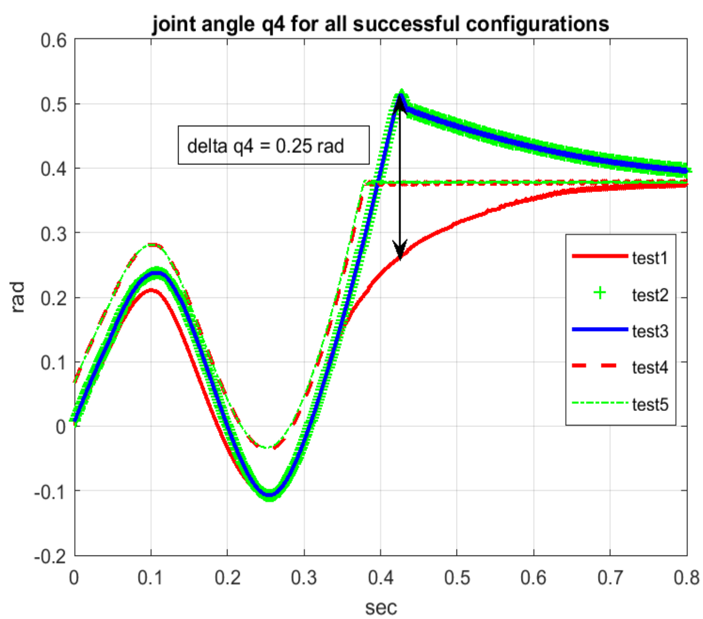

Figure 3.15: Trajectories for joint angle q_4 in all successful configurations

Experiment 4: we tried another initial position and another initial orientation inside the gantry (position and configuration close to the final target). We got the same results above. The algorithm succeeded in 4 configurations and failed in the other 4 ones. These results present that local minima are unavoidable in this kind of applications.

Experiment 5: we tried some other tests to test whether the local minima depends on the orientation or not. Based on these tests, we found no relation while we expected the opposite. The robot orientation affects the attractive forces which in its turn can affects the balance with repulsive forces (local minima) as the furmla proposes. However, we could not perform enough experiments to decide precisely on such relation.

3.4.3 Local minima

Multiple techniques were intruduced to detect and escape local minima in literature since the early use of APF. Local minima occur when total torque (Eq 3.15) is so small to generate a change in the robot configuration or it is vibrating while not reaching the goal point yet. It was detected by measuring the standard deviation of the robot joint angles over a horizon. If it is smaller than some predefined threshold before finishing the task, then the robot is trapped in local minimum region. In (Xiaoping Yun & Ko-Cheng Tan, 1997) a wall-following method was introduced in order for the mobile robot to escape the local minima by following the direction of the obstacle’s wall. One of the famous techniques to escape this region was to assign a virtual goal or obstacle to change the balance between repulsion and attraction that occurs in local minima regions. In (Safadi, 2007), a virtual force in the direction of no obstacle has been assigned to the original forces (repulsive and attractive ones).

In our algorithm, we used a similar technique that assigns a force affecting the robot’s end-effector. This virtual third force is perpendicular to the attractive force precomputed in (Eq 3.9). Then, the virtual torque resulting from this force is added to (Eq 3.15). Most of the local minima have been resolved using this techniques, Fig 3.16 shows an example of the resolved situations. However, there are still some cases, that they need to be resolved, in which, local minima appear at the goal point’s proximity.

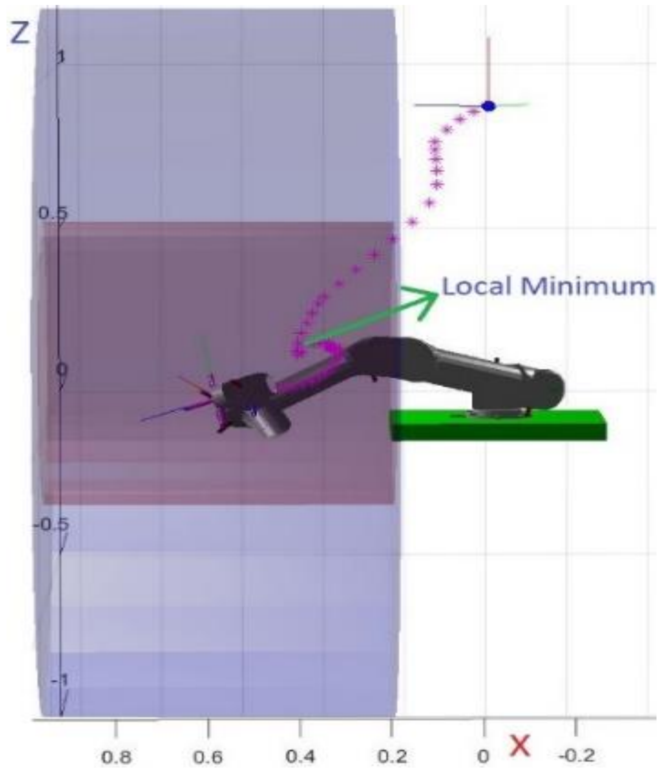

Figure 3.16: The path with processing local minimum

In summary, the simulation setup included creating a *UR5* robot model using MATLAB and Robotics Toolbox, and experiments on avoiding both spherical and hollow cylindrical obstacles. Simulation results validate the proposed APF algorithm, and the results showed successful obstacle avoidance in the majority of situations. However, there has been some failure in others which need to be improved.

The proposed algorithm was implemented on a *UR3e* robot to be evaluated in the teleoperation main task context. The results are shown in chapter 5 in parallel with teleoperation experiments.

After showing that the proposed algorithm was able in planning collision-free paths, it is suitable for the application of manipulation inside a hollow cylinder especially in case of small variations of the desired tool position and orientation. And it is successful in local planning as a part of global path planning task and for avoiding obstacle in case of teleoperation. The average time needed for doing all the calculations in order to get the next robot configuration, was about 1ms in case of the spherical obstacle and 1.3ms in case of the hollow cylindrical one. These results indicates that the proposed algorithm can be integrated in a whole control system for the task of manipulation in real-time application.

Due to the model of poly-articulated cylinders which was used for the manipulator during the collision avoidance, only small margins around obstacles can be used to ensure the collision-free paths. These margins depend on the maximal value of the robot links radius. The results also show that the proposed algorithm works in different cases with a variety of collision types by defining a suitable repulsive force function for each type of obstacles.

Limitations due to local minima were processed and resolved in most of the cases. However, they are still faced in some cases when the end effector reaches near the final pose, but we believe that teleoperation, as long as there's a human in the loop, will contribute to solve these situations.

Performing tele-echography in the cPETRUS context, in which there is a patient and sometimes a radiologist near the robot, makes it necessary to generalize the obstacle avoidance method to be able to process human-like obstacles. In the next chapter, we will present a general perceptual framework to the human-like obstacle avoidance based on the Artificial Potential Field. The evaluation of the algorithm integrated with teleoperation task will be presented in chapter 5.

CHAPTER 4
Generalization of APF obstacle avoidance algorithm for human-like obstacles

We have seen in the previous chapter the design of APF-based collision-free motion planning for the whole body of the robot manipulator. The obstacles we've discussed had spherical and hollow cylindrical shapes. However, in human-robot interaction domain, like our application presented in chapter 1, we need to discuss the human body as an obstacle. In this chapter, we will study this case in APF-based motion planner by introducing a general conceptual framework for collision avoidance between the human body and the entire robot manipulator using the earlier proposed APF method.

4.1 Human body collision model

When implementing human body obstacle avoidance in the context of motion planning for a robot using APF, there are several specific considerations and techniques to increase the effectiveness and safety of the system. Here are some additional contributions and strategies

4.1.1 Human collision modelling: challenges and solutions

Choosing a suitable human collision model, when implementing human body collision-free motion planning, is important for safe and successful path planning.

The human body characteristics add some extra aspects and considerations of which we need to take care comparing to non-human obstacles. Here we introduce some of these considerations:

1) The human body can be modelled as articulated links, like a poly-articulated robot manipulator. Each link corresponds to a part of the body. Although this approach provides a detailed representation of the human body, it can be difficult to integrate into a motion planning algorithm, especially when the human is dynamic.
2) The human body can have a variable size and shape that differs from person to person. This makes it complicated to develop a generic obstacle avoidance technique that can adapt to individual differences among humans who might possibly interact with the robot. In addition, humans have soft tissues and clothing that may need to be considered when designing a collision model. However, this is more relevant to very close physical interaction (*E.g.* physical contact) where compliance control is considered rather than obstacle avoidance planning.

It's very often to consider the human body as a point, or to consider only the nearest point of the human body. The obstacle avoidance model uses the distance between the point of concern in the human and the end-effector point on the robot (Farsoni, Rizzi, Ufondu, &

Bonfè, 2022). As a result, the collision model should prevent this distance from being less than threshold (Fig 4.1a). Although it might be successful in some applications that doesn't require intersection between the human parts and the robot parts. There has been some enhancements on this collision model by taking the human length into consideration (Safeea & Neto, 2018). So, the robot has to avoid collision with a cylinder around the human body (Fig 4.1b).

However, this enhancement doesn't take into consideration the size difference between body parts. In order to ensure safety for the human hands, we need to increase the cylinder diameter which undesirably decreases the robot workspace around some other body parts. The obstacle avoidance can be improved using the capsule model presented in (Safeea, Neto, & Bearee, 2019) as shown in Fig 4.2. This collision model protects all the human body parts, while preserving the robot workspace.

In (Bharatheesha et al., 2017), the authors used an artificial skin on the *UR5* robot manipulator which allowed for safe collisions with humans within a work cell (Fig 4.3). A 3D point cloud was generated, and collisions were detected using the *KineoTMCollision* Detector (KCD). This system provided precise proximity information, similar to tactile sensing. However, this approach had some limitations, including the limited effectiveness of proximity sensors at relatively far distances limiting the obstacle avoidance efficiency in various situations.

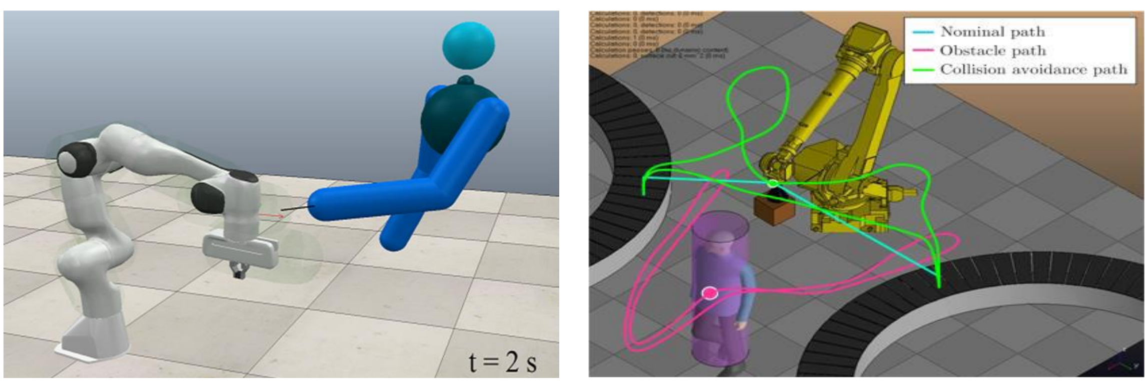

(a) (b)

Figure 4.1: (a) The human forearm bone exceeds the minimum distance threshold so that the robot follows the repulsive potential fields to avoid collisions (Farsoni et al., 2022)
(b) one-cylinder human collision model (Safeea & Neto, 2018)

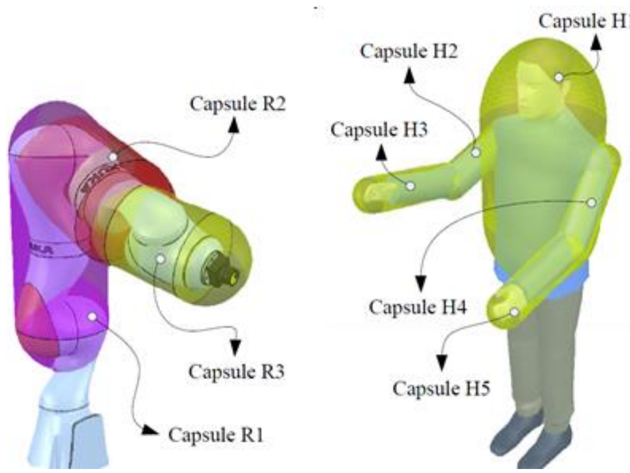

Figure 4.2: The robot and the human represented by capsules or multi-parts (Safeea, Neto, & Bearee, 2019)

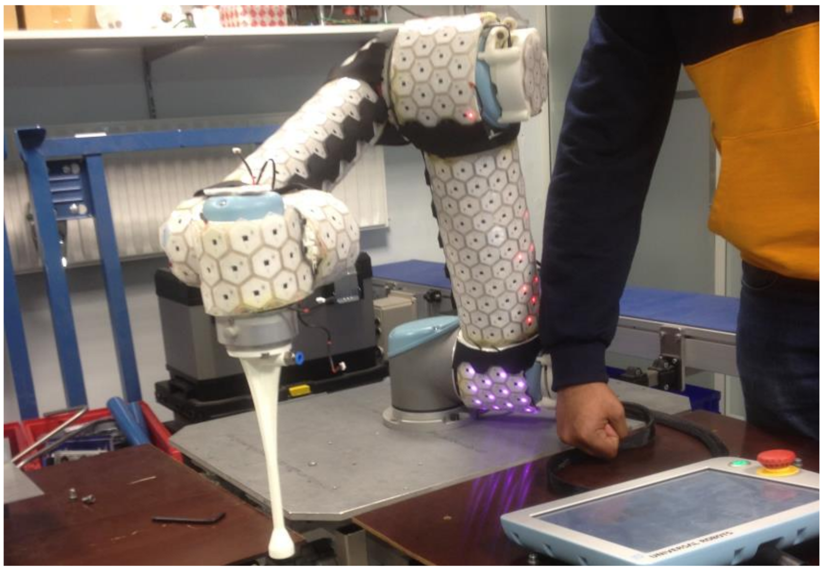

Figure 4.3: *UR5* setup with the Artificial Robot Skin (Bharatheesha et al., 2017) showing some cells being activated (with red LEDs) by obstacles (<= 6 cm)

In (Dietrich, Wimbock, & Albu-Schaffer, 2011), the authors explored collision avoidance with the DLR's humanoid robot Justin. The study introduced a comprehensive collision avoidance system involving time-of-flight cameras to generate repulsive potential fields around the mobile base and upper body self-collision avoidance using a potential field-based approach. This approach profits from redundancy and null space to manage various tasks, such as self-collision avoidance and mobile base avoidance. While promising to highlight the robot's adaptability in dynamic environments, the method requires redundant mechanisms to manage obstacle avoidance with main tasks.

The same team (Dietrich, Wimbock, Taubig, Albu-Schaffer, & Hirzinger, 2011) used self-collision avoidance techniques for the humanoid robot. The method identifies and prevents collisions by finding pairs of links with the smallest distances. Through the calculated distance and the critical points and using a parabolic model (see Fig 4.4), repulsive forces were generated and used in the admittance controller to ensure compliance without collision. Experimental results confirmed effective self-collision avoidance in low computational time, making it faster than other approaches such as grid-based ones.

Figure 4.4: Self-collision avoidance model of DLR's humanoid Justin consisting of 28 convex hulls (left arm: 8, right arm: 8, mobile platform: 5, torso: 4, head: 2, floor: 1) (Dietrich, Wimbock, Taubig, et al., 2011)

In (Hong Liu, Xuezhi Deng, & Hongbin Zha, 2005), authors proposed a solution to the computational challenge of determining obstacle positions in real-time depending on the construction of a dynamic roadmap and using sampled surface points to represent moving obstacles (Fig 4.5). The continuity of obstacles' surfaces, allowed for a significant reduction in the number of sampled points required. This enables the roadmap to be updated in real-time, which in turn facilitates collision avoidance. This offers several advantages, including adaptability to dynamic environments and the ability to maintain a safe distance between robots and moving obstacles. However, it's important to note that the reliance on sampled surface points may have limitations in highly complex or irregular obstacle geometries.

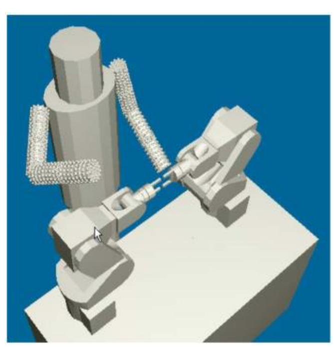

Figure 4.5: Sampled surface points and the goal configuration (Hong Liu et al., 2005)

An obstacle model is built on depth space data to compute the distances between the robot and dynamic obstacles including people in (Flacco et al., 2012). Obstacle detection relies on depth-sensing technology, such as the *Microsoft Kinect* sensor (Fig 4.6). Repulsive vectors, which can adjust to obstacle velocities are used to control multiple points along the robot's structure which ensures the whole robot body obstacle avoidance. However, it requires depth sensors and faces potential restrictions in extremely dynamic environments.

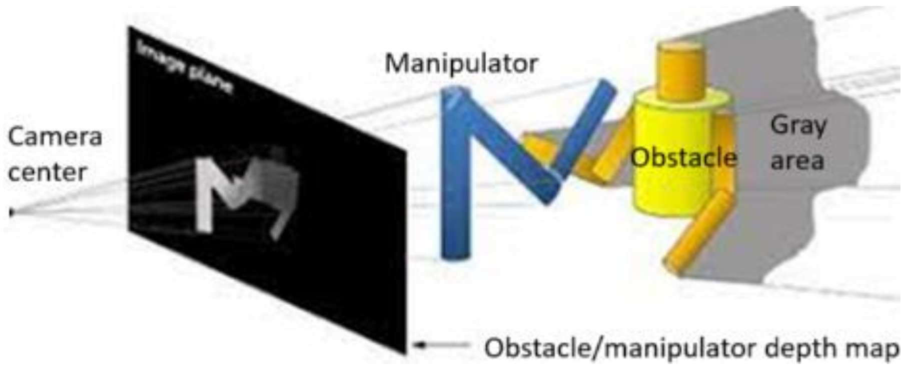

Figure 4.6: Generation of a depth image, with lighter intensities representing closer objects Points occluded by the obstacle compose the grey area (Flacco et al., 2012)

(a) (b)

Figure 4.7: (a) The human is trying to touch the robot causing the robot to maneuver in a collision avoidance motion (Safeea, Neto, & Béarée, 2019) (b) Human body pose recognition from a single-view depth camera (Huang & Jeng, 2012)

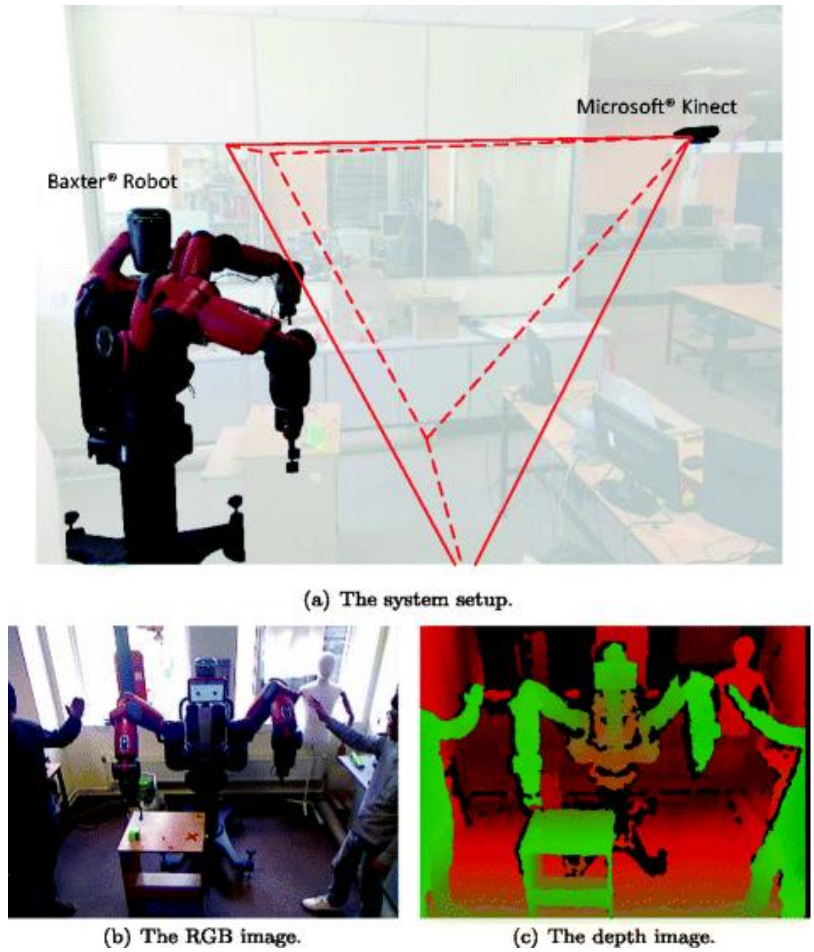

Figure 4.8: Robot manipulator self-identification for surrounding obstacle detection
The (a) system setup (b) RGB image (c) depth image (X. Wang, Yang, Ju, Ma, & Fu, 2017)

The obstacle model employed in (Sugiura, Gienger, Janssen, & Goerick, 2007), simplifies the humanoid robot model into primitive objects (spheres or swept sphere lines see Fig 4.9), enabling faster computation of distances and closest points. The method uses virtual forces and null-space optimization to ensure collision-free planning. The system improved safety in real-time tasks and allowed continuous motion. However, it encounters difficulties related to local minima, motion irregularities, and computing complexity. The collision model is similar to earlier works that have been investigated but does not take avoidance with other objects into consideration.

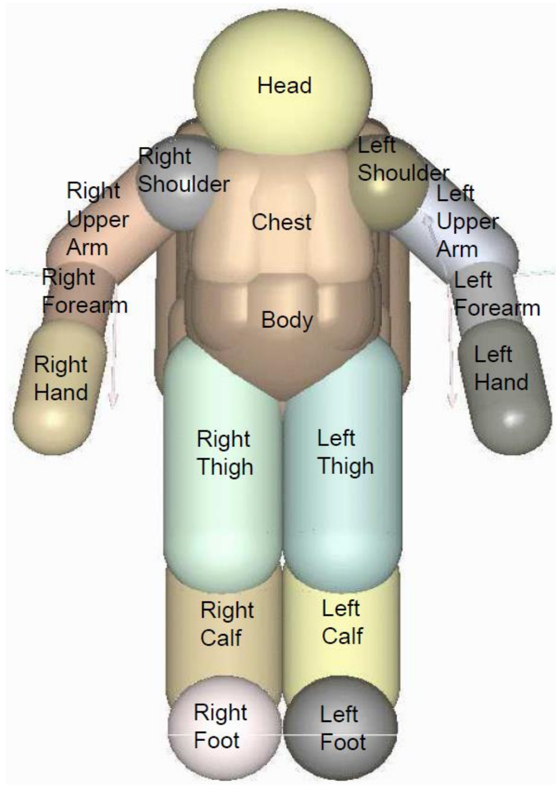

Figure 4.9: The human collision model is composed of 17 segments
Each segment is composed of one or several sphere-swept-lines or spheres (Sugiura et al., 2007)

In (C. Park, 2015), the author introduces the development of a self-collision avoidance algorithm for a dual-arm robot manipulator (6 *DoF* per arm and 2 *DoF* for the torso), which was developed for assembly tasks. There is a possibility of self-collision (collision between the robot's arms and torso). Predicting self-collision with an exact robot model can be computationally intensive. To reduce computing time, virtual links and spheres are used to approximate the robot's shape and detect potential collisions to prevent the robot's limbs from colliding with each other. The algorithm checks the distance between virtual spheres representing different parts of the robot (Fig 4.10). If the distance is less than the sum of the radii of the spheres, a self-collision is predicted. The radius of the virtual sphere can be adjusted to provide flexibility based on the specific task and operating conditions. The algorithm's low computational requirements make it suitable for real-time implementation in the robot's controller. It can adjust the robot's motion to avoid self-collision or slow down if a potential collision is detected.

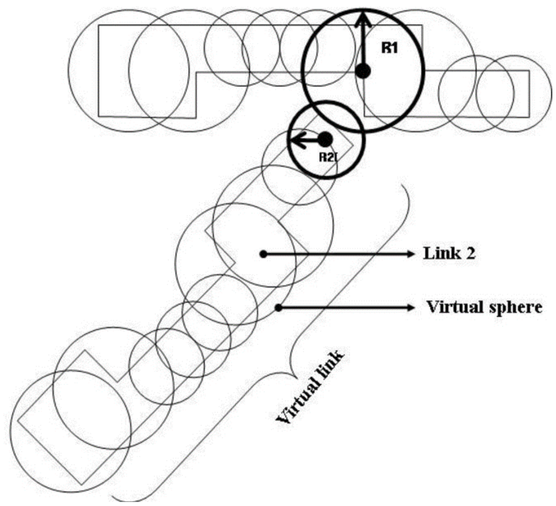

Figure 4.10: Calculation method of the collision of the virtual spheres (C. Park, 2015)

Based on the presented state-of-the-art and to reply to the issues mentioned at the beginning of this chapter, here is a discussion of the potential considerations to be taken into account when designing a collision-free path planner that involves:

1) Integrating proper perception sensor data, such as vision or depth sensors, to continually update the collision model based on the real-time position, shape, and movement of the human can create a realistic representation of the human's shape with the use of 3D point clouds. These realistic models can be enhanced by using multiple sensors to capture different aspects of human motion. This point cloud can serve as the basis for calculating a virtual repulsive force generated by each point within the cloud. These repulsive forces collectively contribute to the computation of a potential field around the human body to be used in obstacle avoidance. The distance between the 3D point cloud and the robot is either to consider the closest point, all the points, or only the surface points within the cloud. Depending on only the closest point is not practical if it is necessary for the robot to approach the human because it does not take into consideration the human shape and turns the collision model to simple point avoidance. Generating the surface shape of a point cloud is an interesting challenge and it can be beneficial to generate a more practical potential field around the human in collision avoidance tasks. However, demands the construction of a point cloud for the human body each time instant then finding a way to find out the surface points then computing the total effect (repulsive forces) of each point of this cloud on the robot test point, which requires a high computation power. The construction of a point cloud although it seems a more exact model of the human body, it is still not so much exact practically due to the distortion resulting from the difficulty of segmentation and the discrimination of the human from the other objects around him. This justifies the unpromising expectation when using such models.

2) Using anthropometric data to roughly determine the dimensions and proportions of the collision model. However, variations in body sizes and shapes need to be taken into account in order to create a collision model that applies to a diverse range of individuals and can be solved by user-defined parameters. This is performed by enabling users to define or customize some parameters of the model based on the specific requirements of the application. This flexibility allows the collision avoidance behaviour to be fine-tuned.
3) Considering joint constraints to accurately model the range of motion for each body part. This ensures that the collision model respects anatomical constraints and prevents unrealistic intersections between body segments.
4) Defining variable attraction regions around the human body. Different body parts might have different levels of sensitivity to robot proximity. This also can depend on the application. *E.g.* during the echography for the torso, the head might have a larger repulsion zone than the arms.
5) Implementing different human-robot collaboration modes to allow for variations in human-robot interaction. For instance, the robot might switch between modes for close collaboration, maintaining a safe distance, or temporarily stopping when the human is in proximity. And also allowing for human intervention and control in (human-in-the-loop) situations where the robot encounters difficulties in navigating around the human body.
6) Integrating the sense of approaching obstacles in haptic feedback in applications that contain teleoperation tasks can allow the human operator to intervene by modifying the robot's path in real-time to respond to sudden changes in the environment.
7) Incorporating learning-based approaches like Deep Reinforcement Learning (DRL) techniques introduced in (Sangiovanni, Rendiniello, Incremona, Ferrara, & Piastra, 2018). Unlike the previously investigated collision avoidance approaches, the proposed one is a model-free approach which facilitates the implementation phase. To the best of the authors' knowledge, the proposed approach is one of the first examples of applying DRL techniques to robot manipulators for collision avoidance. However, it has been applied in a virtual scenario. Such techniques use machine learning techniques to improve the adaptability of the motion planner and can be employed to learn from human-robot interactions and optimize the planner's parameters over time. However, most often, their spaces of output action are discrete, making them difficult to apply to continuous action spaces such as the trajectory planning for robot manipulators. In addition to that, due to the randomness and blindness of these techniques, they can lead to a large number of useless explorations which decreases the algorithm efficiency (Peng, Yang, Li, & Khyam, 2023).
8) Evaluating the collision model through user studies to collect feedback on the collision avoidance behaviour to refine and improve the model.

4.1.2 Intermediate human collision model

An alternative approach is to simplify the representation of the human body as a cylinder (Fig 4.11a). To apply this approach, we need to determine the position and orientation of the cylinder at each moment. It's also important to assume that we do not need to access any point inside the cylinder. Furthermore, the dimensions of the cylinder should be chosen to be larger than the actual human body for complete obstacle avoidance which is a limitation in our case (as for echography, the tool must be in contact with the patient). Ultrasound requires access to certain parts of the human body that the cylindrical model may not allow.

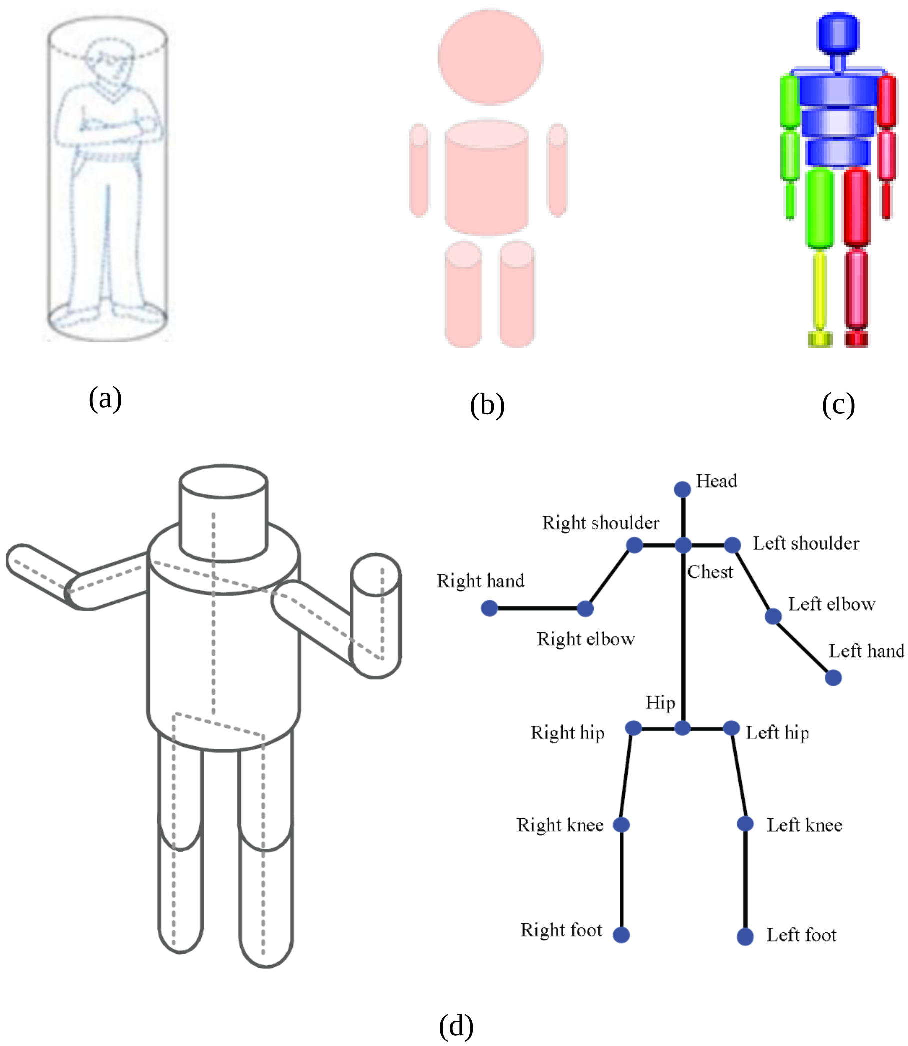

Figure 4.11: (a) One cylinder representation (b) Multi-parts representation (c) Multi-parts (d) Multi-parts with joint constraints representation

To address these limitations, an intermediate representation that involves dividing the human body into distinct regions can be used. Each region is represented by a geometric shape that closely approximates the human's one. For example, we can use a sphere (or a spheroid) to represent the head, a cylinder for the neck, and cylinders, ellipsoids, elliptical cylinders… for the upper body and so forth (Fig 5.11b-d). This intermediate representation enables us to navigate and access points near the human body effectively.

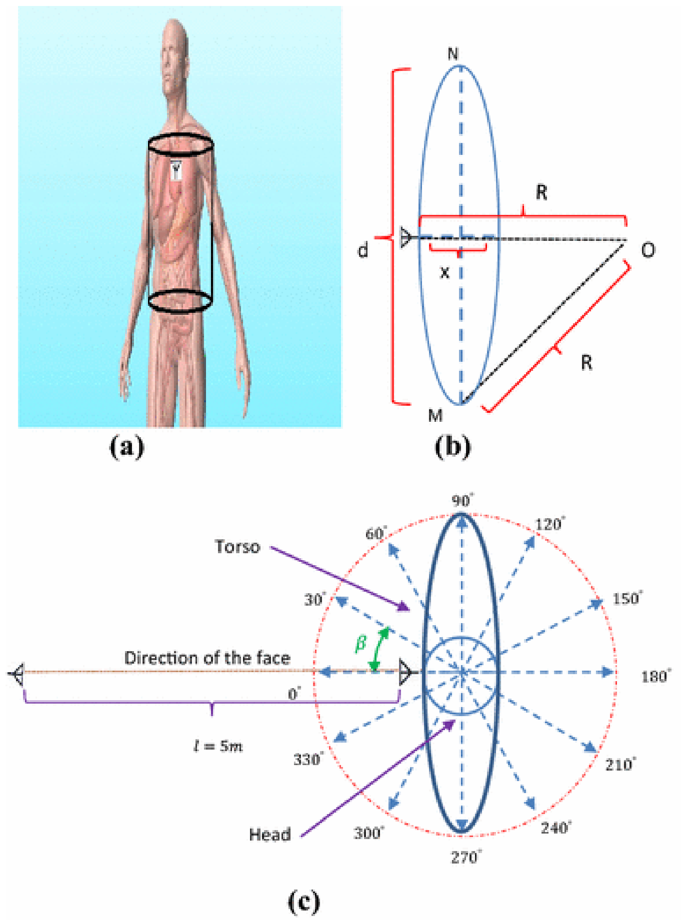

Figure 4.12: Modelling human body effect on ToA ranging using Ray Theory
(a) elliptical cylinder contouring the torso (b) top projection showing the ellipse
(c) the cylinder and the ellipse contouring the torso (Askarzadeh et al., 2017)

All these works depended on a cylinder model to represent the torso. We believe this is not effective for echography applications due to the need to reach some points of the patient that must be inside the cylinder in order to ensure the collision avoidance for all other points of the human body. So, we propose a new model using an elliptical cylinder, 3D ellipse elongated along an axis perpendicular to its surface, (Fig 4.12). This representation cannot generate an accurate model as the point cloud one, but at least it takes into consideration the empty area near the body better than the simple cylinder model.

We can also use equations to calculate the potential field around the obstacle without the need for extra computation power as we will see later in this chapter. Model detection in this case is easier than in the point cloud case because we only need to localize some markers on the human body which is easier than segmenting the whole body.

Due to the difficulty of modelling the lower part of the body and to simplify the discussed problem, we will introduce, in the following part, a detailed conceptual framework for the APF-based method to the upper human body collision avoidance using the elliptical cylinder model for the torso with arms which will be considered static during the interaction which represents the practical situation in the cPETRUS application as explained in chapter 1.

4.2 Conceptual framework for the APF-based method for human collision avoidance

We introduce multiple possibilities for the human collision model as shown in (Fig 4.13) illustrating the unreached areas near the human body in each case.

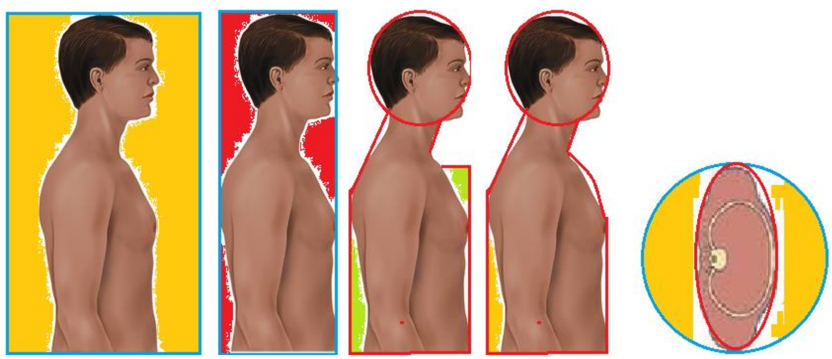

(a) (b) (c) (d) (e)

Figure 4.13: A comparison between different models for the human body's upper part

In this figure, it's illustrated how the chosen model can affect the reached area for the robot in variable cases:

(a) Considering a cylindrical envelope surrounding the human body with a diameter bigger than the width of the body and two arms
(b) Considering an ellipse cylindrical envelope
(c) Multiple segments (ellipse cylinder for the torso, cylinder for the neck, sphere for the head)
(d) Multiple segments with refining some sharp areas
(e) Cross-sectional top projection of the human upper body with the arms showing the difference between simple cylindrical and ellipse cylindrical envelopes.

By comparing between these models, we can recognize that the model shown in Fig 4.13c has more relevance (than Fig 4.13a, b cases) while preserving a simple geometry in relative to the refined one (Fig 4.13 d). So, we consider this model in the later calculations.

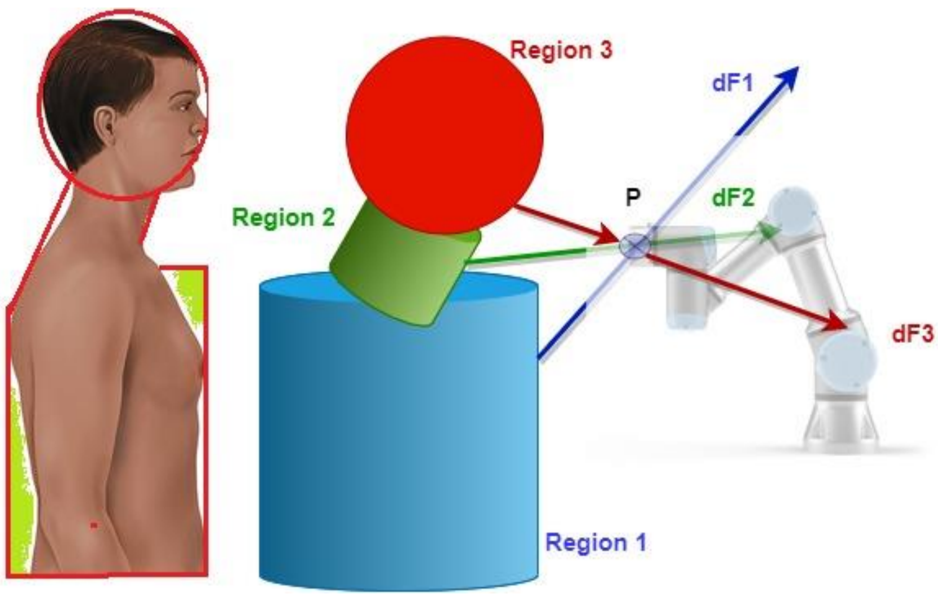

Figure 4.14: The human upper body collision model
using a sphere (for the head), a cylinder (for the neck), and an elliptical cylinder
(for the chest and arms) illustrating the repulsive forces affecting the robot

The resulting repulsive force that affects the robot is the sum of all repulsive forces coming from the different parts of the model. However, we need to investigate more in the potential field model to compute the value of this virtual repulsive force.

4.2.1 Potential field model

We propose various approaches to consider the potential repulsive field model. Table 4.1 contains propositions for the potential field and force expressions which ensure increase in the force value with the decreased distance between the robot and the obstacle. The general expression between the field and the force value is done in the equation:

$$F = -grad(U)$$

Where U is the potential field function, and F is the potential (repulsive) force. The choice of the approach depends on the force rate of change needed around the obstacle and this highly depends on the application. *E.g.,* when we need the robot reaches to very close areas around the obstacle with free movements a little far from it, it’s practically to use a high-degree approach like the magnet one. While when the robot only works near the obstacle without the need for reaching to very close places from the obstacle, then a simple approach (like static fixtures or linear) may be sufficient.

Table 4.1: Different approaches for the repulsive field and force model

Approach	Potential repulsive force	Potential repulsive field	remarks
Static fixture	$U = kr$	$F = -k$	Assigning a constant force value is similar to virtual fixture techniques that aim to prevent the robot from reaching the obstacle potential region
Linear	$U = \frac{1}{2}k(r_0 - r)^2$	$F = -k(r_0 - r)$	The repulsive force linearly increases while the robot is approaching the obstacle
Reciprocal	$U = k\log(r)$	$F = -k\frac{1}{r}$	The repulsive force reciprocally increases while the robot is approaching the obstacle
Gravity	$U = k\frac{1}{r}$	$F = -k\frac{1}{r^2}$	Model the obstacle as a mass that generates anti-gravity forces affecting the approaching robot
Magnet	$U = \frac{1}{2}k\frac{1}{r^2}$	$F = -k\frac{1}{r^3}$	Imagine the obstacle as a magnet that pushes away the approaching robot. This approach is well known in literature since introduced in (O. Khatib, 1985)

4.2.2 Obstacle effective parts

In most cases, not all the obstacle parts have the same effects on the human especially when they have different shapes. In this session we discuss the various ways of modelling the effective parts of the obstacle when calculating the repulsive forces. This is necessary when processing complicated obstacle shapes.

We describe the primitive approaches that can be taken into consideration to represent the effective parts as detailed in Table 4.2.

As described in the table, the obstacles may be classified into 4 types considering their shapes and dimensions when calculating the repulsive forces:

1) Point obstacle: the obstacle is significantly smaller compared to nearby objects or the robot, as shown in Fig 4.15a.
2) Line obstacle: the obstacle features an edge directed toward the checkpoint. It could possess a linear-like structure, resembling a cylinder or a rod with a small radius relative to its height and surrounding objects or the robot, as depicted in Fig 4.15b.
3) Surface obstacle: The obstacle's surface or a section of it is oriented towards the checkpoint. While the obstacle can have 2D or 3D shapes, only its surfaces produce repulsive forces, as illustrated in Fig 4.15c.
4) Volume obstacle: the mass within the obstacle volume generates repulsive forces, similar in topology to surface obstacles, but influenced by the material type or density. This concept is illustrated in Fig 4.15d.

Table 4.2: Different approaches for the obstacle effective part model

Point approach	**Line approach**	**Surface approach**	**Volume approach**
We consider the closest point of the obstacle to produce the repulsive force on the robot check point $F_{rep} = F(r)$	We consider the edge facing the check point to produce the repulsive forces (obstacle with sharp edges) $F_{rep} = \int_L dF(r)$ $dF(r) = g(r)dl$ dl is an elementary width on the obstacle effective edge	We consider a surface facing the check point to produce the repulsive forces $F_{rep} = \iint_S dF(r)$ $dF(r) = g(r)ds$ ds is an elementary surface on the obstacle effective surface	We consider a 3D volume to generate the repulsive forces $F_{rep} = \iiint_V dF(r)$ $dF(r) = g(r)dv$ dv is an elementary volume in the obstacle
Point obstacle	**Line obstacle**	**Surface (2d) obstacle**	**Volume (3d) obstacle**
The obstacle has small dimensions in relative to the near robot. (Fig 4.15a)	The obstacle has or forms an edge facing the check point. It may have a linear shape (cylinder or rod with small radius in relative to its hight and to nearby robots. (Fig 4.15b)	The obstacle surface or part of it faces the check point. The obstacle might have 2D or 3D shapes but only its surfaces generate repulsive forces. (Fig 4.15c)	The obstacle volume (or mass) or a part of it generates repulsive forces. The material type or density may affect the repulsive forces in this approach. (Fig 4.15d)

While the surface model is typically sufficient for general obstacle avoidance, there are scenarios where collisions with soft objects may be acceptable while those with solid objects are not. In such cases, it is important to consider the material nature and density of obstacles which becomes important when calculating repulsive forces if we need to consider a hybrid control that manage compliance and collision avoidance at ones. This approach is inspired by human behaviour, where individuals tend to navigate near soft objects with less caution compared to their movements near hard or sharp objects, where they exercise greater care and move cautiously to ensure safety in case of unexpected collisions. This hybrid technique can provide a balance between reachability and safety.

In more general cases, the obstacle may have a complicated topology in which it needs to be divided into some of these primitives to compute the repulsive forces generated nearby (see Fig 4.14).

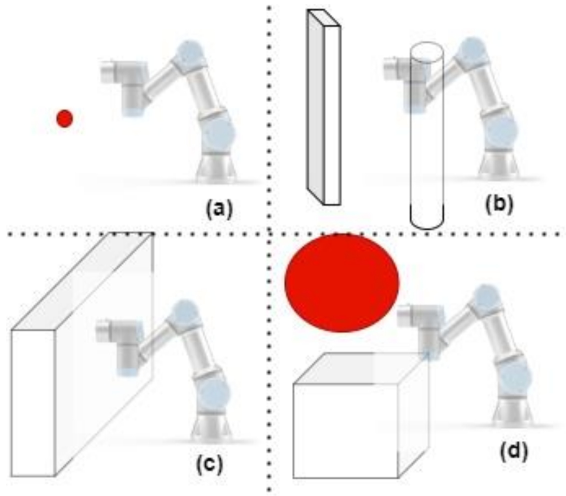

Figure 4.15: The different cases for the obstacle's shape

We suggest that in order to compute the repulsive forces affecting some point in the space, we only have to integrate the effects of the obstacle facing parts to this point. *E.g.* in Fig 4.15d, the obstacle has a cubic shape, then only the faces that are visible from the check point must be taken into consideration when integrating the elementary repulsive forces. This suggestion is considered while formulating the repulsive forces produced by the hollow cylindrical gantry in chapter 3.

In our case, we deal with a 3D human obstacle presented in Fig 4.14, and we don't consider compliant collisions in the obstacle avoidance problem which allows us to choose the 2D surface obstacle to model the human instead of the 3D obstacle approach. In this case, the total repulsive force is expressed in the equation (Eq 4.1):

$$F = \sum_{i=1}^{3} \iint_{S_i} dF_i \qquad \text{(Eq 4.1)}$$

As we see in the last equation, 3 primitives were considered to model the human upper part. Each primitive produces a force F_i that can be calculated through surface integral. The elementary repulsive forces resulted from the elementary obstacle surface is needed to complete the total repulsive force calculation. These 3 forces are summed up to calculate the total force F.

The following part will discuss the development of the repulsive force formula for these primitives be used in computing the total force used later in the collision avoidance algorithm.

4.2.3 Repulsive forces

The primitives used to form the human upper body has spherical and cylindrical (with circular or elliptic bases) shapes.

A- Repulsive forces for spherical obstacles

As Fig 4.14 shows, the human head can be modelled as a sphere. Due to the spherical symmetry, we can consider only the sphere's centre and radius R while calculating the repulsive force which allows us to consider the point obstacle approach. Hence, we only need to detect the distance r between the obstacle centre and the robot check point as illustrated in Fig 4.16.

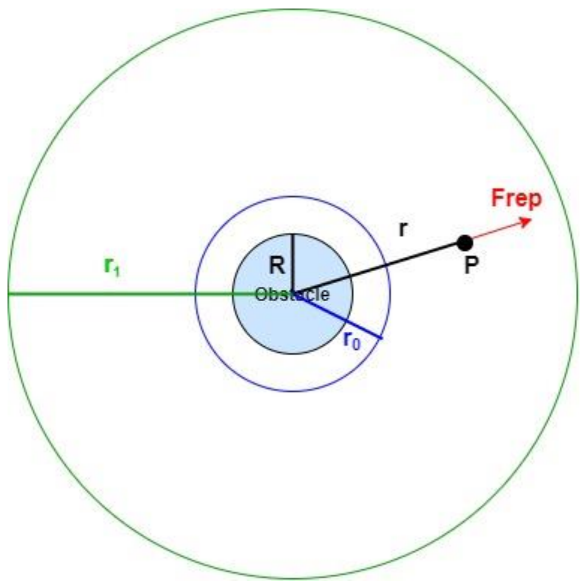

Figure 4.16: The repulsive force in the point approach case for the obstacle model

For more intuitive and realistic avoidance, we will not consider the static fixture approach to model the repulsive forces as it doesn't allow for gradually change in force value with the variation in value for the distance r. Also, we will not consider a high degree level like the magnet one to avoid high repulsive dynamic at the filed region edge r_0 which may lead to unstable behaviour. Fig 4.17 illustrates a comparison between the two other (reciprocal and the linear) approaches for the repulsive force model.

The potential field for the obstacle reaches the maximum distance r_1 (horizontal axis in Fig 4.17) where the repulsive force (vertical axis in Fig 4.17) has zero value. At the opposite, and very close to the obstacle at a distance r_0, the repulsive force has the maximum value F_{max} to prevent the robot from entering this zone to avoid collision and ensure safety. The equations (Eq 4.2a) and (Eq 4.2b), express the repulsive force as function of the distance r with considering the other parameters (r_0, r_1, F_{max}) in the linear and the reciprocal approaches respectively.

Linear approach Reciprocal approach

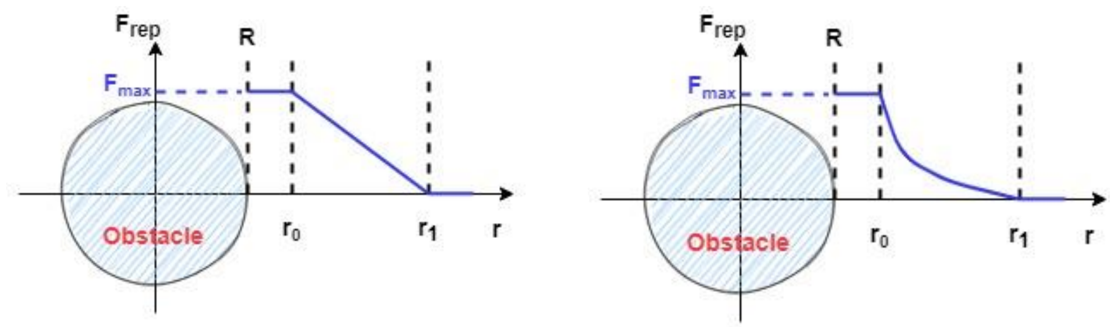

$$F_{rep} = \begin{cases} F_{\max}\left(1 - \dfrac{r - r_0}{r_1 - r_0}\right) & if \quad r_0 \le r \le r \\ F_{\max} & if \quad r < r_0 \\ 0 & if \quad r > r_1 \end{cases}$$

(Eq 4.2a)

(a)

$$F_{rep} = \begin{cases} F_{\max}\dfrac{r_1 r_0}{r_1 - r_0}\left(\dfrac{1}{r} - \dfrac{1}{r_1}\right) & if \quad r_0 \le r \le r \\ F_{\max} & if \quad r < r_0 \\ 0 & if \quad r > r_1 \end{cases}$$

(Eq 4.2b)

(b)

Figure 4.17: A graphic and an analytic comparison between the repulsive forces in the (a) linear approach (b) reciprocal approach

Both approaches can be suitable for the human collision avoidance. Choosing the approach to be used, depends on the desired behaviour for the repulsive forces which depends on the application.

B- Repulsive forces for cylindrical obstacles

The human neck and torso, when modelled for collision avoidance during H-R interaction, can be simplified as cylindrical structures, with the torso being a cylinder with an elliptical base, to account for more accurate shape representation, especially with the presence of arms as explained earlier. When a robot is navigating around these cylindrical surfaces, the challenge is to model the repulsive forces correctly, which help avoid collisions.

Since the cylindrical model has limited height, we can define different regions of interaction where the repulsive forces act differently:

1-Region 1 and region 3

This region refers to the space where the robot's checkpoint is close to the side surface of the cylindrical torso. Only the lateral cylindrical surface contributes to the repulsive force in this region. More specifically, only the closer half (or part) of this cylindrical surface, denoted as semi1 (see Fig 4.18), generates a repulsive effect. This is because the part of the surface farther from the robot will have negligible influence due to the distance and orientation.

The equation for calculating the repulsive force $F_{rep,1}$ for a point located in region 1 (or similarly in region 3) will depend primarily on the lateral surface's contribution S_1 (see Fig 4.18).

$$F_{rep,1} = \iint_{S_1} dF(r) \qquad \text{(Eq 4.3)}$$

1- Region 2 and region 4

These regions are situated outside the height of the cylindrical torso, meaning that both the lateral (side) surface and the top or bottom base surfaces of the cylinder contribute to the repulsive forces.

The repulsive force, for a point in region 2 (or region 4), must consider the effect of these two surfaces. In this part of space, the robot is either above or below the height of the torso, so the bases of the cylinder play an important role in generating the repulsive force.

The equation for calculating the repulsive force $F_{rep,12}$ for a point P2 located in region 2 (or similarly in region 4) will depend on the lateral surface's contribution S_1 (see Fig 4.18).

$$F_{rep,12} = \iint_{S_1} dF(r) + \iint_{S_2} dF(r) \qquad \text{(Eq 4.4)}$$

However, only the second part of the equation is considered if the point P2 exists directly above the upper base (or under the lower one) as illustrated in Fig 4.19. In this case the repulsive force is then perpendicular to the cylinder base.

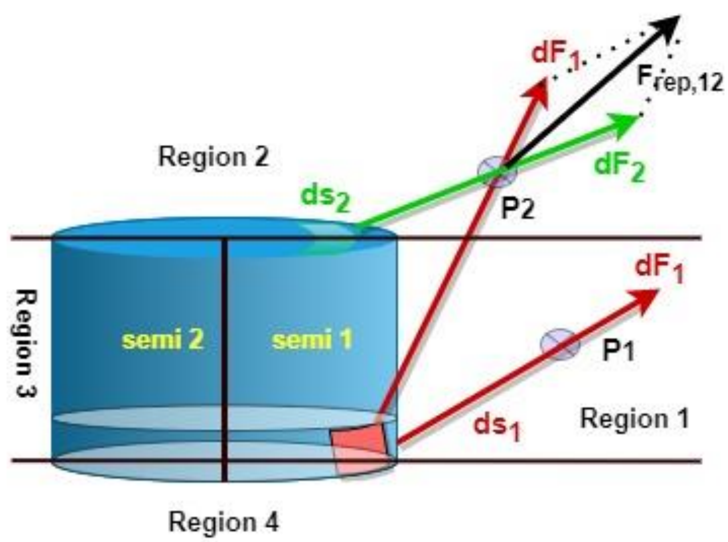

Figure 4.18: The repulsive forces in different regions around the cylinder

Repulsive force model

In Fig 4.19, a simplified model is presented for the potential field around the cylindrical obstacle. This model assumes that the repulsive forces are normal to the obstacle's surface (*E.g.* points P1 and P2) and decrease as the robot's distance from the surface increases. The cylindrical symmetry makes it practical to model the force behaviour in this way. However, at the boundary where region 1 and region 2 intersect (*E.g.* point P0), the force is simply modelled as a linear superposition, $F_0 = F_1 + F_2$ (see Fig 4.19), of the forces from the side and base surfaces. This model is inspired from the principle of superposition applied to gravitational, magnetic, and electric fields.

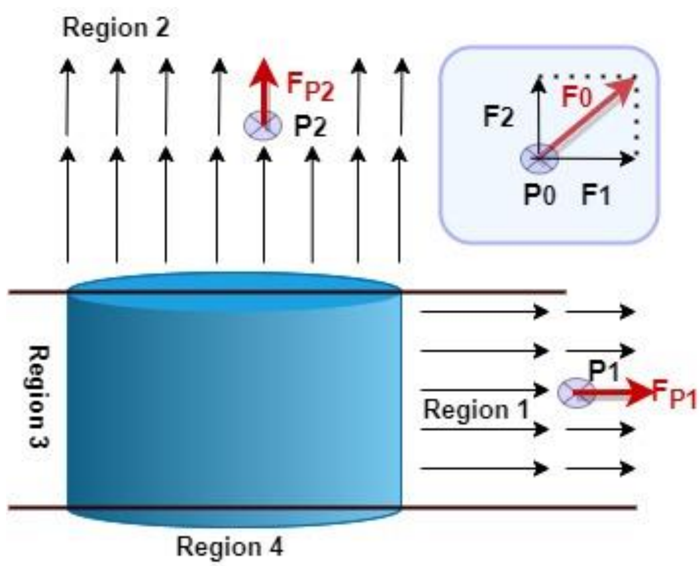

Figure 4.19: Simplified model for the repulsive forces around the elliptical cylinder

This linear combination, mentioned above, ensures force continuity but lacks smoothness at the transition between regions. Smoother transitions can be achieved using a smoothing function, such as a sigmoid function, to make the force model more practical for robotic navigation.

The simple proposed potential field model is useful when the robot is very close to the cylindrical surface because in such case, we can assume that the surface extends infinitely in that area according to the Field Theory. The field generated in this case is uniform (the field lines are parallel, meaning the direction of the repulsive force doesn't change, although its magnitude does). In such close proximity, we can simplify the calculation to focus only on the distance between the robot check point and the obstacle without needing to track the robot's exact coordinates.

However, this assumption breaks down when the robot encounters more complex or real-world obstacles where multiple surfaces face the robot check point. In those cases, we cannot assume that the force fields are uniform, and we must compute the effect of all these surfaces at the same time. A simple approach is to generalize the linear superposition, mentioned above, to be a linearly weighted combination of the fields generated by each surface. This can be translated to the following equations (based on Fig 4.19).

$$F_1 = k_1 \frac{1}{r_1}, F_2 = k_2 \frac{1}{r_2}, F_0 = \alpha_F F_1 + \beta_F F_2 \quad \text{(Eq 4.5)}$$

The coefficients α_F , β_F of this combination can be chosen as functions of the two distances r_1 and r_2. However, this method can still lead to discontinuous force behaviour, resulting in undesired robotic movements, especially near the obstacle's edges.

To address this issue, a more advanced model could be developed by integrating over the entire obstacle's surface. In this approach, we calculate the exact contribution of each part of the surface based on the robot's relative position. Only the effective parts of the surface (i.e., the parts close to the robot) would contribute significantly to the repulsive force, while distant or ineffective parts would have a minimal or null effect. The potential field lines in this case are curved near the obstacle's edge, as shown in Fig 4.20, comparing to the potential field lines in Fig 4.19.

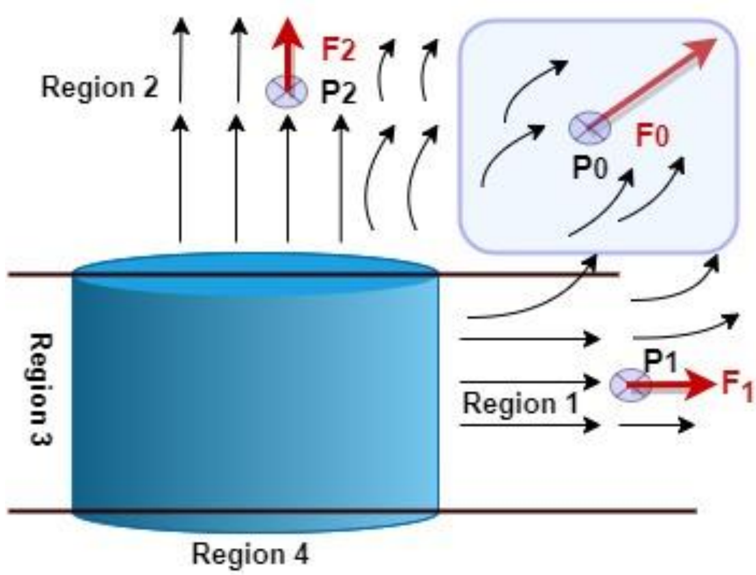

Figure 4.20: Smoothed repulsive forces model around the elliptical cylinder

Based on this discussion, we will derive, in the following part, the equations to calculate the repulsive force generated in a particular point, located in the space near a cylindrical (elliptical cylindrical) object based on the reciprocal force approach (detailed in Fig 4.17).

Global repulsive force calculation

In the following figure (Fig 4.21), the geometric vectors and coordinates are presented to explain the analytical calculation of the potential repulsive forces.

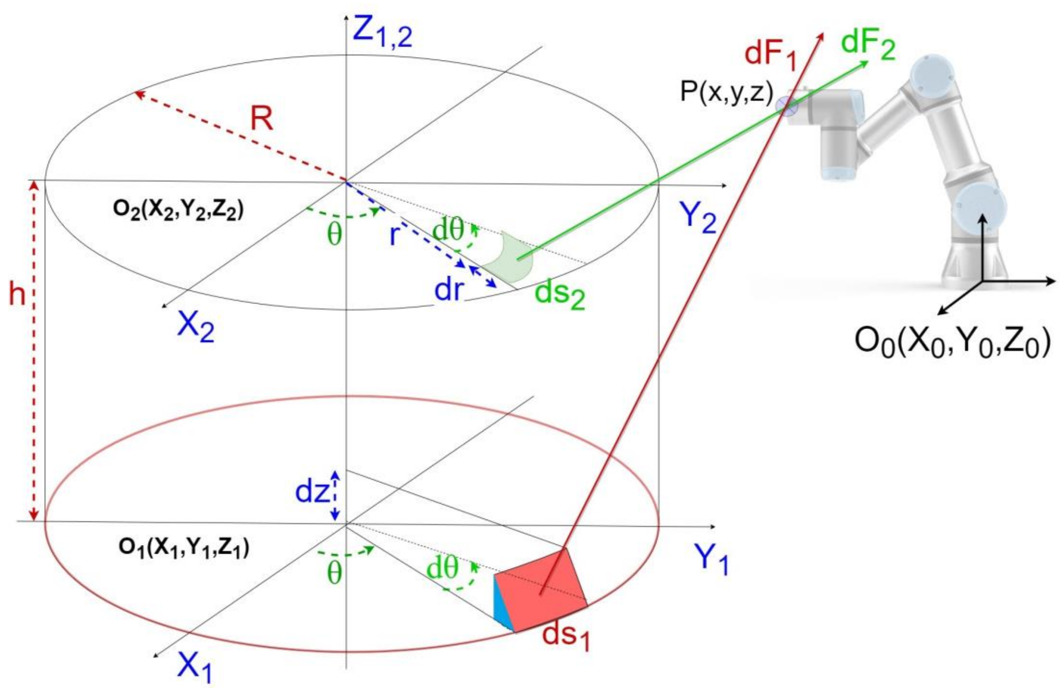

Figure 4.21: The elementary repulsive forces produced by elementary elliptical cylinder surfaces

We can use the dot product between the surface normal vector (which points outward from the obstacle) and the distance vector (pointing from the obstacle to the robot) to decide whether the part of the surface affects the robot check point with a repulsive force or not. If the dot product is positive, it indicates that the surface contributes to the repulsive force. If the dot product is negative or null, the surface does not affect the robot because it is too far or oriented in the opposite direction.

By integrating over the whole surface while only considering the effective parts, the calculated repulsive force would naturally reflect the physical proximity and orientation of the robot check point in relative to the obstacle.

To facilitate force calculation, we can define the cylindrical surface in Cartesian coordinates, assuming the cylinder is aligned with its own reference frame, as follows.

$$\frac{x^2}{a^2} + \frac{y^2}{b^2} + 1, \quad z = h \qquad \text{(Eq 4.6)}$$

This geometry allows as an easier way to perform the integral in polar or cylindrical coordinates. In these coordinates, we can define an elementary surface ds_2 as follows:

$$ds_2 = rdrd\theta \qquad \text{(Eq 4.7)}$$

The elementary surface ds_1 near a point $P_1(x_1, y_1, z_1)|_{O_1}$ expressed in the reference frame $O_1(X_1, Y_1, Z_1)$ is as follows:

$$ds1 = Rd\theta dz_1 \qquad \text{(Eq 4.8)}$$

Where:

$$R = \sqrt{x_1^2 + y_1^2} \qquad \text{(Eq 4.9)}$$

And:

$$x_1(\theta) = R\cos\theta,\ \ y_1(\theta) = R\sin\theta,\ \ \theta \in [0, 2\pi],\ \ z_1 \in [0, h] \qquad \text{(Eq 4.10)}$$

We need to write all expressions in cylindrical coordinates attached to the frame $O_1(X_1, Y_1, Z_1)$ to do the integral calculation in these coordinates.
In the ellipse we have:

$$R = \frac{ab}{\sqrt{b^2\cos^2\theta + a^2\sin^2\theta}} \qquad \text{(Eq 4.11)}$$

So, the equation (Eq 4.8) becomes,

$$ds_1 = \frac{ab}{\sqrt{b^2\cos^2\theta + a^2\sin^2\theta}} d\theta dz_1 \qquad \text{(Eq 4.12)}$$

The expression of the elementary force dF_1 resulting from the elementary surface ds_1 using the reciprocal approach is done as follows:

$$\overrightarrow{dF_1} = k_1 \frac{1}{\left\|\overrightarrow{P_1P}\right\|} \frac{\overrightarrow{P_1P}}{\left\|\overrightarrow{P_1P}\right\|} ds_1 \qquad \text{(Eq 4.13)}$$

Where k_1 is a proportional constant.
The force has the same direction of the vector $\overrightarrow{P_1P}$ and reciprocally depends on its norm.

The point P can be expressed in the reference frame O as $P(x, y, z)|_O$, or in the frame O_1 as $P(x', y', z')|_{O_1}$. Hence, $P(x, y, z)|_O = P(x', y', z')|_{O_1}$.

The vector $\overrightarrow{P_1P}$ is expressed then as:

$$\overrightarrow{P_1P} = \begin{pmatrix} x' - R\cos\theta \\ y' - R\sin\theta \\ z' - z_1 \end{pmatrix} \quad \text{(Eq 4.14)}$$

Based on these expressions, the elementary repulsive force dF_1 becomes:

$$\overrightarrow{dF_1} = k_1 \frac{1}{\left(x' - R\cos\theta\right)^2 + \left(y' - R\sin\theta\right)^2 + \left(z' - z_1\right)^2} \begin{pmatrix} x' - R\cos\theta \\ y' - R\sin\theta \\ z' - z_1 \end{pmatrix} ds_1 \quad \text{(Eq 4.15)}$$

By integrating on the total surface, we find the total repulsive force F_1:

$$\overrightarrow{F_1} = \int_0^h \int_0^{2\pi} k_1 \frac{1}{\left(x' - R\cos\theta\right)^2 + \left(y' - R\sin\theta\right)^2 + \left(z' - z_1\right)^2} \begin{pmatrix} x' - R\cos\theta \\ y' - R\sin\theta \\ z' - z_1 \end{pmatrix} d\theta dz_1 \quad \text{(Eq 4.16)}$$

As we can see the force value and direction is a function of the parameters $\overrightarrow{F_1}(a,b,h,x',y',z')$.

In a similar way, we can calculate the repulsive force F_2 resulted from the cylinder base's surface by expressing the vectors in the frame $O_2(X_2,Y_2,Z_2)$.

The elementary surface ds_2 near a point $P_2(x_2,y_2,z_2)\big|_{O_2}$ is expressed as follows:

$$ds_2 = rdrd\theta \quad \text{(Eq 4.17)}$$

Where:

$$r = \sqrt{x_2^2 + y_2^2} \quad \text{(Eq 4.18)}$$

And:

$$x_2(\theta) = r\cos\theta,\ \ y_2(\theta) = r\sin\theta,\ \ \theta \in \left[0, 2\pi\right] \quad \text{(Eq 4.19)}$$

The expression of the elementary force dF_2 resulting from the elementary surface ds_2 using the reciprocal approach is done as follows:

$$\overrightarrow{dF_2} = k_2 \frac{1}{\left\|\overrightarrow{P_2P}\right\|} \frac{\overrightarrow{P_2P}}{\left\|\overrightarrow{P_2P}\right\|} ds_2 \quad \text{(Eq 4.20)}$$

Where k_2 is a constant.

The force has the same direction of the vector $\overrightarrow{P_2P}$ and reciprocally depends on its norm.

The point P can be expressed in the reference frame O as $P(x,y,z)|_O$, or in the frame O_2 as $P(x'',y'',z'')|_{O_2}$. Hence, $P(x,y,z)|_O = P(x'',y'',z'')|_{O2}$.

The vector $\overrightarrow{P_2P}$ is expressed then as:

$$\overrightarrow{P_2P} = \begin{pmatrix} x''-r\cos\theta \\ y''-r\sin\theta \\ z''-z_2 \end{pmatrix} \quad \text{(Eq 4.21)}$$

Based on these expressions, the elementary repulsive force dF_2 becomes:

$$\overrightarrow{dF_2} = k_2 \frac{1}{(x''-r\cos\theta)^2+(y''-r\sin\theta)^2+(z''-z_2)^2} \begin{pmatrix} x''-r\cos\theta \\ y''-r\sin\theta \\ z''-z_2 \end{pmatrix} ds_2 \quad \text{(Eq 4.22)}$$

By integrating on the total surface (ellipse), we find the total repulsive force F_2:

$$\overrightarrow{F_2} = \int_0^R \int_0^{2\pi} k_2 \frac{1}{(x''-r\cos\theta)^2+(y''-r\sin\theta)^2+(z''-z_2)^2} \begin{pmatrix} x''-r\cos\theta \\ y''-r\sin\theta \\ z''-z_2 \end{pmatrix} r dr d\theta \quad \text{(Eq 4.23)}$$

As we can see the force value and direction is a function of the parameters $\overrightarrow{F_2}(a,b,h,x'',y'',z'')$.

In order to practically implement this calculation, we need to express the equations in a numeric form.

The equations' Numeric form

In order to avoid the need for analytical solution for the double integral, a numerical form can be used for the calculations. This approach involves performing a discrete integral by dividing the obstacle's surface into a grid of points then summing the elementary forces across all the grid points using double series.

By dividing the angle's interval [0, 2π] into N points and the cylinder height's interval [0, h] into M points, we can express the numerical elementary angle and height as follows:

$$d\theta = \frac{2\pi}{N}, \; dz_1 = \frac{h}{M} \quad \text{(Eq 4.24)}$$

Then, the numerical form (in Eq 4.16) for calculating the repulsive force F_1 becomes,

$$\overrightarrow{F_1} \simeq k_1 \frac{2\pi h}{N.M} \sum_{i=1}^{N}\sum_{j=1}^{M} \frac{1}{(x'-R\cos\theta_{i,j})^2+(y'-R\sin\theta_{i,j})^2+(z'-z_{1_{i,j}})^2} \begin{pmatrix} x'-R\cos\theta_{i,j} \\ y'-R\sin\theta_{i,j} \\ z'-z_{1_{i,j}} \end{pmatrix} \quad \text{(Eq 4.25)}$$

The same procedure can be followed for the calculation of F_2. By dividing the angle's interval [0, 2π] into N points and the cylinder radius's interval [0, R] into M points, we can express the numerical elementary angle and height as follows:

$$d\theta = \frac{2\pi}{N}, \ dr = \frac{R}{M} \quad \text{(Eq 4.26)}$$

Then, the numerical form (in Eq 4.23) for calculating the repulsive force F_2 becomes,

$$\overrightarrow{F_2} = k_2 \frac{2\pi R}{N.M} \sum_{i=1}^{N} \sum_{j=1}^{M} \frac{1}{\left(x'' - r_{i,j}\cos\theta_{i,j}\right)^2 + \left(y'' - r_{i,j}\sin\theta_{i,j}\right)^2 + \left(z'' - z_2\right)^2} \begin{pmatrix} x'' - r_{i,j}\cos\theta_{i,j} \\ y'' - r_{i,j}\sin\theta_{i,j} \\ z'' - z_2 \end{pmatrix} \quad \text{(Eq 4.27)}$$

While performing these summations, we need to consider only the effective points of the grid by verifying the dot product as mentioned earlier.

After calculating the repulsive force resulting from each primitive (a simple part of the complex shaped human obstacle), we can use the sum of these forces to perform the APF obstacle avoidance detailed in chapter 3.

4.3 Summery

As we'll discuss later in our future directions of work, we'll soon be working on examples of constrained environments where humans are present, to provide a proof-of-concept for this model. Through a comprehensive platform of collision avoidance strategy using the Artificial Potential Field (APF), this chapter contributes to advancing safety in human-robot interaction, leading for safer collaboration between humans and robot manipulators. While preliminary insights have been discussed, further work is required to fully implement and validate the proposed approach. In the next chapter, we will introduce the integration of the APF collision avoidance in a robot teleoperation task to respond to the requirements presented in chapter 1.

CHAPTER 5
Obstacle-free Teleoperation
Robot-assisted tele-echography with obstacle avoidance

In the previous chapters, we proposed a reactive obstacle avoidance technique that depends on the Artificial Potential Field (APF) for the robot manipulator's whole body. This technique enables the robot to navigate the CT-PET gantry without collision with the borders. In this chapter we will introduce the integration of the APF obstacle avoidance motion planner in a teleoperation control structure to allow the medical agent performing the tele-echography during the CT-PET imaging procedure with assuring the patient and the robot safety. It also details the experimental results and observations, emphasizing the effect of the APF algorithm presented in chapter 3, and virtual haptic feedback on the radiologist's ability to respond to obstacles during tele-echography tasks.

5.1 Introduction

As mentioned in chapter 1, we aim to integrate the ultrasound probe inside the CT-PET gantry device to perform multimodal imaging, which can enhance the quality and the anatomical accuracy of PET images in based on the INSERM teams' studies (Perez-Liva et al., 2018, 2020; Provost et al., 2018). The team used a pre-clinical scanner that combines PET-CT and UUI offering multiple combinations for imaging. This combination of anatomical, functional, and molecular imaging with PET-CT-UUI represents a high-performance and clinically transferable technology for biomedical research.

We also mentioned in chapter 1 that, in PRISME laboratory, we will present a new robotic solution that allows the insertion of an ultrasound probe inside the gantry of a PET-CT imaging device, offering clinicians a new approach to Tele-echography under PET-CT test. In such applications, a robot is used to guide an ultrasound probe held by a specific tool within hollow cylinders (gantries) where a patient is located. The robot manipulates the probe to perform echography, under expert control. In this application, the robot movements to perform the echography needs to be performed through teleoperation (noted T), comanipulation (noted C), either in a separated mode, or in a combined one (noted TC^2) (Joseph Diab, 2021). Additionally, once the task is completed, the robot must navigate and exit the tool holding the US probe outside the confined environment. Throughout these sub-tasks, the complex poly-articulated robot mechanism must avoid collisions with the CT-PET device boundaries.

We have also seen that due to the physical principles governing medical devices (e.g., CT scans, PET scans) in which the robots operate there are some challenges (mentioned in chapter 1) that make it necessary to assign the obstacle avoidance sub-task to an autonomous path planner rather than assigning it to the human operator to perform it through teleoperation. Assigning obstacle avoidance to the human operator may compromise the performance of the primary task, and they may struggle to succeed in either task. Hence, a more effective approach is to implement an automatic algorithm directly on the slave robot, which can independently handle the obstacle avoidance task while the main teleoperation task remains the focus.

We have seen in chapter 3 the design of such collision-free path planner using the APF method (Elahres et al., 2021). However, this algorithm needs to be integrated in a teleoperation control scheme to perform the task described in this application. In the following sections, we will describe the features of this integration approach.

5.2 Human operator’s role

During robot teleoperation, human operators play an important role in effective obstacle avoidance within complex environments. Supplied with visual feedback from cameras and sensors mounted on the robot, operators can observe their surroundings, identifying potential obstacles that might exist in the robot's path. The teleoperation interface, enriched with features like live video feeds and haptic feedback devices, serves as the operator's command centre. In this dynamic interaction, operators possess the ability to manually intervene and adjust the robot's trajectory in real-time based on the information provided by the robot's sensors. However, the difficulty of performing manual obstacle avoidance during teleoperation becomes evident in highly dynamic environments. The challenge lies in the operator's need for swift and precise decision-making, especially when faced with unforeseen obstacles. Another challenge comes from the limited human potentials. Human operator can’t perform multiple tasks efficiently at the same time. In tasks that requires high concentration like medical diagnostics, where the medical staff needs to manipulate the robot in the patient’s area of diagnosis while observing the resulting image and watching the scene from time to time, it is very difficult for the medical staff to deal with the safety issues related to the robot motion. So even if the environment is not highly dynamic in such tasks, it is important to assign the obstacle avoidance subtask to an autonomous path planner implemented on the slave robot.

The incorporation of haptic feedback systems allows operators to not only visualize but also feel the robot's environment, enhancing their ability to detect obstacles and make swift adjustments despite the inherent complexities. Maintaining a high level of situational awareness, operators navigate the robot while being attuned to its position and potential risks. Proper training, familiarity with the robot's capabilities, and the utilization of advanced obstacle detection systems contribute to the operator's ability to make informed decisions and guide the robot safely through its surroundings. Effective communication channels between the operator and the robot, coupled with appropriate control strategies and emergency stop mechanisms and procedures, further empower operators to ensure the robot's safe and efficient navigation, avoiding collisions and optimizing performance in diverse and challenging scenarios.

5.3 Control architecture for the teleoperation task

Our laboratory has been already working on mechatronic design and control for robot-assisted tele-echography applications for years like presented at the beginning in (Gourdon, Poignet, Poisson, Parmantier, et al., 1999) or more recently in (Diab, 2021). In this chapter, is proposed a position control architecture for both unilateral and bilateral teleoperation to test the integration with obstacle avoidance for tele-echography purposes. It only depends on mapping the positions received from the master side to the slave robot workspace like in (Omarali et al., 2019). We modified the structure by using the *Jacobian-transpose Control (JT)* (Leeper et al., 2013) to generate the motion, similarly to the reactive control motion planning. Fig 5.2 and Fig 5.4 show the whole control structure of unilateral and bilateral teleoperation respectively.

5.4 Obstacle avoidance during unilateral teleoperation

The integration of the teleoperation task with the obstacle avoidance one can be easier seen as there are two sources of action that affect the robot at the same time, the first represents the desired signals (position, velocity, or force) generated from the remote site through teleoperation, and the second represents the reactive control signals resulting from the collision-free path planner (Fig 5.1). Each of these source signals can be represented by a force affecting the robot manipulator.

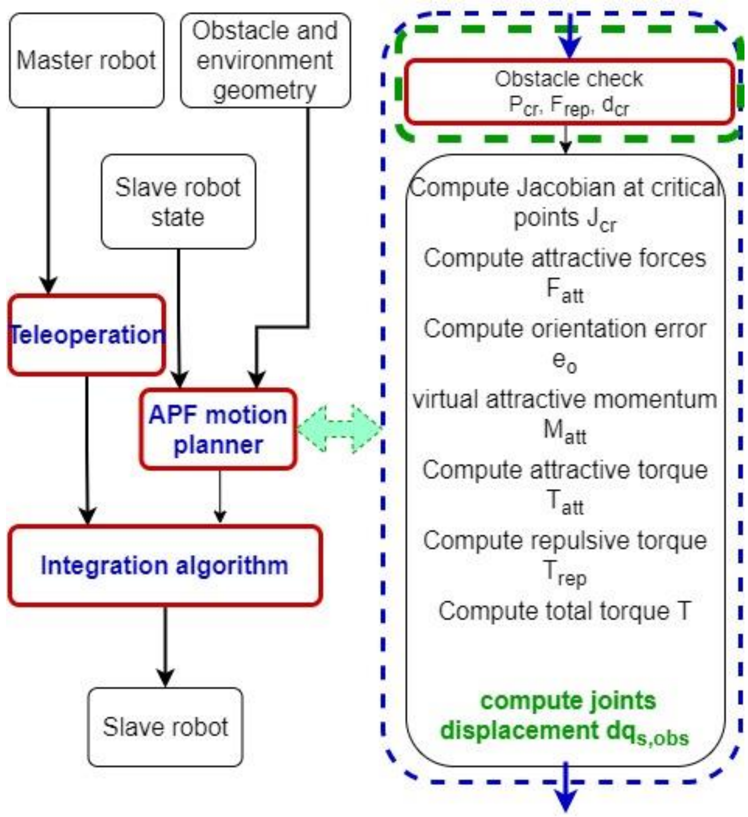

Figure 5.1: Unilateral teleoperation with APF obstacle avoidance flowchart

The overall effect is the sum of these signals as shown in Fig 5.2. The following figure demonstrates a schema diagram of the APF algorithm, presented earlier in Fig 3.2 integrated in the unilateral teleoperation task.

To perform this integration of teleoperation and obstacle avoidance commands in a control structure, the challenge of managing heterogeneous control inputs arises. The obstacle avoidance algorithm, using an Artificial Potential Field (APF), generates virtual repulsive forces, while the teleoperation task provides position, velocity, or physical force commands. To integrate these control signals effectively, it is necessary to unify their representation. This can be achieved either by converting the teleoperation position/velocity commands into virtual force-based signals or by transforming the virtual repulsive forces from the APF into physical position/velocity commands.

Building on the existing APF approach, where virtual forces are mapped into displacements in the robot's joint space, we propose transforming the teleoperation position/velocity commands, received from the *Phantom OMNI* haptic interface, into equivalent displacements in the joint space as well using the *Jacobian-transpose Control (JT)*. This unified representation enables the direct summation of the control inputs, allowing us to dynamically adjust their influence using weighted gains. By tuning these gains, in real-time, we can prioritize either obstacle avoidance or teleoperation control based on the task requirements and the actual situation of the environment. This approach not only resolves the heterogeneity between the control signals but also provides a flexible, real-time solution for balancing safety and operator control in teleoperated robotic systems.

After converting the teleoperation signals into robot joints displacements, they are combined with those generated by the obstacle through the APF collision avoidance algorithm. These displacements are subsequently added to those generated by the teleoperation task.

The resulting robot motion is determined by the sum of the displacements from both the teleoperation input and the obstacle avoidance algorithm. However, this approach does not guarantee complete obstacle avoidance, as there may be situations where the teleoperation commands counteract or even cancel the effects of the APF, leading to potential collisions.

To address this issue, we introduce a weighting parameter α that dynamically adjusts the importance of each control input based on the proximity of the obstacle. When the obstacle is distant, the teleoperation commands dominate, driving the robot's motion. Conversely, when the obstacle is near and there is a high risk of collision, the obstacle avoidance subtask is prioritized, dominating the teleoperation input.

This approach, expressed in (Eq 5.1) and (Eq 5.2), ensures a smooth transition between teleoperation and collision avoidance.

$$dq_s = (1 - \alpha_{APF})dq_{s,teleop} + \alpha_{APF}\, dq_{s,obs} \quad \text{(Eq 5.1)}$$

$$\alpha_{APF} = 1 - \frac{min(d_{act}, d_{tr,max})}{d_{tr,max}} \quad \text{(Eq 5.2)}$$

Where d_{act}, $d_{tr,max}$ are the actual and a threshold distance respectively between the robot segments and obstacle. And α_{APF} is a parameter expresses the obstacle avoidance priority.

Fig 5.2 presents the implemented control architecture to perform the integration of the APF algorithm in a unilateral teleoperation task.

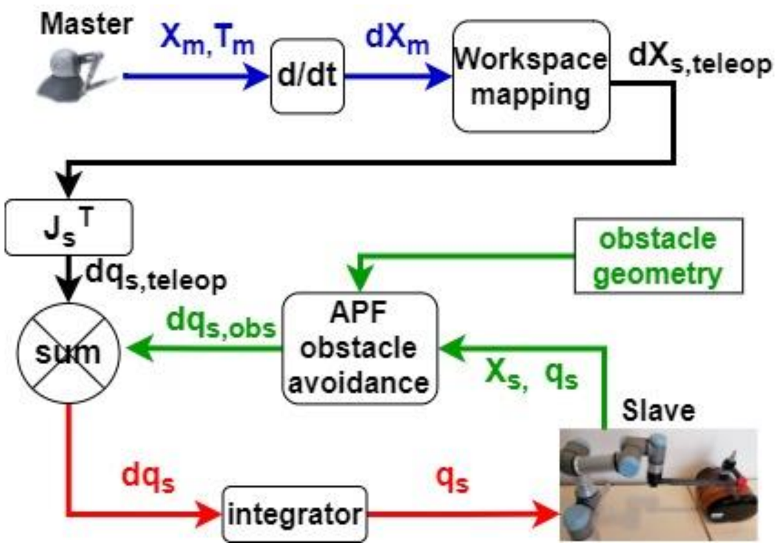

Figure 5.2: Control architecture for the integration of APF with unilateral teleoperation

5.5 Obstacle avoidance during bilateral teleoperation

The integration of unilateral teleoperation and obstacle avoidance ensures the safety of the patient and equipment and decreases the radiologist exhaustion during examination due to the autonomous collision avoidance. However, performing unilateral teleoperation for a robot, where commands are sent from the human operator to the robot without receiving feedback from the robot, often leads to a lack of haptic feedback or sensory information for the operator. This lack of feedback can result in these challenges:

1. The operator has limited understanding of the forces or constraints the robot is experiencing in its environment. Also, he is not aware of potential collisions or unsafe interactions, leading to damage to the robot or its environment.

2. The operator needs to rely more on visual feedback which leads to higher cognitive effort to interpret the robot's environment and actions, which in turn can increase fatigue and reduce efficiency.

In bilateral teleoperation, feedback is sent back to the operator (such as haptic feedback), allowing for more intuitive and safer control of the robot, as the operator can "feel" the environment through the robot. This feedback depends often on force/torque sensors fixed on the robot’s end-effector or integrated in the robot joints. In robot-assisted echography (*E.g.* tele-echography), these sensors are used to supply the human operator with the sense of touch to perform robotized task in a more realistic way.

We introduce here another approach of virtual haptic feedback that depends on the repulsive forces produced by the APF collision avoidance sub-task (more details exist in the next paragraph). Similarly to the integration of the APF collision-free planner with a unilateral teleoperation control architecture, we implemented the integration with a bilateral teleoperation using the virtual haptic feedback. Fig 5.3 illustrates the schema diagram of integrating the APF algorithm with the bilateral teleoperation task. Fig 5.2 presents the implemented control architecture to perform this integration. As in the unilateral teleoperation case, the bilateral structure of the system generates the desired displacements for the slave robot. These displacements are then mapped to the workspace of the slave robot using the *Jacobian-transpose Control (JT)* to be later modified by means of the APF planner, using the equations (Eq 5.1) and (Eq 5.2), as presented in Fig 5.4.

5.6 Virtual haptic feedback

Haptic control for teleoperation represents a major technological advance in the field of robotics and telemanipulation. It offers human operators an immersive and intuitive experience by enabling the transmission of tactile and haptic sensations between the operator and the remote robot. Thanks to this bi-directional communication, the operator, here a medical expert, can perceive sensory information from the remote robot, such as resistance to movement, forces applied and obstacles encountered, while being able to react instantly by adjusting his own actions. This real-time exchange of information enables a more accurate control and a better understanding of the remote environment, improving dexterity and safety in operations.

Incorporating the virtual repulsive forces generated by the Artificial Potential Field (APF) for collision avoidance into haptic feedback can significantly enhance the operator's situational awareness during teleoperation with keeping the physical sensor feedback dedicated to the main task (tele-echography) as described above. By converting the APF's repulsive forces, which depend on the distance between the robot and surrounding obstacles, into haptic feedback, we can provide the operator with real-time, tactile information that assists in obstacle avoidance and improves safety. We propose a method where the magnitude of the virtual repulsive forces, determined by the APF algorithm, is mapped to a haptic interface that the operator can feel. This haptic feedback would increase as the robot approaches an obstacle, providing a force proportional to the proximity of the obstacle. The closer the robot gets to an obstacle, the stronger the haptic feedback becomes, enabling the operator to "sense" the environment through the teleoperation system.

In order to simulate the sensation of approaching the obstacle, we use the virtual forces that the obstacle produces $F_{s,rep}$ after mapping it to the master side workspace $F_{m,rep}$ to generate haptic forces on the master side F_m using an impedance-based controller (Eq 5.3) as illustrated in Fig 5.4. The controller balances the haptic device in equilibrium point to get red off the gravity forces when the human tries to manipulate the device.

$$F_m = k(X_0-X_m) + F_{m,rep} \qquad \text{(Eq 5.3)}$$

Where k is a constant, X_0 is the (x, y, z) coordinates of the set point for the master device (*Phantom OMNI*) end-effector, and X_m is the actual (x, y, z) coordinates of the master device end-effector.

This impedance-based controller achieves equilibrium, cancelling gravitational forces during manipulation by the human operator. While dynamic environments necessitate responses to the relative position and velocity between the operator and the obstacles, in the case of medical imaging tasks where the device gantry and patient remain static, the proposed spring model informs the human operator in case of involuntary patient movements on obstacle avoidance operations. In dynamic tasks and environments, this impedance-based model is more suitable for giving the human operator information about the relative velocity between the slave robot and the surrounding obstacle before a collision occurs.

One of the most important benefits of using the described virtual haptic feedback is enhancing the human operator' spatial awareness. By providing haptic feedback based on the distance to obstacles, the operator gains an intuitive sense of how close the robot is to potential collisions, even when visual feedback is limited. Which in turn can improve safety, because the operator is naturally guided to adjust the robot's trajectory to avoid collisions.

The virtual haptic feedback in parallel with the weight α introduced in (Eq 5.1) and in (Eq 5.2), can also enhance the balance between human control (through teleoperation) and obstacle avoidance, the human operator remains in control of the teleoperation task but is subtly assisted by the APF-driven feedback. Hence, it allows for a better human-robot collaboration. The following figure demonstrates a schema diagram of the integration of the APF algorithm with the bilateral teleoperation using the proposed approach. Fig 5.4 presents the implemented control architecture to perform the integration of the APF algorithm in a bilateral teleoperation task.

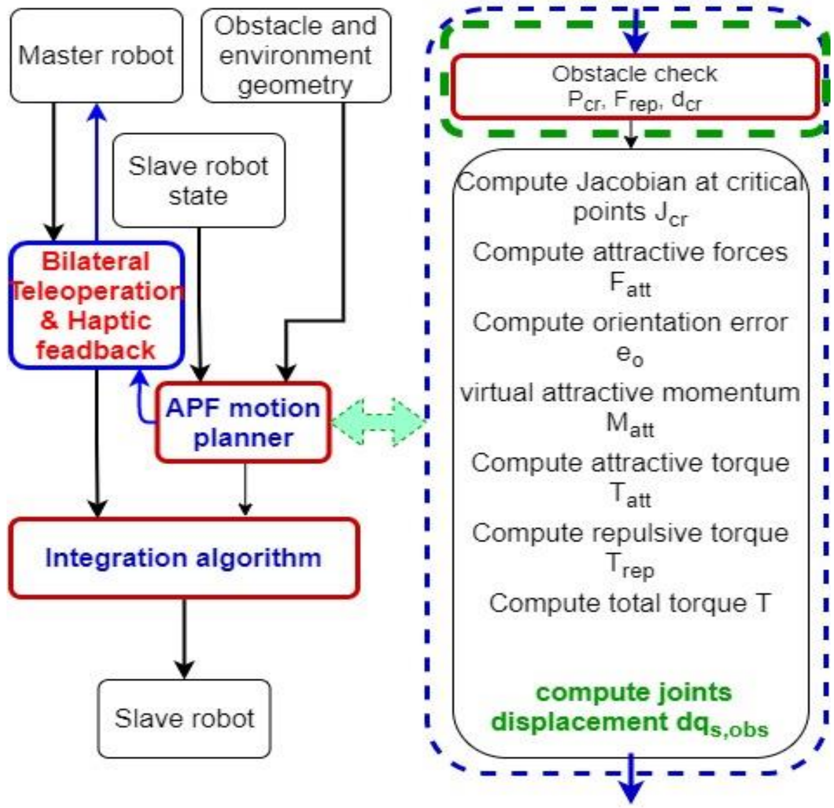

Figure 5.3: Bilateral teleoperation with APF obstacle avoidance flowchart

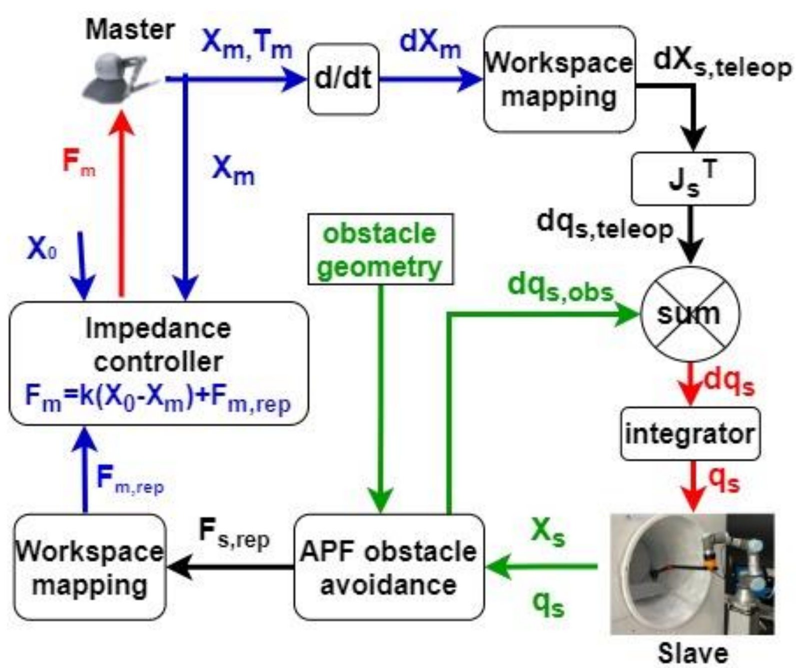

Figure 5.4: Control architecture for the integration of APF with bilateral teleoperation

5.7 Experimental results

We conducted the experiments in laboratory, with the 6 *Degrees-of-Freedom (DoF) UR3e* cobot as slave device and the haptic *Phantom OMNI* (APPENDIX B) as master device, in structured environments representing clinical-like and industrial-like ones. The algorithm has been implemented using *Robotic Operating System* (ROS1, APPENDIX C).

5.7.1 The APF-based obstacle avoidance

We performed some experiments on the implementation of the APF algorithm detailed in chapter 3 taking into consideration multiple practical situations.

1- APF-based spherical obstacle avoidance in a medical-like context

We are interested in positioning the ultrasound probe in a desired pose on the human body using the robot. Instead of a dedicated probe holder robot, we performed the experiment using the *UR3e*. As shown in Fig 5.5a, the US probe, guided by the cobot, has to follow a predefined path on a phantom of the patient's anatomy to perform the medical diagnosis without colliding with some static obstacles nearby. The different tests carried out during this experiment have shown that the APF algorithm can generate a collision-free path or stop the robot in case of risk. The tests consist of using APF algorithm to generate paths between a start and an end point each time taking into consideration the existence of the obstacle modelled by a sphere. The tests showed no collision between obstacle and any robot segments.

2- APF-based spherical obstacle avoidance in an industrial-like context

This experiment demonstrates assembly operations in robotic cells like industrial ones, where the robots are usually operating in known and constrained environments. Robotic cycles are repetitive (most often pick and place ones), well-defined and optimized, and of course, with collision avoidance guarantees. However, in particular situations (malfunction or sudden changes in the environment), it is necessary the robot plans a safe path until reaching its goal avoiding any collision between its parts and the obstacle. Fig 5.5b shows the *UR3e* trying to follow a path between two positions avoiding collision with the obstacle nearby. As in the previous case, the tests showed that the APF algorithm allows the generation of a collision-free path.

3- Emulating tele-echography in MRI Gantry

This experiment demonstrates an echography operation in a clinical application in which our laboratory is involved which consists of the fusion of two imaging modalities.

A robot telemanipulates an ultrasound probe on a patient, now located inside the Gantry of a Magnetic Resonance Imaging scanner (MRI). In order to test the performance of the robotic motions outside of the clinical environment, we developed a facsimile platform of a PET as shown in Fig 5.5c.

Due to the large size and the movements of the probe holder as shown in the same figure, a high risk of collision between the robot parts and the PET gantry exists which leads to the importance of a secondary obstacle avoidance control to support the teleoperation task. We have performed different tests of probe guidance inside the gantry by guiding the robot from an initial position to a desired one using the APF algorithm.

The approach allowed moving the probe to the requested position without collision with the gantry borders. However, the application requires knowing precisely the organs position to be diagnosed which imposes the interference of the physician to adjust the probe position on the patient using teleoperation. Therefore, in the second series of experiments, we combine teleoperation with APF.

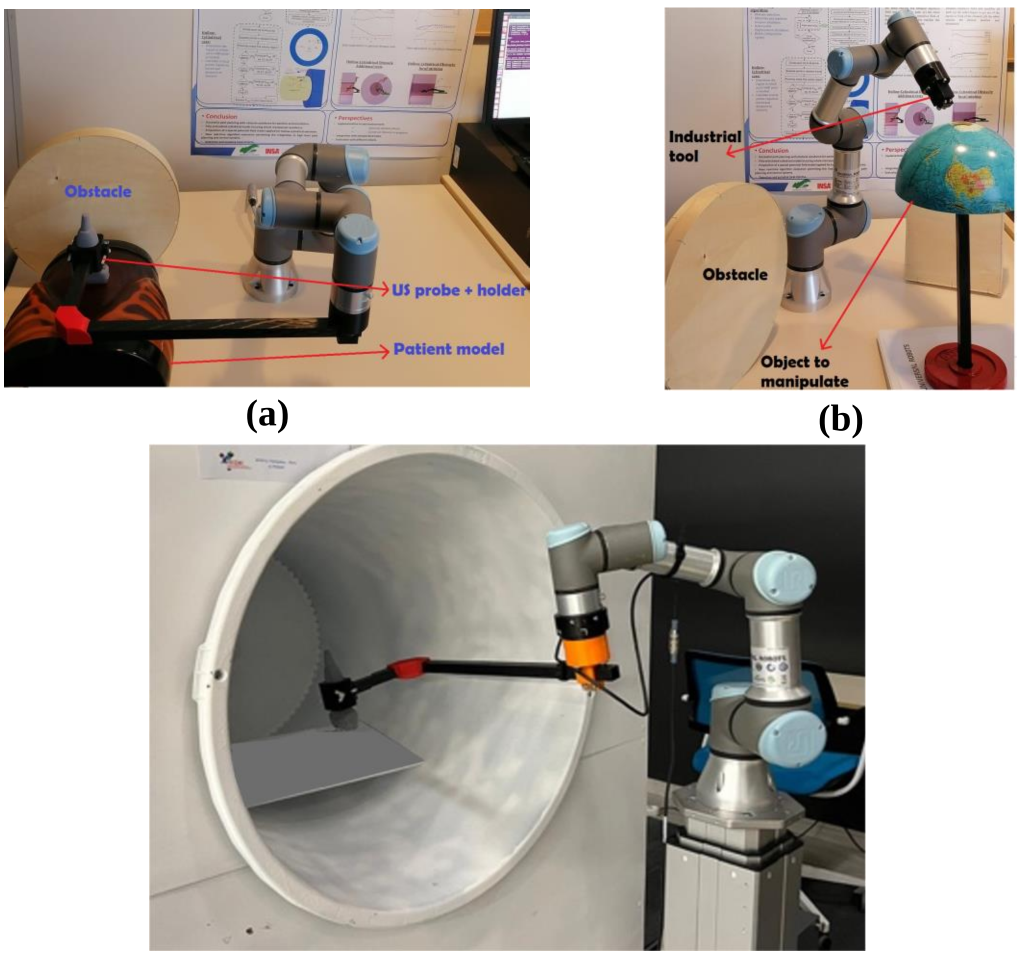

(a) (b) (c)

Figure 5.5: Experimental setup to test APF algorithm
(a) in medical-like context (Experiment1) (b) in industrial-like context (Experiment2) (c) in medical context for cylindrical obstacle (Experiment3)

5.7.2 The APF integration with unilateral teleoperation

To test the method that we have proposed for the integration, we performed some experiments using the setup shown in Fig 5.6.

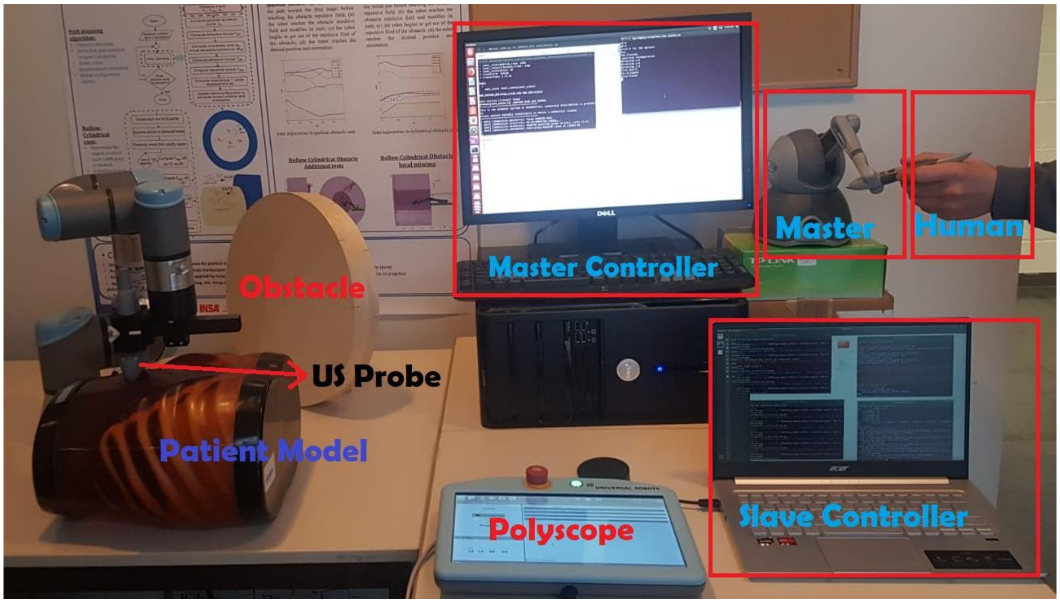

Figure 5.6: The configuration of the equipment used in the APF integration with teleoperation

4- APF motion planning and teleoperation – without obstacle collision

We repeated the first experiment (1) demonstrated in Fig 5.5a after the integration of the teleoperation task without the existence of obstacles to test only the integration of attractive forces generated by the goal point. The motion of the robot is generated between two poses using the APF algorithm with the possibility of modifying the path through teleoperation. Fig 5.7 shows the x, y, and z trajectories for both the master and slave robots.

The first part of the plot "pure APF motion planning" describes the trajectories in the first stage of the experiment where the slave robot motion is generated only by the APF algorithm that tries to move the probe from an initial to a final position. At some point in time, the human operator interferes to modify the path of the salve robot by manipulating the master one as demonstrated in the second part of the plot "Teleoperation with APF motion planning".

The human operator tries to oppose the motion generated by the APF algorithm to clearly demonstrate the effects of combining both modalities at the same time on the plot. We can see how Xs and Zs (axis of the slave robot motion) change direction while the teleoperation task is running in a way that teleoperation cancels the APF effect and creates an opposing effect. However, Ys axis stays in the same direction but at a higher speed because of teleoperation which sums up the APF effect. At the end of the teleoperation stage, the APF algorithm generates the motion alone again as the plot shows.

5- APF-based obstacle avoidance with unilateral teleoperation

By incorporating the teleoperation task from the last experiment (4) into the second one (2) and adding a spherical obstacle, we were able to modify the robot task to move between two points while avoiding a spherical obstacle. As a result, the APF algorithm generates an obstacle-free path, and teleoperation can modify this path. Fig 5.8 shows the x, y and z trajectories for both the master and slave robots.

The first part of the plot describes the trajectories where the motion of the slave robot is generated only by the APF algorithm which tries to move the end effector from an initial position to a final one. At some point in time, the robot reaches the obstacle field and the APF algorithm modifies the motion in order to avoid it. Then, the human operator interferes to modify the robot path through teleoperation as demonstrated in the third part of the plot.

The plot shows how the slave robot Xs, Ys, and Zs trajectories start to change behaviour when detecting the obstacle. We can see also how Xs and Ys change direction while the teleoperation task is running in a way that teleoperation cancels the APF effect and creates a motion in the opposite direction on these two axes.

Discussion

While APF-based obstacle avoidance has shown promising results, there are still some limitations that need to be addressed. The APF approach may not be suitable for certain types of environments, such as those with multiple dynamic obstacles or highly irregular surfaces. Additionally, the design of the potential function and the selection of parameters can significantly affect the performance of the system, and thus require careful consideration and tuning.

The local minima problem needs to be rethought due to the additional effect of teleoperation that can possibly cancel the APF effect even if the human operator might be able sometimes to get out of this through intentional disturbances. But it is not the case all the time.

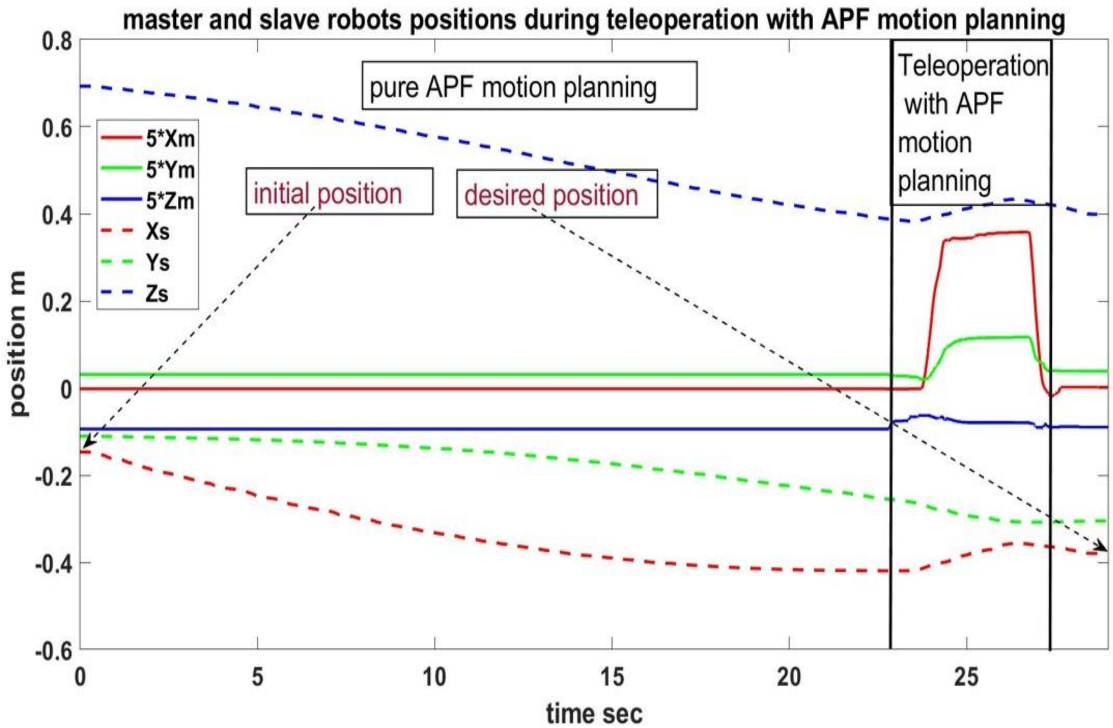

Figure 5.7: Task space trajectories for master (Xm, Ym, Zm) and slave (Xs, Ys, Zs) robots during the APF motion planning and teleoperation – without obstacle collision, experiment (4)

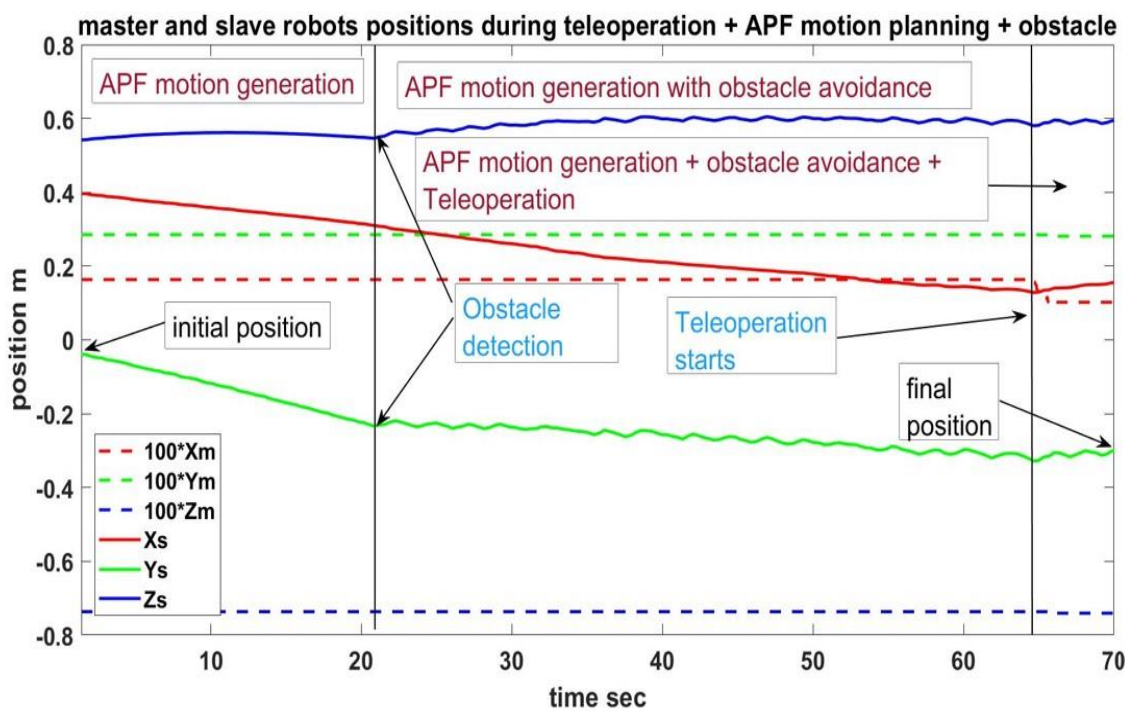

Figure 5.8: Task space trajectories for master (Xm, Ym, Zm) and slave (Xs, Ys, Zs) robots during the APF-based obstacle avoidance with unilateral teleoperation, experiment (5)

5.7.3 The APF integration with bilateral teleoperation

We modified the setup used in unilateral teleoperation presented in Fig 5.6 to implement the virtual haptic feedback described earlier. We show here, in Fig 5.9, the X, Y, and Z trajectories of both master and slave robot during the experiment. In this experiment we used the APF algorithm to generate the path between two points passing through an obstacle without the intervention of the human operator to register the haptic response at the master side due to the obstacle alone.

We can see from this figure that each time the robot reaches the obstacle potential field region a response is generated at the master side modifying the trajectories of the haptic device and that informs the user to take the obstacle into consideration during tele-echography manipulation.

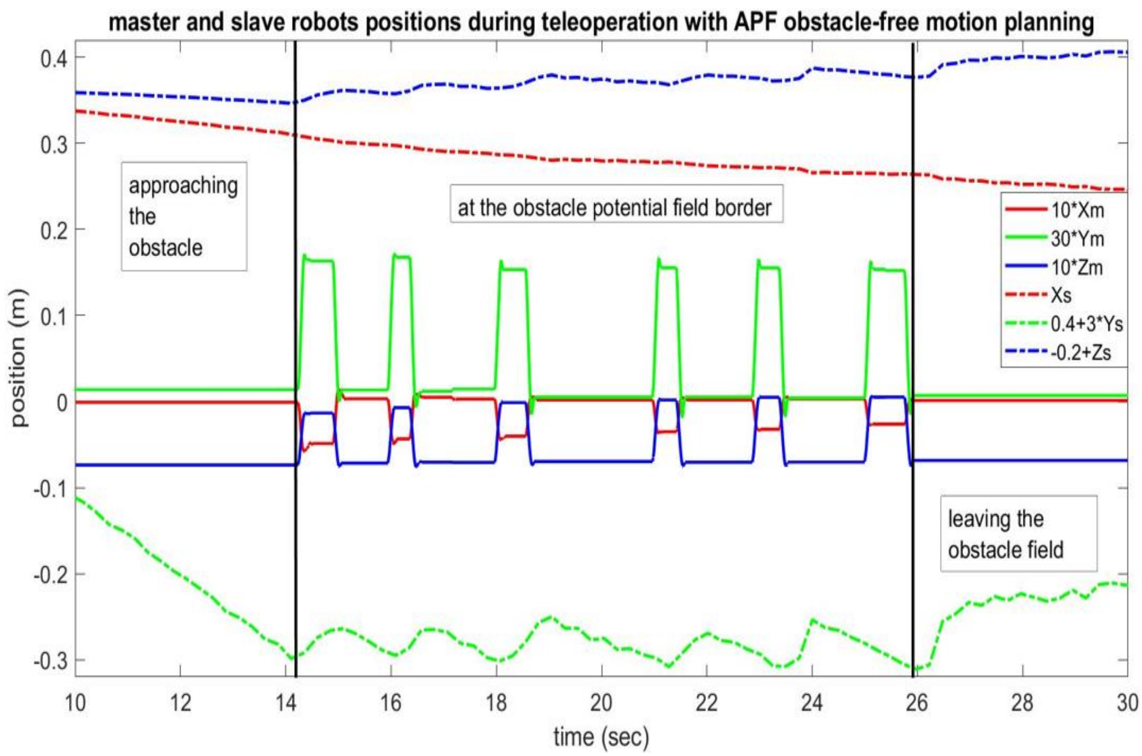

Figure 5.9: Task space trajectories for master (Xm, Ym, Zm) and slave (Xs, Ys, Zs) robots

In Fig 5.10 and Fig 5.11, we highlight the delay between the generation of virtual repulsive forces generated by the APF algorithm near the obstacle at the *UR3e* slave robot side and the haptic response of the *OMNI* master device.

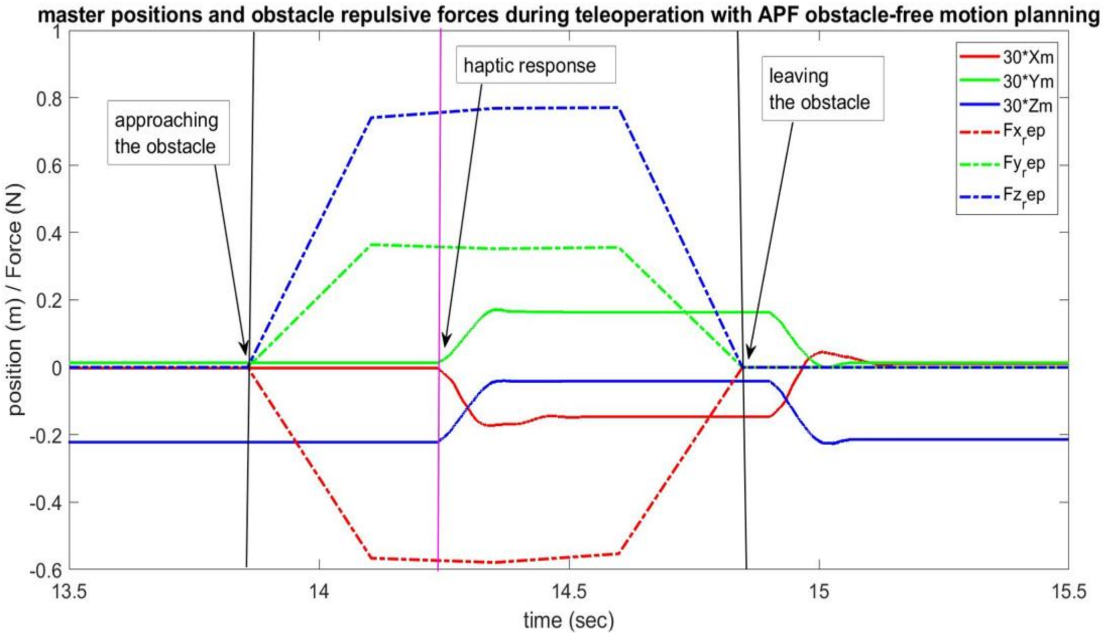

Figure 5.10: Time delay between obstacle virtual repulsive forces (Fx, Fy, Fz at slave side) and master robot trajectories (master side Xm, Ym, Zm)

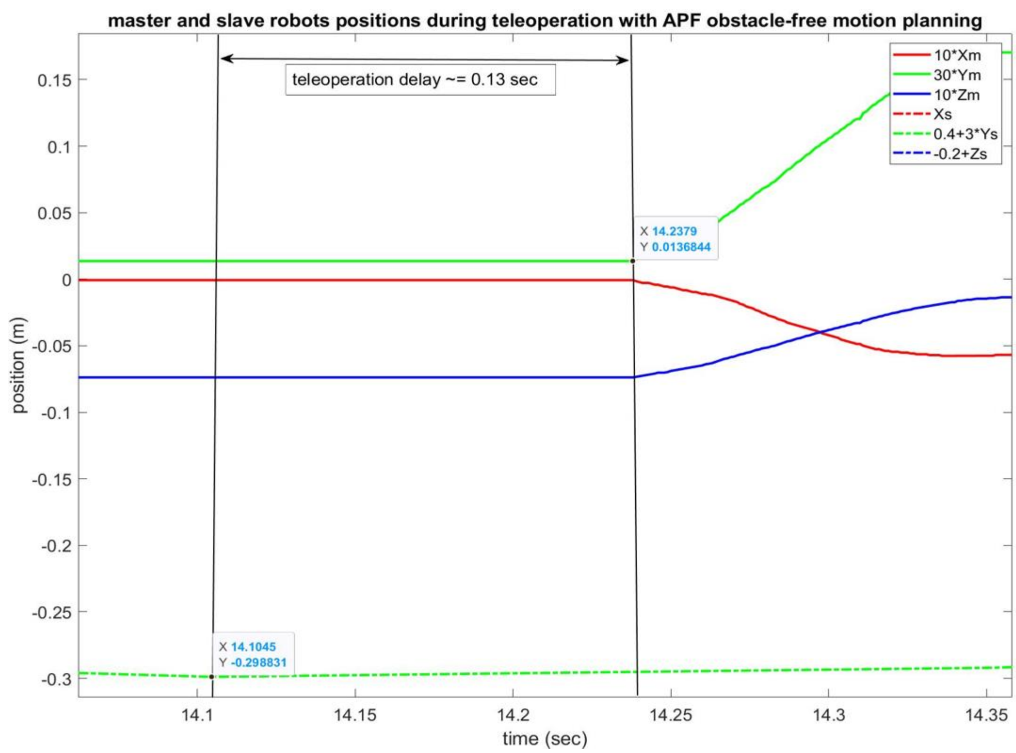

Figure 5.11: Time delays between slave robot trajectories (Xs, Ys, Zs at the slave side) and master robot trajectories (Xm, Ym, Zm at the master side)

As it appears on the plot, the response time is about 0.5 sec (Fig 5.10) that needs to be added to the human reaction time (about 1 s). This response time (0.5 sec) consists of the teleoperation delay which is about 0.13 sec (Fig 5.11) added to the impedance controller's (implemented on the master side) response time.

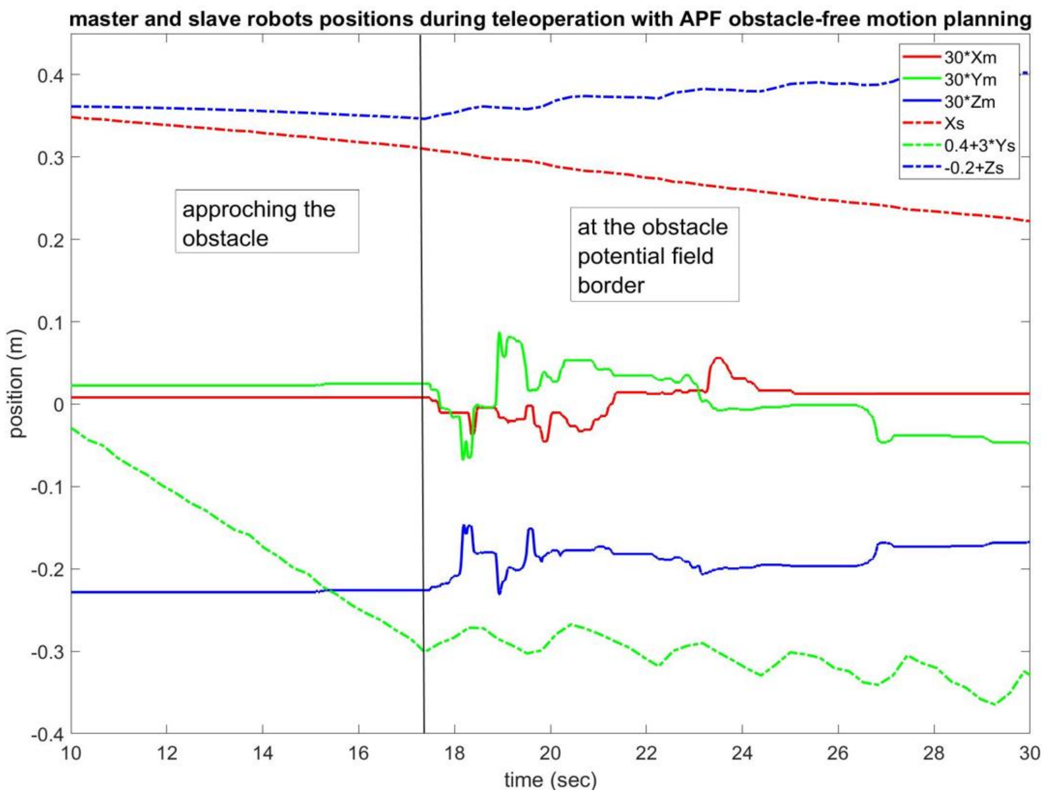

Figure 5.12: Slave (Xs, Ys, Zs) and master (Xm, Ym, Zm) robots' trajectories during tele-echography with obstacle avoidance

We can assume that this delay of (0.5 sec) is due to the use of *Virtual Machine* to run the *ROS* on a *Linux* operating system which doesn't assure exact real-time behaviour. However, this needs to be tested through the implementation of the algorithm without the use of a *Virtual Machine*. In practice, there is a risk of collision due to this delay in addition to the medical operator discomfort while performing tele-echography. The lower dynamic environments, where the objects are moving relatively slowly, the APF algorithm, with the safety margins used before collision, can still avoid collision even in the existence of such delay.

In another experiment, we conducted tele-echography near the obstacle. The human operator was able to feel the haptic forces generated due to approaching the obstacle. So, he modified the path of the teleoperation with his hands to continue tele-echography task while keeping the robot away from the obstacle. The difference between the behaviour of the master robot between this experiment and the first one is that human contact forces are added here to the haptic feedback generated from the obstacle. Fig 5.13 presents the X, Y, and Z trajectories of both master and slave robot during this last experiment.

In this chapter we introduced the integration of the APF-based obstacle avoidance path planner in a teleoperation control structure to allow the medical staff performing the tele-echography during the CT-PET imaging procedure with assuring the patient and the robot safety. The chapter described the materials and methods used for the experimental setup.

Conclusion

In medical procedures such as tele-echography integrated with CT-PET scans, where safety is crucial, this thesis addresses the integration of collaborative robotic systems with the Artificial Potential Field (APF)-based obstacle avoidance algorithm. The work contributes to the understanding of how collaborative robots (cobots) can be used in such complex environments by investigating the combination of several disciplines such as safe robotic motion planning, medical imaging, and human-robot interaction.

Robot-assisted multimodal imaging

The basis of this research, covered in Chapter 1, is the integration of ultrasound and CT-PET imaging under robotic guidance. The development of this system required overcoming the technical challenges that arise when dealing with multimodal imaging techniques within confined environments. This work demonstrated how robotic assistance could enhance diagnostic and interventional procedures through the selection of a suitable collaborative robot (the *UR3e*). The integration of this robotic system in this context offers new avenues for more comprehensive medical interventions. The combination of these imaging modalities with robotics is a step toward medical imaging that can improve patient outcomes.

Human-robot interaction and safe motion planning

The fundamental concepts presented in Chapter 2 provided a better understanding of physical human-robot interaction (pHRI) and safe motion planning. It discussed the development of collaborative robotics increasing trend toward robots sharing workspaces with humans. This discussion focused on the challenges of safe motion planning, particularly in environments that include human operators. The development of teleoperated robotic systems for tasks like echography was enhanced by the special focus on safety, which was investigated in standards such as ISO/TS 15066. The same chapter introduced key concepts such as levels of autonomy and highlighted the need for a hybrid approach that blends local planning methods with teleoperation. The discussion set the stage for more advanced applications of these concepts in later chapters, particularly in developing robot-assisted echography systems where safety, precision, and adaptability are key.

Collision avoidance using Artificial Potential Field algorithms

The Artificial Potential Field (APF) method was theoretically introduced in Chapter 2 as an efficient solution for real-time obstacle avoidance technique during teleoperation, offering predictable robot behaviour due to the human-like concept of repulsive and attractive fields which is easy to understand. We also showed that the APF method requires few parameters to be tuned, making it easy to implement and integrate into teleoperation. Finally, with appropriate modifications, APF can be designed to plan in dynamic environments by updating virtual forces based on sensor feedback.

Chapter 3 presented in detail the application of the APF method for a possible "real-time" path planning, with a specific focus on robot-assisted medical procedures. The proposed algorithm uses APF to guide the robot from an initial to a desired pose (position and orientation), avoiding spherical and hollow cylindrical obstacles. The robot is modeled using a poly-articulated cylinder model to measure the distance to the obstacle. The simulation results using MATLAB and Robotics Toolbox demonstrated the efficacy of the APF algorithm in guiding robotic manipulators, such as the *UR5*, through complex environments while avoiding both spherical and hollow cylindrical obstacles. Then the implementation on a real robot, the *UR3e*, showed successful collision avoidance and successful local planning as a part of global path planning task which is suitable for the integration with teleoperation. However, there has been some failure in other areas that need to be improved. During teleoperation, the human operator can intervene to help the robot getting out of the local minima regions.

The work in Chapter 4 also expanded the application of APF in the context of human-robot interaction. The modelling of human-like obstacles with more intermediate representations, such as elliptical cylinders, provided a conceptual advancement. By accounting for the variability in human anatomy, this research advanced the field of safe human-robot collaboration. These insights have practical implications for ensuring that robots can operate safely alongside humans, particularly in medical environments where patient safety is a top priority. This framework will help design a collision-free path planner to perform safe tele-echography during CT-PET scans.

APF-based collision avoidance with teleoperation

Chapter 5 presented the successful integration of the APF algorithm within a teleoperation control structure to allow the medical staff to perform the tele-echography during the CT-PET imaging procedure. The collision-free bilateral teleoperation, based on the APF algorithm and the virtual haptic feedback, allowed operators to perform tasks in confined environments while minimizing the risk of collisions. This integration represents a significant advancement in the field of tele-echography in constrained environments, providing operators with enhanced control and situational awareness during critical procedures.

The experimental results and observations, particularly in chapter 5, demonstrated the feasibility of using APF for real-time motion planning in teleoperated medical procedures. However, the challenges identified, including the local minima problem and delays in haptic feedback, highlighted areas for further improvement. Future work will need to address these limitations, especially as robotic systems are applied in increasingly complex and dynamic medical environments.

Contributions and Future Directions

In summary, this thesis makes significant contributions to the fields of robotics, motion planning, and medical technology. It offers a robust framework for integrating robotic systems into clinical environments, with a particular focus on enhancing the safety of tele-echography. The application of the APF algorithm and its integration with teleoperation

systems presents a promising solution for improving precision and reducing the cognitive load on medical operators during procedures.
Short-term research efforts should focus on:

- Refining the APF algorithm to address challenges such as:
    - Local minima: changing the length of the temporal horizon used to detect the existence of local minimum which reduces the latency before exiting this region. and add some feature to choose the proper direction and value of the third virtual force which is used to get out the local minimum region which is now not adapted to all the possible situations.
    - Dynamic obstacles: depending on the feedback coming from the optical tracker, we can precise the obstacle's position and orientation. In short-term, we can simulate this feedback through the generation of the obstacle's path manually in the code.
    - Further tuning its parameters for smoother robot path generation: the path created right now contains vibrations around the borders of the obstacle's potential field. So, the behaviour is similar to bang-bang control one, which is not desired to exist in the robot's path. Instead, we think of using the derivative of the distance to the obstacle to add some PID behaviour for the robot joint displacement dq created by the APF algorithm which, we believe, will be an important and new contribution to the Artificial Potential Field APF-based methods.
- Extending APF implementation for human collision avoidance. Starting with MATLAB simulations, we will develop the code necessary for the cylindrical obstacle, based on the method proposed in chapter 4. Then we will integrate it to the one already developed for spherical obstacle. The experiment will be implemented on the *UR3e* to avoid a phantom of the human's torso which we have prepared for this.
- Improving the teleoperation structure to minimize response delays through improvements in software choice and setup. We will use a version of ROS installed on the Linux operating system without using the Virtual Machine.

For medium-term research directions:

- Upgrading the haptic device, such as replacing the *Phantom OMNI* (offering only 3 DoF and limited force feedback 3.3 N) with a more advanced system like *Force Dimension's lambda.7* (offering 7 DoF and 20 N of feedback), which is available now in our laboratory. This device will certainly enhance control over the ultrasound probe and improve virtual haptic feedback. Implementing dual haptic feedback would allow medical staff to sense both patient stiffness and nearby obstacles which enhances tele-echography.

- Integrating an optical tracking system, like the *NDI Polaris Vega*, would improve dynamic obstacle collision avoidance by adding visual sensory feedback.
- Introducing compliance control mechanisms to enable hand-guiding of the robot to perform the clinical whole task which improves usability and safety.
- Performing clinical experiments in a hospital (possible future project) for tele-echography under CT-PET scan.
- Applying the obstacle avoidance integrated with teleoperation to un industrial platform such as a nuclear plant or satellite maintenance.

In conclusion, the integration of collaborative robots into medical imaging and diagnostic procedures represents an important development in healthcare technology. By addressing the technical challenges of safe motion planning and human-robot interaction, this PhD thesis has improved the safety and efficiency of robotic systems in medical applications.

List of works published on this thesis work:

A- Papers in conference proceedings:

1. M. Elahres, A. Fonte and G. Poisson 2021. Evaluation of an Artificial Potential Field Method in Collision-free Path Planning for a Robot Manipulator. *Proceedings of the 2nd International Conference on Robotics, Computer Vision and Intelligent System,* Volume1: ROBOVIS, ISBN 978-989-758-537-1, pages 92-102. https://www.semanticscholar.org/paper/Evaluation-of-an-Artificial-Potential-Field-Method-Elahres-Fonte/6897f850b6e1b8570ff5e570f647103d0f487e42
2. M. Elahres, A. Fonte and G. Poisson 2023. Artificial Potential Field APF-based Obstacle Avoidance Technique for Robot Arm Teleoperation *2023 27th International Conference on Methods and Models in Automation and Robotics (MMAR).* https://www.researchgate.net/publication/373857062_Artificial_Potential_Field_APF-based_Obstacle_Avoidance_Technique_for_Robot_Arm_Teleoperation
3. Mustafa ELAHRES, Aïcha FONTE, and Gérard POISSON 2023. Robot-assisted tele-echography with obstacle avoidance for CT-PET-US diagnostic *Conference on New Technologies for Computer and Robot Assisted Surgery (CRAS) 2023. No open access yet.* https://cras-eu.org/program/

B- Posters:

1. M. Elahres, A. Fonte and G. Poisson 2021. Evaluation of an Artificial Potential Field Method in Collision-free Path Planning for a Robot Manipulator. *PRISME Laboratory seminar*: Poster Presentations, Thursday, Nov. 25th 2021.
2. M. Elahres, A. Fonte and G. Poisson 2021. Evaluation of an Artificial Potential Field Method in Collision-free Path Planning for a Robot Manipulator. *International Conference on Robotics, Computer Vision and Intelligent Systems (ROBOVIS),* online streaming, ROBOVIS21-1A: Poster Presentations, Thursday, Oct. 28th 2021. https://www.insticc.org/node/TechnicalProgram/robovis/2021/presentationDetails/106528
3. M. Elahres, A. Fonte and G. Poisson 2023. Robot-Assisted Methodology from Tele-echography to PEEK Process Manufacturing. *French-Italian Workshop on Robotics 4.0 for factories of the future,* French-Italian Workshop on Robotics 4.0 for factories of the future 8th June 2023 in Paris. Poster 180 second presentation. https://fr-it-robots4fof.sciencesconf.org/

APPENDIX A: *Universal Robot (UR)* manipulator model

This appendix contains information that can be useful while modelling *Universal Robot* 6 *DoF* manipulators, in particular, *UR3e* which is used for the implementation during this research.

A.1. The *UR3e* Cobot Denavit-Hartenberg (DH) Parameters

The Denavit-Hartenberg (DH) Parameters are used to describe the links/joints geometry of a serial-chain robot. They have been adopted for standard kinematics analysis in serial-chain robots. The community has come to call Craig-style DH Parameters as 'modified', with the original DH Parameters interpretation as 'standard'. The modified DH parameters have certain advantages over the standard (the main one being that a Craig coordinate frame rotates right at its joint, rather than distal from the joint as in Paul). The Cartesian reference frame definitions for the *UR3e* manipulator are shown in Fig A.1. Table A.1 gives the associated modified (Craig convention) DHm parameters.

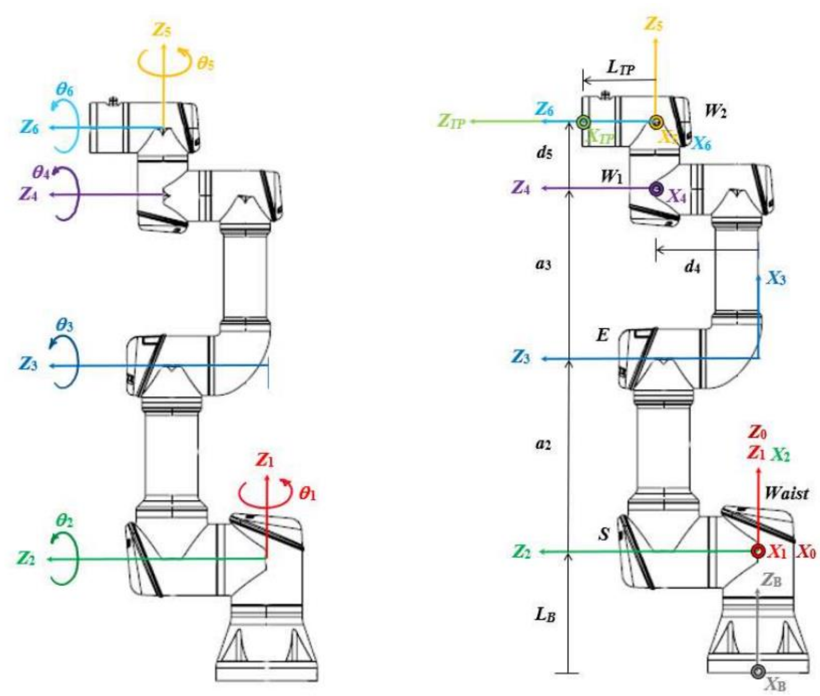

Figure A.1: Diagram of the 6 DoF Universal URe-Series Kinematic with Coordinate Frames (Robert L. Williams II, 2024)

The modified Denavit-Hartenberg parameters are presented in this table for the *UR3e*.

Table A.1: DH Parameters of the 6 DoF Universal Robot URe-Series

i	α_{i-1}	a_{i-1}	d_i	θ_i
1	0	0	0	θ_1
2	90	0	0	θ_2+ 90
3	0	a_2	0	θ_3
4	0	a_3	d_4	θ_4 -90
5	-90	0	d_5	θ_5
6	90	0	0	θ_6

Where Specific DH Lengths in the *UR3e* (mm):
LB=152, a_2=244, a_3=213, d_4=131,d_5=85, LTP=92

A.2. The *UR3e* Cobot forward kinematics

The forward kinematics problem for a robot is to calculate the pose (position and orientation) of the end-effector frame of interest given the joint values. For serial-chain robots, the forward kinematics problem set up and solution is based on substituting each line of the Denavit-Hartenberg parameters table (Table A.1) into the equation below, which gives the pose of frame {i} with respect to its nearest neighbor frame {i–1} back along the serial chain:

$$ {}^{i-1}_{i}T = \begin{bmatrix} c\theta_i & -s\theta_i & 0 & a_{i-1} \\ s\theta_i c\alpha_{i-1} & c\theta_i c\alpha_{i-1} & -s\alpha_{i-1} & -d_i\alpha_{i-1} \\ s\theta_i s\alpha_{i-1} & c\theta_i s\alpha_{i-1} & c\alpha_{i-1} & d_i\alpha_{i-1} \\ 0 & 0 & 0 & 1 \end{bmatrix} = \begin{bmatrix} & {}^{i-1}_{i}R & & {}^{i-1}_{i}P \\ 0 & 0 & 0 & 1 \end{bmatrix} $$

Where the following abbreviations were used:

$$c\theta_i = \cos(\theta_i),\ s\theta_i = \sin(\theta_i),\ c\alpha_{i-1} = \cos(\alpha_{i-1}) \text{ and } s\alpha_{i-1} = \sin(\alpha_{i-1}).$$

The equation above represents pose (position and orientation) of frame {i} with respect to frame {i–1} by using a 4x4 homogeneous transformation matrix. The upper left 3x3 matrix is

the rotation matrix $\left[{}^{i-1}_{i}R\right]$ giving the orientation of frame {i} with respect to frame {i–1}, expressed in {i–1} coordinates. The upper right 3x1 vector $\left\{{}^{i-1}_{i}P\right\}$ is the position vector from the origin of {i–1} to the origin of {i}, expressed in { i–1} coordinates.
Then homogeneous transformation equations are used to find the pose of the overall end-effector frame of interest with respect to the base reference frame, to complete the FPK solution for each serial chain.

The statement of the FPK problem for the serial chain of the Universal Cobot URe-Series is:

Given($\theta_1, \theta_2, \theta_3, \theta_4, \theta_5, \theta_6$) , calculate ${}^{6}_{0}T$ and ${}^{B}_{TP}T$. where $\theta_1, \theta_2, \theta_3, \theta_4, \theta_5, \theta_6$ are the six joint angles, {TP} is the tool-plate frame and {B} is the fixed robot base reference frame.

$$ {}^{0}_{1}T = \begin{bmatrix} c_1 & -s_1 & 0 & 0 \\ s_1 & c_1 & 0 & 0 \\ 0 & 0 & 1 & 0 \\ 0 & 0 & 0 & 1 \end{bmatrix} $$

$$ {}^{1}_{2}T = \begin{bmatrix} -s_2 & -c_2 & 0 & 0 \\ 0 & 0 & -1 & 0 \\ c_2 & -s_2 & 0 & 0 \\ 0 & 0 & 0 & 1 \end{bmatrix} $$

$$ {}^{2}_{3}T = \begin{bmatrix} c_3 & -s_3 & 0 & a_2 \\ s_3 & c_3 & 0 & 0 \\ 0 & 0 & 1 & 0 \\ 0 & 0 & 0 & 1 \end{bmatrix} $$

$$ {}^{3}_{4}T = \begin{bmatrix} s_4 & c_4 & 0 & a_3 \\ -c_4 & s_4 & 0 & 0 \\ 0 & 0 & 1 & d_4 \\ 0 & 0 & 0 & 1 \end{bmatrix} $$

$$ {}^{4}_{5}T = \begin{bmatrix} c_5 & -s_5 & 0 & 0 \\ 0 & 0 & 1 & d_5 \\ -s_5 & -c_5 & 0 & 0 \\ 0 & 0 & 0 & 1 \end{bmatrix} $$

$$ {}^{5}_{6}T = \begin{bmatrix} c_6 & -s_6 & 0 & 0 \\ 0 & 0 & -1 & 0 \\ s_6 & c_6 & 0 & 0 \\ 0 & 0 & 0 & 1 \end{bmatrix} $$

$$ {}^{0}_{6}T(\theta_1,\theta_2\ ,\theta_3\ ,\theta_4,\theta_5,\theta_6)] = [{}^{0}_{1}T(\theta_1)][{}^{1}_{2}T(\theta_2)][\ {}^{2}_{3}T(\theta_3)][{}^{3}_{4}T(\theta_4)][{}^{4}_{5}T(\theta_5)][{}^{5}_{6}T(\theta_6)] $$

$$ [{}^{0}_{6}T(\theta_1,\theta_2\ ,\theta_3\ ,\theta_4,\theta_5,\theta_6)] = \begin{bmatrix} r_{11} & r_{12} & r_{13} & {}^{0}_{6}x \\ r_{21} & r_{22} & r_{23} & {}^{0}_{6}y \\ r_{31} & r_{32} & r_{33} & {}^{0}_{6}z \\ 0 & 0 & 0 & 1 \end{bmatrix} $$

The orthonormal rotation matrix elements for this FPK result are:

$$ r_{11} = -s_1 s_5 c_6 + c_1(-s_{234} s_6 + c_{234} c_5 c_6) $$

$$ r_{21} = c_1 s_5 c_6 + s_1(-s_{234} s_6 + c_{234} c_5 c_6) $$

$$ r_{31} = c_{234} s_6 + s_{234} c_5 c_6 $$

$$ r_{12} = s_1 s_5 s_6 - c_1(s_{234} c_6 + c_{234} c_5 s_6) $$

$$ r_{22} = -c_1 s_5 s_6 - s_1(s_{234} c_6 + c_{234} c_5 s_6) $$

$$ r_{32} = c_{234} c_6 - s_{234} c_5 s_6 $$

$$ r_{13} = s_1 c_5 + c_1 c_{234} s_5 $$

$$ r_{23} = -c_1 c_5 + s_1 c_{234} s_5 $$

$$ r_{33} = s_{234} s_5 $$

$$ {}^{0}_{6}x = d_4 s_1 - c_1(a_2 s_2 + a_3 s_{23} + d_5 s_{234}) $$

$$ {}^{0}_{6}y = -d_4 c_1 - s_1(a_2 s_2 + a_3 s_{23} + d_5 s_{234}) $$

$$ {}^{0}_{6}z = a_2 c_2 + a_3 c_{23} + d_5 c_{234} $$

$$ \{{}^{6}_{0}P\} = \begin{Bmatrix} {}^{0}_{6}x \\ {}^{0}_{6}y \\ {}^{0}_{6}z \end{Bmatrix} $$

Additional, Fixed Transforms – Tool-Plate and Base Coordinate Frames

To complete the FPK solution we need to include the Cartesian coordinate frames {TP} and {B} to find ${}^{B}_{TP}T$:

$$ [{}^{B}_{TP}T] = [{}^{B}_{0}T(L_B)][{}^{0}_{6}T(\theta_1,\theta_2\ ,\theta_3\ ,\theta_4,\theta_5,\theta_6)][{}^{6}_{TP}T(L_{TP})] $$

Where L_B and L_{TP} are known constants.

$$ {}_{0}^{B}T = \begin{bmatrix} 1 & 0 & 0 & 0 \\ 0 & 1 & 0 & 0 \\ 0 & 0 & 1 & L_B \\ 0 & 0 & 0 & 1 \end{bmatrix} $$

$$ {}_{TP}^{6}T = \begin{bmatrix} 1 & 0 & 0 & 0 \\ 0 & 1 & 0 & 0 \\ 0 & 0 & 1 & L_{TP} \\ 0 & 0 & 0 & 1 \end{bmatrix} $$

Note the origin of {TP} is now a function of $(\theta_1, \theta_2, \theta_3, \theta_4, \theta_5, \theta_6)$ but it is still not a function of θ_6 since the last Z_6 R-joint axis passes through the origin of $\{6\}$. Of course, the position of a general tool held in a gripper attached to the tool-plate would be a function of all six joint angles $(\theta_1, \theta_2, \theta_3, \theta_4, \theta_5, \theta_6)$.

The reader can see (J. Diab, Fonte, Poisson, & Novales, 2020; Robert L. Williams II, 2024; Ullah, Ajwad, Islam, Iqbal, & Iqbal, 2014) and (Kufieta, 2014) for more informations and details regarding the Universal Robot manipulator modelling.

APPENDIX B: Phantom OMNI haptic device

Geomagic Touch formerly produced by the *3D Systems* company as Phantom OMNI, is a haptic device that allows users to interact with virtual environments using force feedback. It's presented in the following figure.

(a)

(b)

Figure B.1: The *Phantom OMNI* haptic device

The device is equipped with a 6D joystick, three buttons, and motors for force feedback, allowing operators to control gripper's fingers and robotic arm, and an "inkwell button" for device usage. All the degrees of motion have physical limits. When the user reaches one of these limits he will feel a sudden stop; this is the mechanical stop designed into the device.

The number of degrees of freedom of the device coincides with the number of degrees of freedom of the manipulator and easily accessible buttons, which, makes Phantom OMNI a good choice for working with the 6DoF Universal Robot arms. The arm of the device can be move left/right (see Fig B.1). The body of the Phantom OMNI device will pivot until it reaches a physical limit. The stylus can be move up/down and in/out.

It is also worth noting that Phantom OMNI is relatively compact, so both devices can be easily placed on the desk of operator's workstation.

The tactile device comes with software that allows calibrating and tuning, both in Windows and Linux Operation Systems (OS).

The Phantom OMNI device communicates with the computer through the FireWire port. To enable this, a software driver, called the Phantom Device Drivers (PDD) needs to be installed, to control the communication. Specific instructions for installing the PDD can be found in the Phantom Device Driver Installation Guide. In our research, we used a PCI-FireWire card to enable this connection.

Specifications of Geomagic Touch are presented in Table B.1.

Table B.1: The *Phanotm OMNI* haptic device specifications

Workspace dimensions	160 mm x 120 mm x 70 mm
Resolution	0.055 mm (450 dpi)
Maximum force and torque at nominal position	3.3 N
Stiffness	x-axis > 1.26 N/mm y-axis > 2.31 N/mm z-axis > 1.02 N/mm
Number of buttons	2 on the joystick 1 inside the inkwell socket
Force feedback (6 Degrees of Freedom)	x,y,z
Position sensing/input (6 Degrees of Freedom) [Stylus gimbal]	x, y, z (digital encoders) [Roll, pitch, yaw (± 5% linearity potentiometers)]
Interface	RJ45 Compliant Ethernet Port

The reader can find more detailes about the Phantom OMNI haptic device in (3DSystems, 2024; fsuarez6, 2013/2023; Geomagic, Inc, 2013).

APPENDIX C: Robot Operating System (ROS)

This appendix provides information about the Robot Operating System (ROS), which is used to implement the methods presented in this thesis on the real robots.

C.1. Introduction to ROS

Robots perform complex tasks using sensors, actuators, and a computing unit that processes sensor data and controls movements. To manage these functions efficiently, a Robot Operating System (ROS) is necessary. ROS coordinates multiple processes, ensures smooth data exchange, and supports modular, reusable code. It simplifies development by offering high-level programming tools, community support, and integration with third-party libraries. This makes ROS ideal for creating advanced robotic systems capable of tasks like navigation, manipulation, and vision processing.

ROS is a free, open-source robotics software framework which provides essential capabilities such as interprocess communication, multithreading, low-level device control, package management, and hardware abstraction. It supports popular programming languages like C++ and Python. ROS integrates with third-party libraries like OpenCV and includes off-the-shelf algorithms for tasks like PID control and SLAM. It has a strong community support and tools, such as Rviz for visualization and Gazebo for simulation which makes it indispensable for developing robotic systems.

C.2. ROS Architecture and Concepts

ROS is a framework to communicate between two programs or process. For example, data can be sent/received between two programs using ROS.

In Fig C.1, ROS simplifies communication between programs (nodes), ideal for systems with multiple sensors and actuators. It manages this efficiently by allowing nodes to exchange data through a central ROS Master. ROS breaks this down by enabling nodes to handle specific tasks and communicate through topics, reducing complexity in robotic systems with many components.

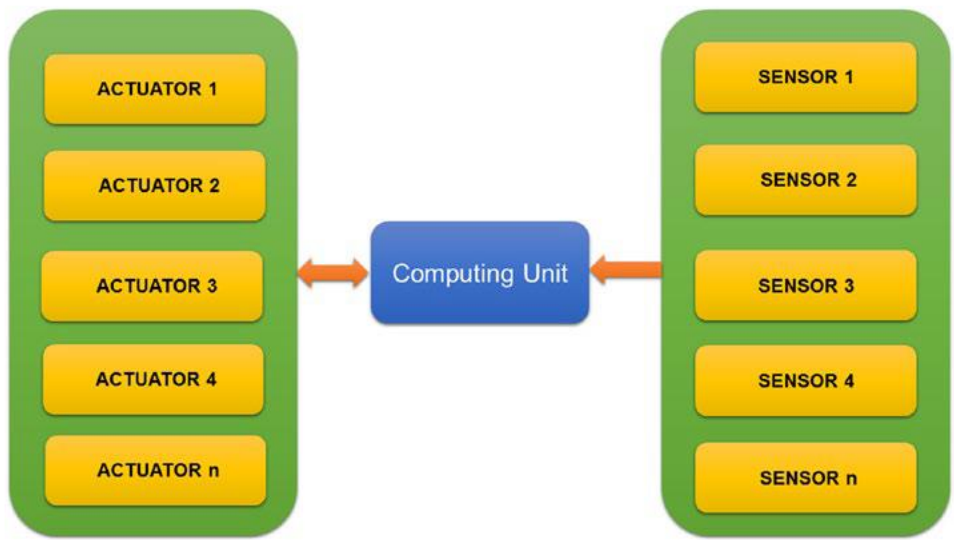

Figure C.1: Typical robot block with actuators and sensors

Let's see how the communication is happening between two programs in ROS. Fig C.2 illustrates a basic block diagram of ROS.

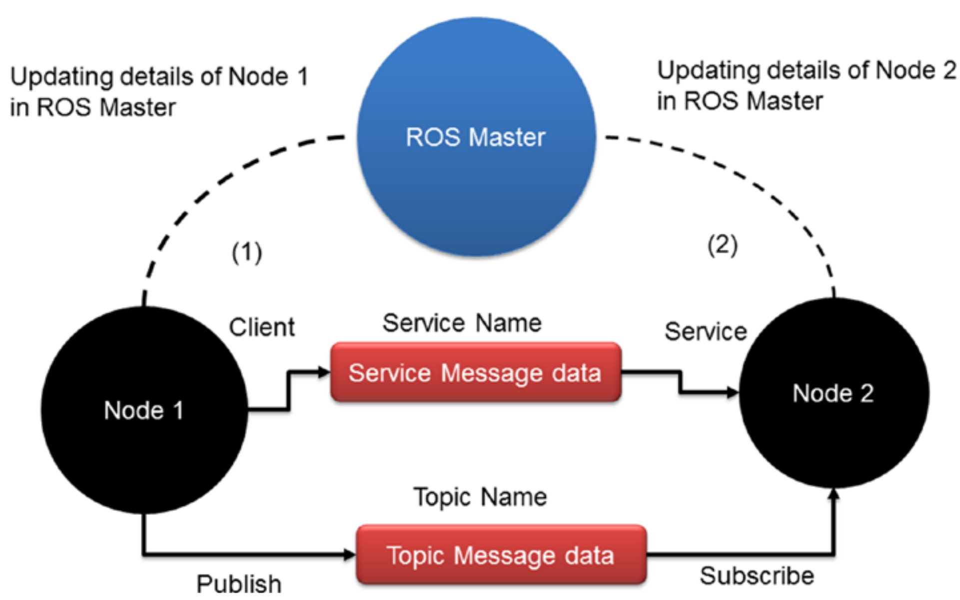

Figure C.2: ROS Communication block diagram

Fig C.2 shows two programs marked as node 1 and node 2. When any of the programs start, a node communicates to a ROS program called the ROS master. The node sends all its information to the ROS master, including the type of data it sends or receives. The nodes that are sending a data are called publisher nodes, and the nodes that are receiving data are called subscriber nodes. The ROS Master has all the publisher and subscriber information running on computers. If node 1 sends some data and the same data is required by node 2, then the ROS master sends the information to the nodes so that they can communicate with each other.

These data, also called ROS messages, can be from different types, which includes integer, float, string, and so forth. With ROS messages, we can send data with a single data type or multiple data with different data types. They are sent through a message bus or path called ROS topic. When a ROS node publishes a topic, it sends a ROS topic with a ROS message, and it has data with the message type.

In Fig C.2, the ROS topic is publishing and subscribing node 1 and node 2. This process starts when the ROS master exchange the node details to each other.

C.3. The ROS file system and computation concepts

The ROS file system includes packages, meta packages, package manifests, repositories, message types, and services types.

- **ROS packages**: the fundamental unit of organization in ROS, containing all the files necessary for ROS software. This includes source code, data files, dependencies, and build configurations.
- **ROS meta-packages**: a collection of related ROS packages. It doesn't contain source or data files but lists dependencies on related packages.
- **Package manifest**: an XML file in each ROS package that contains essential information like the package name, description, authorship, dependencies, etc.
- **ROS repositories**: a version-controlled collection of ROS packages often shares a common purpose and are tracked together in a version control system like Git.
- **Message types**: custom-defined message formats used for communication between ROS nodes. These messages are stored in the msg folder of a package.
- **Service types**: like message types but focused on request-response interactions between nodes. They are stored in the srv folder of a package.

These are the terms associated with ROS computation concepts.

- **ROS nodes**: independent processes that perform computations using ROS APIs. Each node can communicate with other nodes in a distributed ROS network.
- **ROS master**: acts as the intermediary for communication, helping nodes find each other and facilitating message exchanges across the system.
- **ROS parameter server:** works alongside the ROS master to store and manage global or node-specific parameters. These parameters can be public (accessible by all nodes) or private (accessible only by specific nodes).
- **ROS topics**: named communication channels through which nodes exchange messages. They can either publish to a topic (sending data) or subscribe to it (receiving data).
- **ROS messages**: data packets that are transmitted through topics. ROS provides built-in message types based on primitive data types, but the user can also define his own message formats.
- **ROS services**: a request/reply communication mechanism where a client node sends a request and the server node responds. They provide synchronous communication, unlike topics, which are asynchronous.
- **ROS bags**: files used for recording and playing back ROS message exchanges on topics which is useful for logging and later analysis of data.

The reader can find more informations about the Robot Operating System ROS in (Joseph, 2018; Stasse, n.d.; Wiki ROS, 2024).

REFERENCES

3DSystems. (2024). Haptic Device Guides. Retrieved 21 June 2024, from https://support.3dsystems.com/s/article/Haptic-Device-Guides?language=en_US

Aguilar, I. H., & Sidobre, D. (2006). On-line trajectory planning of robot manipulator ’ s end effector in Cartesian Space using quaternions. *Contract*.

Aracil, R., Sánchez, F. M., García, D., González, J. M., Jiménez, L. M., & Sebastián, J. M. (1998). Obstacle Avoidance for Teleoperated Robots for Live Power Lines Maintenance, Using Artificial Vision. *IFAC Proceedings Volumes*, *31*(2), 327–332. https://doi.org/10.1016/S1474-6670(17)44218-2

Askarzadeh, F., Pahlavan, K., Geng, Y., Makarov, S. N., Ye, Y., & Khan, U. (2017). Modeling the Effect of Human Body on ToA Ranging Using Ray Theory. *International Journal of Wireless Information Networks*, *24*(2), 140–152. https://doi.org/10.1007/s10776-017-0336-5

Bassit, L. A., Poisson, G., & Vieyres, P. (2003). *Kinematics of a dedicated 6DOF Robot for Tele-echography*. Retrieved from https://www.semanticscholar.org/paper/Kinematics-of-a-dedicated-6DOF-Robot-for-Bassit-Poisson/941000c88d52b8cedc5871bf6421e63ba945e69b?sort=relevance&citationIntent=methodology

Beer, J. M., Fisk, A. D., & Rogers, W. A. (2014). Toward a Framework for Levels of Robot Autonomy in Human-Robot Interaction. *Journal of Human-Robot Interaction*, *3*(2), 74. https://doi.org/10.5898/JHRI.3.2.Beer

Bharatheesha, M., Hernandez, C., Wisse, M., Dumonteil, G., Bat, M., & Giftsun, N. (2017). *Dynamic Obstacle Avoidance for Collaborative Robot Applications*.

Boas, F. E., & Fleischmann, D. (2012). CT artifacts: Causes and reduction techniques. *Imaging in Medicine*, *4*(2), 229–240. https://doi.org/10.2217/iim.12.13

Campa, R., & Camarillo, K. (2008). Unit Quaternions: A Mathematical Tool for Modeling, Path Planning and Control of Robot Manipulators. In *Robot Manipulators*. https://doi.org/10.5772/6197

Ceriani, N. M., Zanchettin, A. M., Rocco, P., Stolt, A., & Robertsson, A. (2015). Reactive Task Adaptation Based on Hierarchical Constraints Classification for Safe Industrial Robots. *IEEE/ASME Transactions on Mechatronics*, *20*(6), 2935–2949. https://doi.org/10.1109/TMECH.2015.2415462

Chemweno, P., Pintelon, L., & Decre, W. (2020). Orienting safety assurance with outcomes of hazard analysis and risk assessment: A review of the ISO 15066 standard for collaborative robot systems. *Safety Science*, *129*, 104832. https://doi.org/10.1016/j.ssci.2020.104832

Chittawadigi, R. G., & Saha, S. K. (2013). An analytical method to detect collision between cylinders using dual number algebra. *IEEE International Conference on Intelligent Robots and Systems*, 5353–5358. https://doi.org/10.1109/IROS.2013.6697131

Chotiprayanakul, P., Liu, D. K., Wang, D., & Dissanayake, G. (2007). A 3-dimensional force field method for robot collision avoidance in complex environments. *Automation and Robotics in Construction - Proceedings of the 24th International Symposium on Automation and Robotics in Construction*, (September 2007), 139–145. https://doi.org/10.22260/isarc2007/0026

Colgate, J. E., Wannasuphoprasit, W., & Peshkin, M. A. (1996). *COBOTS: ROBOTS FOR COLLABORATION WITH HUMAN OPERATORS*.

Courrèges, F., Novales, C., Poisson, G., & Vieyres, P. (2009). Modélisation, commande géométrique et utilisation d'un robot portable de télééchographie: Teresa. *Journal Européen Des Systèmes Automatisés (JESA)*, *43*(n°1-2), pp 165-195. https://doi.org/10.3166/jesa.43.165-195

Dance, D. R., Christofides, S., Maidment, A. D.A., McLean, I. D., & Ng, K. H. (2014). *Diagnostic Radiology Physics: A Handbook for Teachers and Students*.

Denavit, J., & Hartenberg, R. S. (1955). A Kinematic Notation for Lower-Pair Mechanisms Based on Matrices. *Journal of Applied Mechanics*, *22*(2), 215–221. https://doi.org/10.1115/1.4011045

Di Mauro, E., Solbiati, M., De Beni, S., Forzoni, L., D'Onofrio, S., & Solbiati, L. (2013). Virtual navigator real-time ultrasound fusion imaging with positron emission tomography for liver interventions. *2013 35th Annual International Conference of the IEEE Engineering in Medicine and Biology Society (EMBC)*, 1406–1409. Osaka: IEEE. https://doi.org/10.1109/EMBC.2013.6609773

DIAB, J. (2021). *Hybrid robotic control by teleoperation and comanipulation: Application to ultrasound probe positioning in a constrained environment* (Orléans). Orléans, Orléans, France. Retrieved from https://www.theses.fr/2021ORLE3144

Diab, J., Fonte, A., Poisson, G., & Novales, C. (2020). PHRI safety control using a virtual flexible joint approach. *ICINCO 2020 - Proceedings of the 17th International Conference on Informatics in Control, Automation and Robotics*, (Icinco), 262–271. https://doi.org/10.5220/0009777702620271

Diab, Joseph. (2021). *Commande robotique hybride par téléopération et comanipulation: Application au positionnement d'une sonde échographique en milieu contraint* (These de doctorat, Orléans). Orléans. Retrieved from https://www.theses.fr/2021ORLE3144

Dietrich, A., Wimbock, T., & Albu-Schaffer, A. (2011). *Dynamic Whole-Body Mobile Manipulation with a Torque Controlled Humanoid Robot via Impedance Control Laws*.

Dietrich, A., Wimbock, T., Taubig, H., Albu-Schaffer, A., & Hirzinger, G. (2011). Extensions to reactive self-collision avoidance for torque and position controlled humanoids. *2011 IEEE International Conference on Robotics and Automation*, 3455–3462. Shanghai, China: IEEE. https://doi.org/10.1109/ICRA.2011.5979862

Elahres, M., Fonte, A., & Poisson, G. (2021). Evaluation of an Artificial Potential Field Method in Collision-free Path Planning for a Robot Manipulator: *Proceedings of the 2nd International Conference on Robotics, Computer Vision and Intelligent*

Systems, 92–102. Online Streaming, --- Select a Country ---: SCITEPRESS - Science and Technology Publications. https://doi.org/10.5220/0010652800003061

Faragallah, O. S., El-Hoseny, H., El-Shafai, W., El-Rahman, W. A., El-Sayed, H. S., El-Rabaie, E.-S. M., … Geweid, G. G. N. (2021). A Comprehensive Survey Analysis for Present Solutions of Medical Image Fusion and Future Directions. *IEEE Access*, *9*, 11358–11371. https://doi.org/10.1109/ACCESS.2020.3048315

Farsoni, S., Rizzi, J., Ufondu, G. N., & Bonfè, M. (2022). Planning Collision-Free Robot Motions in a Human–Robot Shared Workspace via Mixed Reality and Sensor-Fusion Skeleton Tracking. *Electronics*, *11*(15), 2407. https://doi.org/10.3390/electronics11152407

Faverjon, B., & Tournassoud, P. (1987). A local based approach for path planning of manipulators with a high number of degrees of freedom. *Proceedings. 1987 IEEE International Conference on Robotics and Automation*, *4*, 1152–1159. Raleigh, NC, USA: Institute of Electrical and Electronics Engineers. https://doi.org/10.1109/ROBOT.1987.1087982

Feddema, J. T., & Novak, J. L. (1994). Whole arm obstacle avoidance for teleoperated robots. *Proceedings of the 1994 IEEE International Conference on Robotics and Automation*, 3303–3309. San Diego, CA, USA: IEEE Comput. Soc. Press. https://doi.org/10.1109/ROBOT.1994.351062

Flacco, F., Kroger, T., De Luca, A., & Khatib, O. (2012). A depth space approach to human-robot collision avoidance. *2012 IEEE International Conference on*

Robotics and Automation, 338–345. Saint Paul, MN: IEEE. https://doi.org/10.1109/ICRA.2012.6225245

Fonte, A., Essomba, T., Vieyres, P., Canou, J., Fraisse, P., Zeghloul, S., … Arbeille, P. (2010). *Robotic Platform for an Interactive Tele-echographic System: The PROSIT ANR-2008 project*.

fsuarez6. (2023). *Fsuarez6/phantom_omni* [C++]. Retrieved from https://github.com/fsuarez6/phantom_omni (Original work published 2013)

Garcia-Hernandez, N., & Parra-Vega, V. (2009). Haptic Teleoperated Robotic System for an Effective Obstacle Avoidance. *2009 Second International Conferences on Advances in Computer-Human Interactions*, 255–260. Cancun, Mexico: IEEE. https://doi.org/10.1109/ACHI.2009.36

Gasparetto, A., Boscariol, P., Lanzutti, A., & Vidoni, R. (2015a). Path Planning and Trajectory Planning Algorithms: A General Overview. In G. Carbone & F. Gomez-Bravo (Eds.), *Motion and Operation Planning of Robotic Systems* (pp. 3–27). Cham: Springer International Publishing. https://doi.org/10.1007/978-3-319-14705-5_1

Gasparetto, A., Boscariol, P., Lanzutti, A., & Vidoni, R. (2015b). Path planning and trajectory planning algorithms: A general overview. In *Mechanisms and Machine Science* (Vol. 29, pp. 3–27). https://doi.org/10.1007/978-3-319-14705-5_1

Geomagic, Inc. (2013). *Omni Device Guide*. Retrieved from www.geomagic.com

Gervasi, R., Mastrogiacomo, L., & Franceschini, F. (2020). A conceptual framework to evaluate human-robot collaboration. *The International Journal of Advanced*

Manufacturing Technology, *108*(3), 841–865. https://doi.org/10.1007/s00170-020-05363-1

Giuliani, M., Szczęśniak-Stańczyk, D., Mirnig, N., Stollnberger, G., Szyszko, M., Stańczyk, B., & Tscheligi, M. (2020). User-centred design and evaluation of a tele-operated echocardiography robot. *Health and Technology*, *10*(3), 649–665. https://doi.org/10.1007/s12553-019-00399-0

Gourdon, A., Poignet, P., Poisson, G., Parmantier, Y., & Marche, P. (1999). Master slave robotic system for ultrasound scanning. *European Medical and Biological Engineering Conference*, *2*, 1116–1117.

Gourdon, A., Poignet, P., Poisson, G., Vieyres, P., & Marche, P. (1999). A new robotic mechanism for medical application. *1999 IEEE/ASME International Conference on Advanced Intelligent Mechatronics (Cat. No.99TH8399),* 33–38. Atlanta, GA, USA: IEEE. https://doi.org/10.1109/AIM.1999.803139

Guiochet, J., & Vilchis, A. (2002, October 10). *Safety Analysis of a Medical Robot for Tele-echography*. Retrieved from https://www.semanticscholar.org/paper/Safety-Analysis-of-a-Medical-Robot-for-Guiochet-Vilchis/b0efc0f0b5803f22048c8ca794a0a2a3935e9543

Guoxian, N., & Liang, L. (2020). Workspace Analysis and Dynamics Simulation of Manipulator based on MATLAB. *IOP Conference Series: Materials Science and Engineering*, *825*(1), 012001. https://doi.org/10.1088/1757-899X/825/1/012001

Hoeckelmann, M., Rudas, I. J., Fiorini, P., Kirchner, F., & Haidegger, T. (2015). Current Capabilities and Development Potential in Surgical Robotics. *International Journal of Advanced Robotic Systems*, *12*(5), 61. https://doi.org/10.5772/60133

Hong Liu, Xuezhi Deng, & Hongbin Zha. (2005). A planning method for safe interaction between human arms and robot manipulators. *2005 IEEE/RSJ International Conference on Intelligent Robots and Systems*, 2724–2730. Edmonton, Alta., Canada: IEEE. https://doi.org/10.1109/IROS.2005.1545241

Hoy, M., Matveev, A. S., & Savkin, A. V. (2015). Algorithms for collision-free navigation of mobile robots in complex cluttered environments: A survey. *Robotica*, *33*(3), 463–497. https://doi.org/10.1017/S0263574714000289

Huang, P.-C., & Jeng, S.-K. (2012). Human body pose recognition from a single-view depth camera. *2012 IEEE International Conference on Systems, Man, and Cybernetics (SMC)*, 2144–2149. Seoul, Korea (South): IEEE. https://doi.org/10.1109/ICSMC.2012.6378057

Iqbal, J., Islam, R. U., Abbas, S. Z., Khan, A. A., & Ajwad, S. A. (2016). Automatzacija industrijskih poslova kroz mehatronicke sustave—Pregled robotike iz industrijske perspektive. *Tehnicki Vjesnik*, *23*(3), 917–924. https://doi.org/10.17559/TV-20140724220401

Jiang, Chalich, & Deen. (2019). Sensors for Positron Emission Tomography Applications. *Sensors*, *19*(22), 5019. https://doi.org/10.3390/s19225019

Jiang, S., Fang, H., He, K., & Yan, C. (2018). Research on obstacle avoidance path planning algorithm for six-axis robot. *2018 IEEE International Conference on*

Information and Automation, ICIA 2018, (August), 465–469. IEEE. https://doi.org/10.1109/ICInfA.2018.8812545

Joseph, L. (2018). *Robot Operating System for Absolute Beginners*. Berkeley, CA: Apress. https://doi.org/10.1007/978-1-4842-3405-1

Kavraki, L. E., & LaValle, S. M. (2008). Motion Planning. In B. Siciliano & O. Khatib (Eds.), *Springer Handbook of Robotics* (pp. 109–131). Berlin, Heidelberg: Springer. https://doi.org/10.1007/978-3-540-30301-5_6

Ketchel, J., & Larochelle, P. (2006). Collision detection of cylindrical rigid bodies for motion planning. *Proceedings - IEEE International Conference on Robotics and Automation*, *2006*(May), 1530–1535. https://doi.org/10.1109/ROBOT.2006.1641925

Ketchel, J. S., & Larochelle, P. M. (2005). Collision detection of cylindrical rigid bodies using line geometry. *Proceedings of the ASME International Design Engineering Technical Conferences and Computers and Information in Engineering Conference - DETC2005*, *7 B*, 811–825. https://doi.org/10.1115/detc2005-84699

Khalil, W., & Kleinfinger, J. (1986). A new geometric notation for open and closed-loop robots. *1986 IEEE International Conference on Robotics and Automation Proceedings*, *3*, 1174–1179. https://doi.org/10.1109/ROBOT.1986.1087552

Khatib, O. (1985). Real-time obstacle avoidance for manipulators and mobile robots. *Proceedings. 1985 IEEE International Conference on Robotics and Automation*, *2*, 500–505. Institute of Electrical and Electronics Engineers. https://doi.org/10.1109/ROBOT.1985.1087247

Khatib, Oussama. (1986). The Potential Field Approach And Operational Space Formulation In Robot Control. In K. S. Narendra (Ed.), *Adaptive and Learning Systems* (pp. 367–377). Boston, MA: Springer US. https://doi.org/10.1007/978-1-4757-1895-9_26

Kivelä, T., Mattila, J., Puura, J., & Launis, S. (2017). On-line path planning with collision avoidance for coordinate-controlled robotic manipulators. *ASME/BATH 2017 Symposium on Fluid Power and Motion Control, FPMC 2017*, 1–10. American Society of Mechanical Engineers. https://doi.org/10.1115/FPMC2017-4297

Kufieta, K. (2014). *Force Estimation in Robotic Manipulators: Modeling, Simulation and Experiments*. 144.

Kwee, H. H., Tramblay, M., Barbier, R., Dupeyroux, M., Vinceneux, M. F., Semoulin, P., & Pannier, S. (1983). First experimentation of the Spartacus telethesis in a clinical environment. *Spinal Cord*, *21*(5), 275–286. https://doi.org/10.1038/sc.1983.47

Lacevic, B., Rocco, P., & Zanchettin, A. M. (2013). Safety Assessment and Control of Robotic Manipulators Using Danger Field. *IEEE Transactions on Robotics*, *29*(5), 1257–1270. https://doi.org/10.1109/TRO.2013.2271097

Lajpah, L., & Petri, T. (2012). Obstacle Avoidance for Redundant Manipulators as Control Problem. In S. Kucuk (Ed.), *Serial and Parallel Robot Manipulators—Kinematics, Dynamics, Control and Optimization*. InTech. https://doi.org/10.5772/32651 lajpah, L., & Petri, T. (2012). Obstacle Avoidance for Redundant Manipulators as Control Problem. In *Serial and Parallel Robot Manipulators—Kinematics, Dynamics, Control and Optimization*. https://doi.org/10.5772/32651

Lameka, K., Farwell, M. D., & Ichise, M. (2016). Positron Emission Tomography. In *Handbook of Clinical Neurology* (Vol. 135, pp. 209–227). Elsevier. https://doi.org/10.1016/B978-0-444-53485-9.00011-8

Leeper, A., Hsiao, K., Ciocarlie, M., Sucan, I., & Salisbury, K. (2013). Methods for collision-free arm teleoperation in clutter using constraints from 3D sensor data. *2013 13th IEEE-RAS International Conference on Humanoid Robots (Humanoids)*, 520–527. Atlanta, GA: IEEE. https://doi.org/10.1109/HUMANOIDS.2013.7030023

Li, X., Song, A., Li, H., Lu, W., & Mao, C. (2012). Real-Time Obstacle Avoidance for Telerobotic Systems Based on Equipotential Surface. *International Journal of Advanced Robotic Systems*, *9*(3), 71. https://doi.org/10.5772/50652

Liu, S., & Liu, P. (2020, November 15). A Review of Motion Planning Algorithms for Robotic Arm Systems [Proceedings Paper]. Retrieved 27 September 2024, from 8th International Conference on Robot Intelligence Technology and Applications (proceedings) website: https://eprints.whiterose.ac.uk/168146/

Lynch, K. M., & Park, F. C. (2017). *Modern robotics: Mechanics, planning, and control*. Cambridge: Cambridge university press.

Magazine, S., & Novak, M. (2012). Telemedicine Predicted in 1925. Retrieved 24 November 2023, from Smithsonian Magazine website:

https://www.smithsonianmag.com/history/telemedicine-predicted-in-1925-124140942/

Matúšová, M., Bučányová, M., & Hrušková, E. (2019). The future of industry with collaborative robots. *MATEC Web of Conferences*, *299*, 02008. https://doi.org/10.1051/matecconf/201929902008

Michael, S. (2010). ¨ *ERLANGEN-N URNBERG FRIEDRICH-ALEXANDER-UNIVERSIT AT Lehrstuhl f ¨ ur Informatik 10 (Systemsimulation) Collision Detection for Cylinder-Shaped Rigid Bodies*. *10*.

Mihelj, M., Bajd, T., Ude, A., Lenarčič, J., Stanovnik, A., Munih, M., … Šlajpah, S. (2019). Collaborative Robots. In M. Mihelj, T. Bajd, A. Ude, J. Lenarčič, A. Stanovnik, M. Munih, … S. Šlajpah, *Robotics* (pp. 173–187). Cham: Springer International Publishing. https://doi.org/10.1007/978-3-319-72911-4_12

Omarali, B., Palermo, F., Valle, M., Poslad, S., Althoefer, K., & Farkhatdinov, I. (2019). Position and Velocity Control for Telemanipulation with Interoperability Protocol. In K. Althoefer, J. Konstantinova, & K. Zhang (Eds.), *Towards Autonomous Robotic Systems* (pp. 316–324). Cham: Springer International Publishing. https://doi.org/10.1007/978-3-030-23807-0_26

Paparo, F., Piccazzo, R., Cevasco, L., Piccardo, A., Pinna, F., Belli, F., … Rollandi, G. A. (2014). Advantages of percutaneous abdominal biopsy under PET-CT/ultrasound fusion imaging guidance: A pictorial essay. *Abdominal Imaging*, *39*(5), 1102–1113. https://doi.org/10.1007/s00261-014-0143-8

Park, C. (2015). *Self-Collision Detection & Avoidance Algorithm for a Robot Manipulator*. *5*(4).

Park, S. O., Lee, M. C., & Kim, J. (2020a). Trajectory Planning with Collision Avoidance for Redundant Robots Using Jacobian and Artificial Potential Field-based Real-time Inverse Kinematics. *International Journal of Control, Automation and Systems*, *18*(8), 2095–2107. https://doi.org/10.1007/s12555-019-0076-7

Park, S. O., Lee, M. C., & Kim, J. (2020b). Trajectory Planning with Collision Avoidance for Redundant Robots Using Jacobian and Artificial Potential Field-based Real-time Inverse Kinematics. *International Journal of Control, Automation and Systems*, *18*(8), 2095–2107. https://doi.org/10.1007/s12555-019-0076-7

Peng, G., Yang, J., Li, X., & Khyam, M. O. (2023). Deep Reinforcement Learning With a Stage Incentive Mechanism of Dense Reward for Robotic Trajectory Planning. *IEEE Transactions on Systems, Man, and Cybernetics: Systems*, *53*(6), 3566–3573. https://doi.org/10.1109/TSMC.2022.3228901

Perez-Liva, M., Viel, T., Yoganathan, T., Garofalakis, A., Sourdon, J., Facchin, C., … Tavitian, B. (2018). Performance evaluation of the PET component of a hybrid PET/CT-ultrafast ultrasound imaging instrument. *Physics in Medicine & Biology*, *63*(19), 19NT01. https://doi.org/10.1088/1361-6560/aad946

Perez-Liva, M., Yoganathan, T., Herraiz, J. L., Porée, J., Tanter, M., Balvay, D., … Tavitian, B. (2020). Ultrafast Ultrasound Imaging for Super-Resolution

Preclinical Cardiac PET. *Molecular Imaging and Biology*, *22*(5), 1342–1352. https://doi.org/10.1007/s11307-020-01512-w

Petrič, T., Gams, A., Likar, N., & Žlajpah, L. (2015a). Obstacle Avoidance with Industrial Robots. In G. Carbone & F. Gomez-Bravo (Eds.), *Motion and Operation Planning of Robotic Systems* (pp. 113–145). Cham: Springer International Publishing. https://doi.org/10.1007/978-3-319-14705-5_5

Petrič, T., Gams, A., Likar, N., & Žlajpah, L. (2015b). Obstacle avoidance with industrial robots. In *Mechanisms and Machine Science* (Vol. 29, pp. 113–145). https://doi.org/10.1007/978-3-319-14705-5_5

Pie, E. (2021, July 12). Unimate: D'un bras mécanique à une innovation sans précédent. Retrieved 12 July 2024, from Robot Magazine website: https://www.robot-magazine.fr/robot-unimate-revolution-industrielle/

Pimkin, A., Samoylenko, A., Antipina, N., Ovechkina, A., Golanov, A., Dalechina, A., & Belyaev, M. (2020). Multidomain CT Metal Artifacts Reduction Using Partial Convolution Based Inpainting. *2020 International Joint Conference on Neural Networks (IJCNN)*, 1–6. Glasgow, United Kingdom: IEEE. https://doi.org/10.1109/IJCNN48605.2020.9206625

Portillo-Velez, R. de J., Rodriguez-Angeles, A., & Cruz-Villar, C. A. (2009). *Whole-Arm obstacle avoidance for non similar redundant teleoperated robots*.

Provost, J., Garofalakis, A., Sourdon, J., Bouda, D., Berthon, B., Viel, T., … Tavitian, B. (2018). Simultaneous positron emission tomography and ultrafast ultrasound for hybrid molecular, anatomical and functional imaging. *Nature Biomedical Engineering*, *2*(2), 85–94. https://doi.org/10.1038/s41551-018-0188-z

Reddy, A. C. (2014). Difference Between Denavit—Hartenberg (D-H) Classical and Modified Conventions for Forward Kinematics of Robots With Case Study. *International Conference on Advanced Materials and Manufacturing Technologies (AMMT)*, (figure 1), 267–286.

Robert L. Williams II. (2024). *Universal Robot URe-Series Cobot Kinematics & Dynamics*. Mechanical Engineering, Ohio University. Retrieved from https://people.ohio.edu/williams/html/PDF/UniversalRobotKinematics.pdf

Roizenblatt, M., Edwards, T. L., & Gehlbach, P. L. (2018). Robot-assisted vitreoretinal surgery: Current perspectives. *Robotic Surgery: Research and Reviews*, *5*, 1–11. https://doi.org/10.2147/RSRR.S122301

Safadi, H. (2007). *Local Path Planning- Using Virtual Potential Field*.

Safeea, M., & Neto, P. (2018). *Human-Robot Collision Avoidance for Industrial Robots: A V-REP Based Solution*.

Safeea, M., Neto, P., & Béarée, R. (2019). A Quest Towards Safe Human Robot Collaboration. In K. Althoefer, J. Konstantinova, & K. Zhang (Eds.), *Towards Autonomous Robotic Systems* (pp. 493–495). Cham: Springer International Publishing. https://doi.org/10.1007/978-3-030-25332-5_48

Safeea, M., Neto, P., & Bearee, R. (2019). On-line collision avoidance for collaborative robot manipulators by adjusting off-line generated paths: An industrial use case.

Robotics and Autonomous Systems, *119*, 278–288. https://doi.org/10.1016/j.robot.2019.07.013

Sangiovanni, B., Rendiniello, A., Incremona, G. P., Ferrara, A., & Piastra, M. (2018). Deep Reinforcement Learning for Collision Avoidance of Robotic Manipulators. *2018 European Control Conference (ECC)*, 2063–2068. Limassol: IEEE. https://doi.org/10.23919/ECC.2018.8550363

Sheridan, T. B. (2016). Human–Robot Interaction: Status and Challenges. *Human Factors: The Journal of the Human Factors and Ergonomics Society*, *58*(4), 525–532. https://doi.org/10.1177/0018720816644364

Spong, M. W., Hutchinson, S., & Vidyasagar, M. (2006). Robot modeling and control. *IEEE Control Systems*, *26*(6), 113–115. https://doi.org/10.1109/MCS.2006.252815

Stasse, O. (n.d.). *Introduction à ROS*.

Sugiura, H., Gienger, M., Janssen, H., & Goerick, C. (2007). Real-time collision avoidance with whole body motion control for humanoid robots. *2007 IEEE/RSJ International Conference on Intelligent Robots and Systems*, 2053–2058. San Diego, CA, USA: IEEE. https://doi.org/10.1109/IROS.2007.4399062

Swerdlow, D. R., Cleary, K., Wilson, E., Azizi-Koutenaei, B., & Monfaredi, R. (2017). Robotic Arm–Assisted Sonography: Review of Technical Developments and Potential Clinical Applications. *American Journal of Roentgenology*, *208*(4), 733–738. https://doi.org/10.2214/AJR.16.16780

Szasz, T. (2016). *Advanced beamforming techniques in ultrasound imaging and the associated inverse problems*.

Tang, X., Zhou, H., & Xu, T. (2024). Obstacle avoidance path planning of 6-DOF robotic arm based on improved A* algorithm and artificial potential field method. *Robotica*, *42*(2), 457–481. https://doi.org/10.1017/S0263574723001546

Tanter, M., & Fink, M. (2014). Ultrafast imaging in biomedical ultrasound. *IEEE Transactions on Ultrasonics, Ferroelectrics, and Frequency Control*, *61*(1), 102–119. https://doi.org/10.1109/TUFFC.2014.2882

Taylor, R. H. (2006). A Perspective on Medical Robotics. *Proceedings of the IEEE*, *94*(9), 1652–1664. https://doi.org/10.1109/JPROC.2006.880669

TIMM SANTE. (2017). Télé échographie. Retrieved 17 October 2024, from TIMM, Télé imagerie médicale mobile website: https://timm-sante.com/equipements/equipements-tele-echographie/

Torres, L. G., Kuntz, A., Gilbert, H. B., Swaney, P. J., Hendrick, R. J., Webster, R. J., & Alterovitz, R. (2015). A motion planning approach to automatic obstacle avoidance during concentric tube robot teleoperation. *2015 IEEE International Conference on Robotics and Automation (ICRA)*, 2361–2367. Seattle, WA, USA: IEEE. https://doi.org/10.1109/ICRA.2015.7139513

Trafton, J. G., Schultz, A. C., Cassimatis, N. L., Hiatt, L. M., Perzanowski, D., Brock, D. P., … Adams, W. (2005). Communicating and Collaborating with Robotic Agents. In R. Sun (Ed.), *Cognition and Multi-Agent Interaction* (1st ed., pp. 252–

278). Cambridge University Press. https://doi.org/10.1017/CBO9780511610721.011

Troccaz, J., Berkelman, P., Cinquin, P., & Vilchis-Gonzales, A. (2002). Interactive robots for medical applications. In H. U. Lemke, K. Inamura, K. Doi, M. W. Vannier, A. G. Farman, & J. H. C. Reiber (Eds.), *CARS 2002 Computer Assisted Radiology and Surgery* (pp. 175–180). Berlin, Heidelberg: Springer Berlin Heidelberg. https://doi.org/10.1007/978-3-642-56168-9_29

Troccaz, J., Dagnino, G., & Yang, G.-Z. (2019). Frontiers of Medical Robotics: From Concept to Systems to Clinical Translation. *Annual Review of Biomedical Engineering*, *21*(1), 193–218. https://doi.org/10.1146/annurev-bioeng-060418-052502

Ullah, M. I., Ajwad, S. A., Islam, R. U., Iqbal, U., & Iqbal, J. (2014). Modeling and computed torque control of a 6 degree of freedom robotic arm. *2014 International Conference on Robotics and Emerging Allied Technologies in Engineering, iCREATE 2014 - Proceedings*, 133–138. https://doi.org/10.1109/iCREATE.2014.6828353

Universal Robots. (2020). Parameters for calculations of kinematics and dynamics. Retrieved 18 May 2021, from Universal Robots Web Page website: https://www.universal-robots.com/articles/ur-articles/parameters-for-calculations-of-kinematics-and-dynamics/

Vaillant, J., Kheddar, A., Audren, H., Keith, F., Brossette, S., Escande, A., … Kanehiro, F. (2016). Multi-contact vertical ladder climbing with an HRP-2 humanoid. *Autonomous Robots*, *40*(3), 561–580. https://doi.org/10.1007/s10514-016-9546-4

Vieyres, P, Novales, C., Rivas, R., Vilcahuaman, L., Sandoval, J., Clark, T., … Lefebvre, E. (2013). *The next challenge for WOrld wide Robotized Tele-Echography eXperiment (WORTEX 2012): From engineering success to healthcare delivery*.

Vieyres, Pierre, Poisson, G., Courrèges, F., Smith-Guerin, N., Novales, C., & Arbeille, P. (2006). A Tele-Operated Robotic System for Mobile Tele-Echography: The Otelo Project. In R. S. H. Istepanian, S. Laxminarayan, & C. S. Pattichis (Eds.), *M-Health: Emerging Mobile Health Systems* (pp. 461–473). Boston, MA: Springer US. https://doi.org/10.1007/0-387-26559-7_35

Vilchis, A., Masuda, K., Troccaz, J., & Cinquin, P. (2003). Robot-based tele-echography: The TER system. *Studies in Health Technology and Informatics*, *95*, 212–217.

Vilchis González, A. (2003). *Robotic tele-echography*.

Villalobos, J., Sanchez, I. Y., & Martell, F. (2022). Singularity Analysis and Complete Methods to Compute the Inverse Kinematics for a 6-DOF UR/TM-Type Robot. *Robotics*, *11*(6), 137. https://doi.org/10.3390/robotics11060137

Von Haxthausen, F., Böttger, S., Wulff, D., Hagenah, J., García-Vázquez, V., & Ipsen, S. (2021). Medical Robotics for Ultrasound Imaging: Current Systems and Future Trends. *Current Robotics Reports*, *2*(1), 55–71. https://doi.org/10.1007/s43154-020-00037-y

Wang, H., Qi, H., Xu, M., Tang, Y., Yao, J., Yan, X., & Li, M. (2014). Research on the Relationship between Classic Denavit-Hartenberg and Modified Denavit-Hartenberg. *2014 Seventh International Symposium on Computational Intelligence and Design*, 26–29. Hangzhou, China: IEEE. https://doi.org/10.1109/ISCID.2014.56

Wang, L., Lim, S., & Jr, M. (2002). *Hybrid of global path planning and local navigation implemented on a mobile robot in indoor environment* (p. 826). https://doi.org/10.1109/ISIC.2002.1157868

Wang, X., Yang, C., Ju, Z., Ma, H., & Fu, M. (2017). Robot manipulator self-identification for surrounding obstacle detection. *Multimedia Tools and Applications*, *76*(5), 6495–6520. https://doi.org/10.1007/s11042-016-3275-8

Wiki ROS. (2024). Documentation—ROS Wiki. Retrieved 21 June 2024, from https://wiki.ros.org/

Withers, P. J., Bouman, C., Carmignato, S., Cnudde, V., Grimaldi, D., Hagen, C. K., … Stock, S. R. (2021). X-ray computed tomography. *Nature Reviews Methods Primers*, *1*(1), 18. https://doi.org/10.1038/s43586-021-00015-4

Xiao, L., & Zhang, Y. (2016). Dynamic design, numerical solution and effective verification of acceleration-level obstacle-avoidance scheme for robot manipulators. *International Journal of Systems Science*, *47*(4), 932–945. https://doi.org/10.1080/00207721.2014.909971

Xiaoping Yun & Ko-Cheng Tan. (1997). A wall-following method for escaping local minima in potential field based motion planning. *1997 8th International*

Conference on Advanced Robotics. Proceedings. ICAR'97, 421–426. Monterey, CA, USA: IEEE. https://doi.org/10.1109/ICAR.1997.620216

Yang, G.-Z., Cambias, J., Cleary, K., Daimler, E., Drake, J., Dupont, P. E., … Taylor, R. H. (2017). Medical robotics—Regulatory, ethical, and legal considerations for increasing levels of autonomy. *Science Robotics*, *2*(4), eaam8638. https://doi.org/10.1126/scirobotics.aam8638

Zhang, Y., & Wang, J. (2004). Obstacle Avoidance for Kinematically Redundant Manipulators Using a Dual Neural Network. *IEEE Transactions on Systems, Man and Cybernetics, Part B (Cybernetics)*, *34*(1), 752–759. https://doi.org/10.1109/TSMCB.2003.811519

Zhong, N., & Hauser, K. (2022). *Attentiveness Map Estimation for Haptic Teleoperation of Mobile Robot Obstacle Avoidance and Approach*. https://doi.org/10.48550/ARXIV.2212.08742

Planification de mouvement basée sur le champ potentiel artificiel pour une échographie robotisée sûre : application à l'imagerie médicale multimodale

1. Introduction

L'échographie constitue une modalité d'imagerie médicale souple, non invasive, peu coûteuse, et offrant une visualisation en temps réel. Cependant, elle est fortement dépendante de l'expertise de l'opérateur, qui doit manipuler manuellement la sonde sur la surface du patient pour obtenir les vues désirées. Dans les contextes cliniques complexes, tels que ceux impliquant des dispositifs d'imagerie multimodale (comme les appareils combinés CT-PET), l'accès à la zone d'examen peut être restreint, rendant la manipulation de la sonde difficile, voire impossible.

C'est dans ce cadre que s'inscrit la présente recherche, qui vise à développer un système robotisé collaboratif capable de manipuler une sonde échographique de manière sécurisée dans un environnement d'imagerie confiné. Le projet est mené dans le cadre du dispositif c-PETRUS, un projet pluridisciplinaire coordonné par l'INSERM, visant à intégrer les modalités échographiques à l'environnement hybride CT-PET pour une imagerie plus complète et pertinente sur le plan clinique.

L'environnement d'imagerie CT-PET est caractérisé par des contraintes physiques et géométriques importantes : espace limité dans le portique, visibilité partielle, co-présence de personnel médical, et nécessité d'éviter tout contact non contrôlé avec le patient ou les appareils. Dans ce contexte, l'approche robotique retenue repose sur l'utilisation d'un bras collaboratif (UR3e) doté d'une stratégie de planification de mouvement fondée sur les champs de potentiel artificiels (Artificial Potential Field – APF). Le système inclut également une interface de téléopération haptique permettant à un opérateur de piloter la sonde à distance, tout en bénéficiant d'une assistance automatique pour éviter les collisions.

La thèse discute ainsi la conception, le développement, l'intégration et la validation expérimentale d'un tel système, avec une attention particulière portée à la modélisation des obstacles (en particulier anthropomorphes), à la sécurité de l'interaction homme-robot, et à la fluidité du pilotage dans un cadre de téléopération.

2. Objectifs de la recherche

L'objectif principal de cette thèse est de proposer une solution de planification de mouvement sécurisée pour un bras robotisé manipulant une sonde échographique dans un environnement médical contraint. Plus précisément, il s'agit de répondre aux besoins suivants :

- Permettre une échographie téléopérée dans un portique d'imagerie CT-PET, en garantissant l'absence de collision avec les parois ou les obstacles environnants.

- Protéger les acteurs humains (patient, soignants) présents dans la zone d'examen, à travers une modélisation efficace de leurs formes et postures.
- Maintenir une interaction fluide entre le robot et l'opérateur humain, en garantissant la transparence du système dans les zones dégagées et une assistance efficace dans les zones à risque.
- Évaluer expérimentalement la robustesse et la réactivité du système en conditions simulées et physiques.
- Contribuer au projet c-PETRUS en fournissant une solution technologique intégrable et validée.

Pour atteindre ces objectifs, le travail est structuré autour du développement d'un algorithme APF personnalisé, l'intégration de ce dernier dans une architecture de téléopération haptique, la modélisation géométrique et anthropomorphe des obstacles, ainsi que la validation par simulation et par des tests physiques.

Le chapitre 1 contient plus de détailles expliquant le contexte médical de l'application et la justification des choix techniques pour l'intégration de la sonde échographique avec la modalité d'imagerie CT-PET. Un état de l'art pour les méthodes de planification de trajectoire et évitement d'obstacle et détaillé dans le chapitre 2. Ce chapitre contient aussi un état de l'art pour la robotique collaboratives et l'échographie robotisé.

3. Méthodologie proposée

Le système robotisé développé repose sur le bras collaboratif UR3e de Universal Robots, reconnu pour sa compatibilité avec les environnements partagés homme-robot, sa compacité et sa précision. Le robot est équipé d'un support permettant la fixation d'une sonde échographique. L'approche de téléopération choisie repose sur une architecture maître-esclave, dans laquelle l'utilisateur pilote la sonde à l'aide d'un dispositif haptique Phantom OMNI.

L'originalité de la méthode réside dans l'intégration d'un algorithme de planification de mouvement basé sur les champs de potentiel artificiels (APF) directement au niveau du robot esclave. Cet algorithme agit en temps réel pour calculer des forces virtuelles qui modifient la trajectoire du robot en cas de détection d'un obstacle dans l'environnement. Le robot combine alors les ordres donnés par l'opérateur avec les forces répulsives issues des obstacles détectés. Ces forces répulsives sont calculées d'une manière à éviter la collision entre des obstacle de plusieurs formes complexes et le corps entier du robot manipulateur.

Le champ de potentiel artificiel est défini par deux composantes :

- Un **champ attractif**, qui guide le robot vers la pose (position et orientation) souhaitée par l'opérateur. Il s'agit d'un vecteur orienté vers la cible, dont l'intensité dépend de la distance (en position et en orientation) à celle-ci. Ce champ est responsable du mouvement principal de la sonde vers la zone d'imagerie.

- Un **champ répulsif**, activé en présence d'obstacles à proximité. Il génère une force inversement proportionnelle aux distances entre des point critiques du robot et les points les plus proches de l'obstacle, et s'annule au-delà d'un certain seuil de détection.

La combinaison de ces deux champs permet d'assurer un compromis dynamique entre fidélité au mouvement désiré et sécurité opérationnelle. Cette architecture permet également d'intégrer le retour haptique : les forces calculées au niveau du robot esclave peuvent être renvoyées au dispositif Phantom OMNI, offrant à l'opérateur une perception tactile des contraintes de l'environnement. Les forces répulsives sont calculées pour deux types d'obstacle (sphérique et cylindrique creux).

Les premières validations sont effectuées en simulation à l'aide d'environnements construits sous MatLab. Le bras robotique (UR5) est modélisé avec précision, ainsi que les obstacles géométriques, la cinématique directe et inverse, et les lois de contrôle. Ces validations permettent d'ajuster les paramètres des champs (gains, rayons d'influence, seuils de déclenchement) pour garantir un comportement fluide, sans oscillations ni blocages. Les détailles de la conception de la méthode de planification de trajectoire avec évitement d'obstacle APF et les résultats de simulation avec MatLab existent dans le chapitre 3. Des tests avec un robot réel (UR3e) sont réalisé avec l'aide de l'environnement ROS (Robot Operating System) et expliqués dans le chapitre 5.

4. Modélisation des obstacles et extension à l'humain

L'environnement d'imagerie CT-PET comprend de nombreux éléments fixes (parois internes du portique, appareils) mais aussi des acteurs humains (patient, soignants), dont la présence impose une attention particulière en termes de sécurité. Le système robotisé doit donc être capable de détecter et d'éviter efficacement tous les types d'obstacles présents dans son espace de travail, qu'ils soient rigides, déformables, statiques ou dynamiques.

Les premiers essais du système d'évitement ont été réalisés avec des obstacles simples : sphères ou cylindres creux. Ces formes permettent de valider les algorithmes d'APF en conditions géométriquement prévisibles. Les obstacles sont définis par leur position, leur rayon d'influence, et une intensité de répulsion variable. Ces configurations sont intégrées dans l'environnement de simulation MatLab (chapitre 3) et dans l'environnement ROS (chapitre 5). Cependant, dans un contexte clinique, cette simplification géométrique est insuffisante. Le patient, par exemple, ne peut être modélisé par une simple forme sphérique : sa morphologie est complexe, asymétrique, et surtout, son volume est réparti de façon non uniforme dans l'espace. De même, un opérateur penché dans le portique introduit des obstacles dynamiques à géométrie changeante.

Pour répondre à cette exigence de réalisme, une modélisation anthropomorphe des obstacles a été introduite. La partie haut du corps humain est représenté comme un assemblage de volumes elliptiques ou cylindriques segmentés : tête, cou, poitrine et bras.

Chaque segment est associé à une zone d'évitement définie selon sa criticité (risque de blessure en cas de contact). Les champs de potentiel sont alors générés autour de ces volumes, avec une transition douce entre les zones actives et neutres.

Cette modélisation permet au robot de "comprendre" la présence d'un corps humain dans son environnement, et d'adapter sa trajectoire pour éviter tout contact. Elle est particulièrement utile dans les situations où les capteurs de vision sont partiellement occultés, ou lorsque le mouvement de l'opérateur n'est pas prévisible par le spécialiste qui téléopère le robot. Des fonctions de lissage ont été implémentées dans les lois de répulsion pour éviter les discontinuités dans les trajectoires du robot. Sans ces fonctions, l'intensité des forces pouvait générer des sauts brusques ou des arrêts intempestifs, nuisibles à la qualité de l'échographie et au confort d'utilisation. Le chapitre 4 contient toutes les détailles utiles pour comprendre cette modélisation de l'être humain comme un obstacle pour l'éviter avec l'aide de l'APF.

5. L'intégration de APF avec un système de téléopération et retour haptique

Le système de téléopération mis en œuvre repose sur une architecture maître-esclave, dans laquelle l'utilisateur contrôle la position de la sonde échographique à distance via un dispositif haptique Phantom OMNI. Ce dernier permet une manipulation à six degrés de liberté, avec un retour d'effort sur trois axes, fournissant ainsi une interaction naturelle et intuitive à l'utilisateur.

Deux architectures de téléopération ont été explorées au cours de la thèse :

1. **Téléopération unilatérale** : dans cette configuration, l'utilisateur pilote la sonde en temps réel, et les forces d'évitement sont appliquées localement au niveau du robot esclave. Le Phantom OMNI n'est utilisé que pour envoyer des commandes, sans retour d'effort. Ce mode est simple à mettre en œuvre, mais il limite la perception de l'environnement distant.

2. **Téléopération bilatérale** : ici, les forces générées par le champ de potentiel sont renvoyées à l'opérateur via le Phantom OMNI. Ce retour haptique permet à l'utilisateur de ressentir les interactions du robot avec l'environnement, telles que la proximité d'un obstacle. Ce mode favorise une manipulation plus fine, améliore la réactivité de l'utilisateur et renforce la sécurité.

L'intégration du retour haptique a nécessité le développement d'une architecture de communication robuste entre le robot et le dispositif maître, notamment pour gérer les délais (latence) et les synchronisations. Les forces haptique transmises sont filtrées et adaptées pour éviter les effets de bruit ou les oscillations.

Le système a été testé avec différents scénarios, dans lesquels l'opérateur manipulait la sonde d'imagerie dans des environnements contenant des obstacles fixes. Nous avons utilisé le robot UR3e et implémenté les méthodologies sous l'environnement ROS. Les essais ont montré une intégration réussite et montre que le retour d'effort améliore significativement la qualité de la navigation et la confiance de l'utilisateur dans le système. Il permet également de réduire la charge cognitive, en fournissant des informations tactiles complémentaires aux images visuelles affichées.

Enfin, cette architecture hybride permet de déléguer partiellement la gestion des risques au robot, tout en conservant le contrôle décisionnel au niveau de l'opérateur humain. C'est un exemple typique d'interaction homme-robot équilibrée, dans laquelle les capacités complémentaires de l'homme (perception, jugement) et du robot (réactivité, précision) sont exploitées conjointement. Les détailles de la méthodologie d'intégration de l'APF avec la téléopération et ces résultats existent dans le chapitre 5.

6. Résultats expérimentaux

Pour évaluer l'efficacité du système développé, plusieurs séries d'expérimentations ont été menées, à la fois en simulation et dans un environnement physique, à l'aide du robot UR3e (UR5 pour la simulation), du dispositif Phantom OMNI, d'obstacles géométriques.

Environnement de simulation : Dans un premier temps, des simulations ont été réalisées sous MatLab avec un modèle complet du bras UR5 (proche du UR3e en termes de structure). Ces simulations ont permis de tester différentes configurations de champs de potentiel (avec ou sans obstacles, statiques) et d'optimiser les paramètres (gains, rayons de détection, zones de transition).

Les résultats montrent que l'algorithme APF permet une navigation sûre dans un environnement complexe, même en présence de plusieurs obstacles simultanés. Les trajectoires sont déformées de manière fluide et prévisible, sans oscillations brusques. En absence d'obstacles, le robot suit fidèlement les ordres de l'utilisateur, démontrant une bonne transparence de l'algorithme.

Expérimentations physiques : Les tests physiques ont été réalisés avec un bras UR3e installé sur une table expérimentale, à l'intérieur d'un environnement simulant la télé-échographie. Des obstacles fixes ont été positionnés dans la zone de travail. Le Phantom OMNI permettait à l'utilisateur de piloter la sonde à distance, avec ou sans retour haptique.

Les expériences ont porté sur plusieurs scénarios :

- **Navigation avec obstacles simples** : le robot devait atteindre des cibles situées derrière des blocs rigides. L'APF permettait d'éviter systématiquement les contacts, tout en maintenant une trajectoire lisible par l'opérateur.

- **Tests de téléopération** : l'utilisateur a piloté la sonde à travers différents parcours. Les essais avec retour haptique ont montré une réduction significative du stress opérateur.

En conclusion, les résultats expérimentaux confirment plusieurs points essentiels :

- ✓ Le système permet une navigation sûre dans un environnement médical contraint.
- ✓ Le retour haptique améliore la qualité du geste et la confiance de l'utilisateur.
- ✓ L'algorithme APF est réactif, prédictible et compatible avec une interaction en temps réel.

✓ Le système s'intègre sans conflit avec la logique de téléopération.

Ces performances valident l'approche hybride adoptée, dans laquelle un opérateur humain contrôle le geste médical, tandis que l'assistance algorithmique garantit la sécurité et la stabilité du robot. Les résultats de simulation et expérimentation se trouvent dans les chapitres 3 et 5.

7. Conclusion

Cette thèse porte sur l'intégration des robots collaboratifs dans les procédures médicales, notamment l'échographie à distance couplée à l'imagerie CT-PET. Elle propose une approche innovante basée sur l'utilisation de l'algorithme de champ de potentiel artificiel (APF) pour éviter les collisions dans des environnements médicaux contraints.

7.1. Apports principaux :

✓ Imagerie multimodale robotisée : Intégration de l'échographie et de l'imagerie CT-PET sous guidage robotique, permettant une meilleure précision et de nouvelles possibilités en intervention médicale.

✓ Interaction homme-robot et sécurité : Analyse approfondie des interactions physiques entre humains et robots (pHRI) avec une attention particulière aux normes de sécurité comme l'ISO/TS 15066.

✓ Évitement d'obstacles avec APF : L'algorithme APF s'est révélé efficace pour planifier les trajectoires en temps réel et éviter les obstacles simples et complexes (sphériques, cylindriques). Il a été simulé puis appliqué sur le robot UR3e.

✓ Téléopération sécurisée : L'APF a été intégré dans une structure de téléopération avec retour haptique, permettant aux médecins de réaliser des échographies à distance en toute sécurité.

7.2. Perspectives :

A. Court terme :

1- Améliorer l'algorithme APF pour gérer les obstacles dynamiques, les zones de minimum local et lisser les trajectoires.

2- Étendre les modèles d'obstacles pour représenter l'anatomie humaine de façon plus réaliste (ex. : cylindre elliptique).

3- Réduire les délais de réponse du système en optimisant la configuration logicielle (ROS sur Linux).

B. Moyen terme :

1- Renforcer le retour haptique avec des dispositifs plus performants (lambda.7).

2- Ajouter un système de suivi optique pour mieux gérer les obstacles mobiles.

3- Introduire un contrôle en compliance pour permettre un guidage manuel sécurisé du robot.

4- Envisager des expérimentations cliniques et des applications industrielles (centrales nucléaires, maintenance spatiale).

En résumé, cette thèse propose une approche solide et innovante pour intégrer les robots collaboratifs dans le domaine médical, en mettant l’accent sur la sécurité, la précision et l’interaction naturelle avec les opérateurs humains. Elle ouvre la voie à de futures recherches et à des applications concrètes en milieu hospitalier et industriel.

Mustafa ELAHRES

Planification de mouvement basée sur le champ potentiel artificiel pour une échographie robotisée sûre : application à l'imagerie médicale multimodale

Résumé :

Cette thèse de doctorat traite de l'intégration de la robotique collaborative dans les flux de travail d'imagerie médicale, en se concentrant sur la télé-échographie dans des environnements de scan CT-PET. En utilisant le robot UR3e, cette recherche améliore l'imagerie multimodale en combinant l'échographie avec les scans CT-PET, améliorant ainsi la fiabilité des diagnostics. L'algorithme du Champ Potentiel Artificiel (APF) est appliqué pour éviter les collisions, garantissant une navigation sécurisée du robot autour des obstacles. La thèse aborde également l'interaction homme-robot en étendant le APF pour modéliser des obstacles de forme humaine, assurant ainsi la sécurité dans les environnements médicaux. Les systèmes de téléopération avec retour haptique virtuel, utilisant le dispositif Phantom Omni, offrent une assistance tactile aux opérateurs lors des procédures d'échographie et augmentent la sécurité en leur permettant de détecter les obstacles et de téléopérer le robot pour les éviter. Les résultats expérimentaux valident l'efficacité du système, apportant des améliorations significatives en matière de sécurité lors de ces procédures. Les travaux futurs viseront à affiner l'algorithme APF, à améliorer les dispositifs haptiques et à réaliser des essais cliniques.

Mots clés : Robot collaboratif, planification de mouvement, évitement de collisions, champ de potentiel artificiel, interaction humain-robot sûre, téléopération, retour haptique, télé-échographie robotisée, CT-PET

Motion planning based on the Artificial Potential Field for safe robotized echography: Application to multimodal medical imaging.

Abstract:

This PhD thesis discusses the integration of collaborative robotics into medical imaging workflows, focusing on tele-echography within CT-PET environments. Using the UR3e robot, this research enhances multimodal imaging by combining ultrasound with CT-PET scans, improving diagnosis reliability. The Artificial Potential Field (APF) algorithm is applied for collision avoidance, ensuring safe robot navigation around obstacles. The thesis also addresses human-robot interaction by extending APF to model human-like obstacles, ensuring safety in medical settings. Teleoperation systems with virtual haptic feedback, using the Phantom Omni device, provide tactile assistance to operators during ultrasound procedures and increase safety by enabling them to sense the obstacle and teleoperating the robot away. Experimental results validate the system's effectiveness, offering significant improvements in safety during such procedures. Future work will refine the APF algorithm, upgrade haptic devices, and aim for clinical trials.

Keywords: Collaborative robot, motion planning, collision avoidance, artificial potential field, APF, safe human-robot interaction, teleoperation, haptic feedback, robotized tele-echography, CT-PET

Laboratoire PRISME, Université d'Orléans

8 Rue Léonard de Vinci - 45072 Orléans